

# **Partitioning of membrane components in adhering vesicles**

vorgelegt von

Dipl.-Ing.  
Jan Steinkühler  
geb. in Düsseldorf

von der Fakultät II - Mathematik und Naturwissenschaften  
der Technischen Universität Berlin  
zur Erlangung des akademischen Grades

Doktor der Naturwissenschaften  
Dr. rer. nat.

genehmigte Dissertation

Promotionsausschuss:

Vorsitzender: Prof. Dr. Holger Stark  
Berichter/Gutachter: Priv.-Doz. Dr. Rumiana Dimova  
Berichter/Gutachter: Prof. Ph.D. Dennis Discher  
Berichter/Gutachter: Prof. Dr. Peter Hildebrandt

Tag der wissenschaftlichen Aussprache: 30. März 2016

Berlin 2017



## Disclaimer

Parts of this thesis have been published and others will be published.

Chapter 3 – **J. Steinkühler**, J. Agudo-Canalejo, R. Lipowsky, R. Dimova, Modulating Vesicle Adhesion by Electric Fields, Biophysical Journal, Volume 111, Issue 7, 4 October 2016, 1454-1464, <http://dx.doi.org/10.1016/j.bpj.2016.08.029>

Chapter 4 - Adhesion of multicomponent vesicles (*working title*) **J. Steinkühler**, R. Lipowsky, R. Dimova

Chapter 5 - Specific adhesion by CD47- SIRP $\alpha$  complexes (*working title*) **J. Steinkühler**, C. Alvey, R. Lipowsky, R. Dimova, D. Discher

All parts of this thesis were written and experimental data was obtained by me, Jan Steinkühler, except the analysis of binding energies (3.1.6 and 3.1.7) which was performed by Jaime Agudo-Canalejo.

Berlin, 1. Februar 2016

Jan Steinkühler

## Acknowledgements

The Max Planck Institute of Colloids and Interfaces has always been a pleasant and inspiring place to work and I would like to say thank you to all members of the department, specifically in the Theory & Bio-Systems group. Roland Knorr helped me with growing my first vesicles. Carmen Remde does a great job to maintain the lab despite the many people working there. Susanne Weber was most helpful in helping me to find my way through the department. Most importantly I would like to thank Romy Dimova who was always encouraging, pointed me in the right direction or other times left me the freedom to explore. I'm very lucky to have such a helpful supervisor. Discussions with Jaime Agudo on shapes of vesicles contributed greatly to my understanding, and the perspective of Prof. Lipowsky has always been an important contribution. During my PhD I had the chance to visit Prof. Dennis Discher's labs where I was welcomed in the most generous way. The stay would not have been a success without his drive and the help of his great lab. Jerome Irianto should be especially mentioned here. My research was funded by the DFG *via* the IRTG 1524 graduate school and I would like to thank the whole team of the IRTG for their great help in administrative issues and organisation of various workshops and symposia.

## Abstract

Biological membranes are segmented into functional compartments of different length and time scales. Here we study model systems which mimic certain aspects of these multiscale phenomena. We introduce a novel experimental setup for modulating adhesion of giant unilamellar vesicles to a planar substrate. Adhesion is induced by application of an external potential to a transparent ITO electrode (the substrate), which enables single-vesicle studies. We demonstrate tuneable and reversible adhesion of negatively charged vesicles. The adhesion energy at different potentials is calculated from the vesicle shape assessed with confocal microscopy. Two approaches for these estimates are employed: one based on the whole contour of the vesicle and a second one based on the contact curvature of the membrane in the vicinity of the substrate. Both approaches agree well with each other and show that the adhered vesicles are in the weak adhesion regime for the range of explored potentials. Using fluorescence quenching assays, we detect that, in the adhering membrane segment, only the outer bilayer leaflet of the vesicle is depleted of negatively charged fluorescent lipids, while the inner leaflet remains unaffected. We show that depletion of negatively charged lipids is consistent with solutions obtained by Poisson Boltzmann theory which accounts for lipid mobility. We also show that lipid diffusion is not significantly affected in the adhering membrane segment adhesion zone in the case of fully miscible membrane components. We then extend this method to the study of multicomponent lipid membranes, which exhibited domains due to a miscibility gap in the liquid phase, as a simple biomimetic model of a heterogeneous membrane. Upon adhesion, we find complex remodelling of membrane composition and morphology, depending on the initial phase of the membrane. Particularly we find a previously undescribed budding transition in the contact line of adhering vesicles. Initially phase separated vesicles are robust against budding transitions in the explored adhesion energies. Only under conditions where membrane components are fully miscible, buds appear. We link these buds to lipid flows between the two membrane compartments. Finally, we study specific adhesion by membrane bound proteins. By natural reconstitution of the membrane protein CD47 into giant plasma membrane vesicles, we can study adhesion complexes. This model is suitable to extract two membrane proteins, which are difficult to assess with established methods.

## Zusammenfassung

Biologische Membranen sind in funktionale Kompartimente von verschiedenen Zeit- und Längenskalen eingeteilt. In dieser Arbeit untersuchen wir Modellsysteme, welche verschiedene Skalen von Biomembranen abbilden. Dazu haben wir eine neue Methode entwickelt, um die Adhäsionsenergie von „Giant Unilamellar Vesicles“ zu einer ebenen Oberfläche präzise einzustellen. Adhäsion wird durch ein externes elektrisches Potential induziert, welches an eine transparente ITO Elektrode angelegt wird. So wird die Untersuchung von Adhäsionsphänomenen an einzelnen Vesikeln möglich. Wir zeigen, dass so reversible und einstellbare Adhäsion von elektrisch negativ geladenen Vesikeln möglich ist. Die Abhängigkeit von Adhäsionsenergie zu angelegtem Potential haben wir auf zwei verschiedenen Wegen bestimmt. Sowohl eine Methode, die die Morphologie von adhärenen Vesikeln berücksichtigt, als auch die Bestimmung der Adhäsionsenergie durch die Membrankrümmung in der Nähe der Kontaktlinie liefern übereinstimmende Ergebnisse. Die gewonnenen Daten zeigen, dass sich die Vesikel im „weak adhesion“ Regime befinden. Durch Fluoreszenzauslöschungs-Experimente zeigen wir, dass im adhärierenden Membransegment nur die äußere Membranhälfte von negativ geladenen Lipiden verarmt wird, während die innere Membranhälfte unbeeinflusst bleibt. Die Verarmung von negativ geladenen Lipiden ist konsistent mit einer Poisson-Boltzmann-Theorie, welche Lipidmobilität explizit berücksichtigt. Des Weiteren zeigen wir, dass die Lipiddiffusion in beiden Kompartimenten nicht beeinträchtigt ist, solange die Membrankomponenten ideal mischbar sind. Im Folgenden betrachten wir Multikomponenten-Vesikel, welche Domänen, hervorgerufen durch eine Mischungslücke in der flüssigen Phase, zeigen. In Abhängigkeit von der Initialen Membranphase führt die Adhäsion von solchen Vesikeln zur komplexen Remodellierung von Membranzusammensetzung und Morphologie. Insbesondere beschreiben wir bisher unbekannte Membranauswölbungen („Buds“) in der Kontaktlinie von adhärenen Vesikeln. Wenn phasenseparierte Vesikeln adhäreren, erscheinen zunächst keine Buds. Nur unter Bedingungen, in denen die Membrankomponenten vollständig verflüssigt werden, erscheinen Buds. Wir diskutieren einen möglichen Mechanismus, der auf Lipidflüsse zwischen den beiden Segmenten basiert. Abschließend untersuchen wir die spezifische Adhäsion von Vesikeln durch Membranproteine. Wir stellen fest, dass natürlich rekonstituiertes CD47 in „Giant Plasma Membrane Vesicles“ Adhäsionskomplexe bilden kann. Dieses Modell ermöglicht es, die zweidimensionale Bindungskonstante zu bestimmen, welche mit etablierten Methoden schwierig messbar ist.

## Table of Contents

1	Introduction .....	10
1.1	Structure of lipids and lipid bilayers .....	10
1.2	Thermodynamics and phases of multicomponent lipid bilayers.....	11
1.3	Typical mechanical quantities and morphologies of fluid lipid bilayers.....	14
1.3.1	Morphologies of adhering vesicles .....	15
1.4	Cell membranes as compartments .....	16
1.4.1	Components and structure of the plasma membrane .....	16
1.4.2	Adhesion and Polarization of Cell membranes.....	18
1.5	Biomimetic models of the plasma membrane.....	19
2	Methods.....	21
2.1	Confocal microscopy .....	21
2.2	Total internal reflection fluorescence microscopy .....	22
2.3	Determination of $T_{\text{mix}}$ .....	23
2.4	Fluorescence recovery after photobleaching (FRAP) .....	24
2.5	Image analysis .....	25
2.6	Preparation of model membranes.....	26
3	Modulating vesicle adhesion by electric fields.....	28
3.1	Materials and Methods.....	29
3.1.1	Vesicle preparation and imaging .....	29
3.1.2	Fluctuation analysis .....	30
3.1.3	Setup of the adhesion chamber .....	30
3.1.4	Quenching assay and fluorescence intensity measurements .....	31
3.1.5	Fluorescence recovery after photobleaching (FRAP) measurements.....	31
3.1.6	Image processing and extraction of the adhesion energy from the vesicle contour	32
3.1.7	Assessing the membrane tension.....	34
3.1.8	Deducing the adhesion energy from the contact curvature .....	34
3.1.9	Numerical solution and parameter estimation of the charge regulated PB equation.....	35
3.2	Results and Discussion .....	36

3.2.1	Calculated adhesion energies at varied external potential .....	37
3.2.2	Redistribution of lipids in the adhering membrane segment .....	39
3.2.3	Mechanism of induced adhesion and lipid depletion .....	43
3.3	Conclusions and Outlook.....	46
4	Adhesion of multicomponent vesicles.....	48
4.1	Methods .....	49
4.1.1	Determination of the miscibility temperature of free vesicles .....	49
4.1.2	Study of phase changes in adhering multicomponent GUVs .....	49
4.1.3	Intensity measurements .....	50
4.2	Results .....	50
4.2.1	Adhesion induces heterogeneous responses in phase separated GUVs...50	
4.2.2	DiIC18 redistribution by adhesion depends on the initial membrane composition .....	52
4.2.3	Domains coarsen in the adhering membrane segment .....	55
4.2.4	Adhesion-induced budding transition depend on the membrane phase state	56
4.2.5	Liquid ordered domains in the contact line of adherent vesicles .....	57
4.2.6	Domains with reduced contrast close to the critical composition.....	57
4.3	Discussion.....	58
4.3.1	Upon adhesion, membrane phase state and composition are significantly changed only close to a critical point .....	58
4.3.2	Relevance to the immunological gap: Dynamic budding transition due to lipid flows between segments .....	60
4.4	Conclusion .....	61
5	Specific adhesion by CD47- SIRP $\alpha$ complexes .....	62
5.1	Methods .....	63
5.1.1	Phagocytosis assay.....	63
5.1.2	Generation of HEK-CD47-GFP Cell Line, Cell culture and GPMV isolation	64
5.1.3	Purification and absorption of SIRP $\alpha$ on glass slides .....	64
5.1.4	Antibody labelling of GPMV, RBC and SIRP $\alpha$ .....	64
5.1.5	Confocal imaging, FRAP experiments and Image analysis.....	64
5.1.6	K <sub>3d</sub> assay using Red Blood Cells (RBCs) .....	65



5.1.7	LUV preparation and Zeta potential measurements.....	65
5.2	Results and discussion.....	66
5.2.1	Cd47 is reconstituted in GPMVs .....	66
5.2.2	Adhesion of CD47 expressing GPMVs to SIRP $\alpha$ .....	67
5.2.3	FRAP indicates cooperative enrichment of CD47 in the adhering membrane segment.....	69
5.2.4	Acidic, tumour like, conditions lead to decrease of $K_{2d}$ .....	71
5.3	Conclusion .....	71
6	Summary and Outlook .....	72
7	References .....	73
8	Appendix .....	80
8.1	List of figures .....	80

# 1 Introduction

This thesis is divided into four chapters. Each chapter starts with a short introduction to the particular goals and field of study. Concepts and terminology relevant throughout this work are introduced in the first chapter. Of particular relevance is how simple cell models lead to understanding of the more complex processes in biological systems. Also aspects of lipid bilayer morphology and phases which are important for the next chapters are discussed. In Chapter 3 we investigate non-specific forces between vesicles of simple compositions and planar substrates. In Chapter 4 adhesion of multicomponent membranes exhibiting domains is considered. Finally, we investigate specific adhesion by membrane bound protein complexes in a model system.

## 1.1 Structure of lipids and lipid bilayers

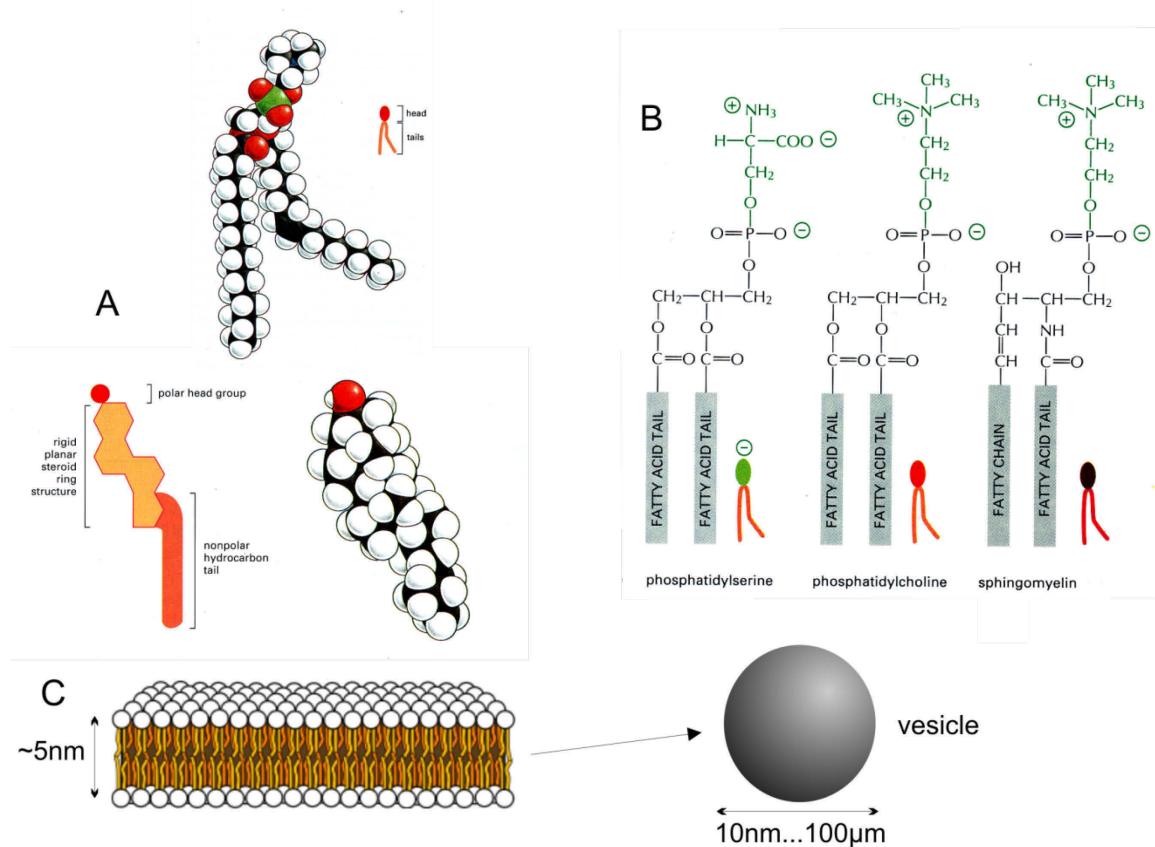


**Figure 1-1 - A)** Schematic drawing of a phospholipid (upper) and cholesterol (lower), spheres indicate atoms **B)** Three different lipid types found in biological membranes **C)** Lipids in a bilayer and closed lipid bilayer (vesicle). Note the separation of length scales. Figures adapted from Alberts <sup>1</sup> p. 479,481

The building blocks of the biological membranes are lipids. Lipids are amphiphilic molecules, meaning that they have a hydrophilic part and a hydrophobic one. Out of the many possible molecular configurations of this general structure, we focus on the most abundant types found in biological membranes. The general structure of phospholipids is shown in Figure 1-1A. The two hydrocarbon chains (fatty acids) of lipids are hydrophobic (to hydrate them with water molecules is energetically unfavourable) and the polar head group is hydrophilic. The fatty acids are characterized

by their length (common lengths are 16 to 24 carbon atoms) and their amount of double bonds (e.g. none (18:0) or one (18:1)) which, in case of a cis-bond, can be thought of as a kink in the conformation of the tail. In biological membranes, sphingomyelin is mostly found with completely saturated fatty acid chains while other phospholipids are mostly unsaturated. Phospholipids exhibit different headgroups, some of them are shown in Figure 1-1B, phosphatidylserine differs from the other headgroups, since it carries a net negative charge (-1) at neutral pH. Another important component of biological membranes, with somewhat different structure, is cholesterol which is shown in Figure 1-1A.

Due to hydrophobic and hydrophilic interactions lipids in water assemble (the critical micelle concentration (CMC) of 16:0 phosphocholine is 0.46 nM) into structures that minimize their free energy (a process referred to as “self-assembly”). A variety of aggregate types (or assemblies) can be obtained, the structure depends on the specific lipids, hydration, salts, temperature etc. Typically, at low concentrations lipids form micelles and with increasing concentration more complex assemblies of higher dimensions, such as the cubic phase. We focus on lamellar phases and specifically on single lamellar “lipid bilayers”, which are the natural state for membranes. It should be noted that non-bilayer structures are important to many biological processes e.g. membrane fusion. Lipid bilayers are usually formed when lipids are fully hydrated and exhibit a configuration of two opposing leaflets (Figure 1-1C left). This can be easily understood by the energetic penalty if one would try to “unzip” the lipid bilayer to expose the hydrophobic core of the lipids. Furthermore, one can understand the closed (spherical) form of lipid bilayer vesicles (Figure 1-1C right) because of the penalty to expose a bilayer edge to water. Vesicles constitute an important membrane model which is discussed in Section 2.6. In the next paragraph we focus on multicomponent lamellar phases.

## 1.2 Thermodynamics and phases of multicomponent lipid bilayers

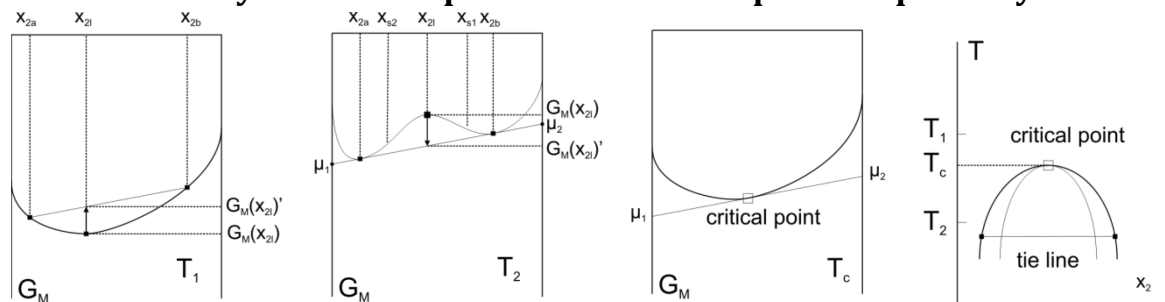


Figure 1-2 – Free energy of a hypothetical binary mixture of composition  $x_2$  exhibiting liquid-liquid separation shown at three different temperatures. Most right: Resulting isobaric phase diagram. Figure adapted with modifications from Koningsveld, et al. <sup>2</sup> p. 46

Let's first review some basic thermodynamic aspects about phases and phase separation. In Figure 1-2, the Gibbs free energy of a binary mixture exhibiting a liquid-liquid miscibility gap is shown at three different temperatures. At a temperature higher than the critical temperature  $T_1 > T_c$ , we find a homogeneous fluid, characterized by the convex curvature of the free energy curve. Any separation into two compositions would result in higher energy of the system ( $G_m(x_2)' > G_m(x_2)$ ) and therefore does not happen spontaneously. At temperatures below  $T_c$ , the local maxima of the free energy

allows for coexisting phases as the system can lower its energy  $G_m(x_2)' < G_m(x_2)$ . Compositions of  $x_{2a}, x_{2b}$ , exhibit the same chemical potential of each substance in the two phases, as required by thermodynamic equilibrium. In a homogenous mixture of composition  $x_{2l}$ , any small fluctuation will lower the total energy by separation into two phases of composition  $x_{2a}, x_{2b}$  (these points are called binodals). Any composition between the two points of inflexion  $x_{s1}, x_{s2}$  will separate this way, note that there is no energetic barrier to cross and no matter how small the fluctuations are, separation will occur, until the minimum free energy is reached (spinodal decomposition). Starting compositions closer to the equilibrium composition  $x_{2a}, x_{2b}$ , are thermodynamically (meta)stable as the condition  $(\frac{\partial^2 G_m}{\partial x_2^2} > 0)$  is met. These compositions can demix by nucleation and growth. At  $T=T_c$  the two binodals points coincide and, as the critical temperature is approached, both phases converge to the same composition and the first order transition becomes a second order transition at this point. From the positions of binodals and spinodals a phase diagram as shown in Figure 1-2 can be constructed. Tie-lines indicate the compositions of the two phases.

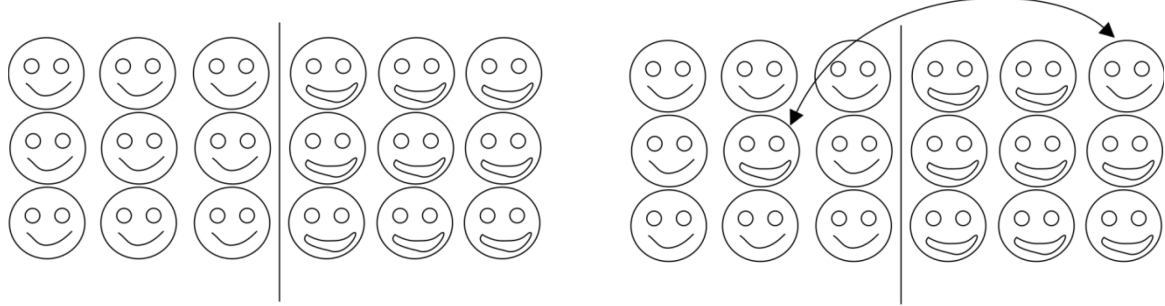


Figure 1-3 – Two substances are separated at  $T=0$  (left). Exchange of two molecules at  $T>0$  (right)

Up to now, we have not discussed the physical mechanism of the miscibility gap. Without going into too much detail, in the case of partial miscibility of substances, one can understand it as a process driven by entropy. Consider molecules on a lattice as shown in Figure 1-3 left, of two completely separated substances. The energy of the system is determined by the interaction of neighbouring molecules and shall be such that likewise interactions are favourable. At  $T>0$ , the system can lower its energy by the exchange of molecules between the two species, due to the higher entropy of the configuration (Figure 1-3 right). The balance between entropic gain and mismatch energy creates the miscibility gap. Neglecting any boundary effects, assuming molecules of equal size and ideal-gas entropy of molecules, the change in free energy  $G_m$  for the described system can be written as<sup>2</sup> p. 101

$$\Delta G_m = RT(x_1 \ln(x_1) + x_2 \ln(x_2)) + hx_1x_2 \quad (1)$$

$RT$  is the ideal gas constant,  $x_2 = 1 - x_1$  are the mole fractions of exchanged molecules and  $h > 0$  is a parameter that describes the mismatch energy between two molecules of different species and doesn't depend on temperature. Solutions of this expression for binodal and spinodal curves, gives a symmetric phase diagram with  $2T_c = h$ , shown in Figure 1-2 right. The above principles also hold for mixture with more components. The dimensionality rises with the number of components  $N$ . For

example in three components mixture there is a line of critical points. The number of phases that can coexist is given by the Gibbs phase rule.

$$f = N - P + 2 \quad (2)$$

where  $f$  are the degrees of freedom,  $N$  number of components,  $P$  number of phases.

We now focus on the miscibility gap of flat or closed lipid bilayers consisting of two or more lipids. Single-component lipid bilayers can be either in a liquid (called  $L_\alpha$ ) or solid-like (gel) state, termed  $L_\beta$ . A characteristic feature of one component lipid lamellar phases, is the melting transition at  $T_m$  from gel to liquid which is a sharp first order transition with pronounced changes in lipid packing and conformation<sup>3</sup>. Already binary mixtures of sterols, e.g. cholesterol, and saturated lipids, such as sphingomyelin, show more complex phase behaviour. The small sterols can interdigitate between the chains and form a liquid sub phase, the liquid ordered ( $L_o$ ) phase<sup>4</sup>. In contrast, the liquid phase formed by low melting temperature lipids such as DOPG and DOPC, exhibits low order and is termed liquid disordered,  $L_d$ . Lipid mixtures forming  $L_o$  and  $L_d$  phases exhibit a liquid-liquid miscibility gap and in lipid bilayers made of mixtures of these lipids, optically resolvable domains can be observed. Since the lipids and domains are liquid, domains fuse and grow over time, eventually reaching equilibrated phase separation. For mixtures of a high melting temperature lipid, low melting temperature lipid and cholesterol, a number of phase diagrams were resolved and for a wide range of compositions,  $L_o$ - $L_d$  phase separation was observed<sup>5</sup>. A typical phase diagram of this type is shown in Figure 1-4. The exact boundaries depend on the lipids and not all lipid mixtures exhibit all phases shown. Also, it is under discussion whether the transitions in the lower right corner are of first or second order<sup>6</sup>. The lipid compositions discussed have an upper critical solution temperature, as temperature is increased the components become fully miscible.

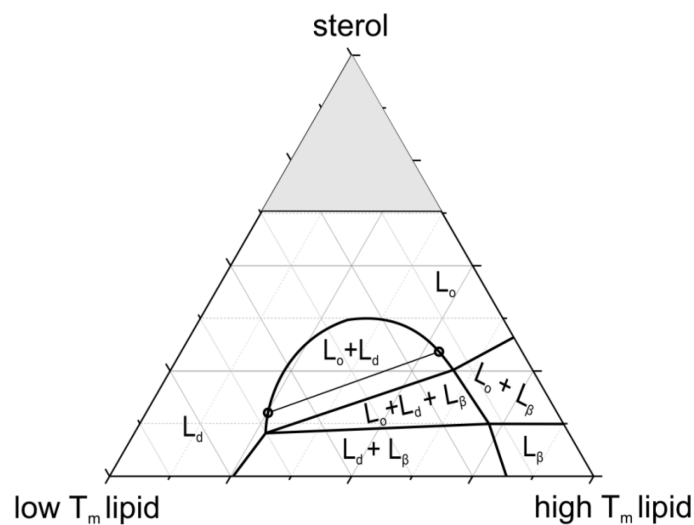


Figure 1-4 – Typical phase diagram for ternary lipid mixture of low and high melting temperature lipids and a sterol. The phases are labelled as described above. In the shaded area lipid bilayers are not formed. A tie line is indicated.

It is instructive to note the typical free energies involved in membrane phase separation. Typical lipid-lipid interaction energies are between  $-3$  and  $2 k_B T$ <sup>7</sup>. These small interaction energies are an indication that membrane phase state can be influenced by various external stimuli. Indeed, change of the temperature by a few degrees, addition of salts, adsorption of proteins and membrane-membrane interactions lead to pronounced changes in phase state and membrane conformation<sup>8-10</sup>.

### 1.3 Typical mechanical quantities and morphologies of fluid lipid bilayers

For fluid bilayers, the shear elasticity is  $\mu_{\text{sheer}}=0$ . The stretching elasticity of a typical lipid bilayer is in the order of  $240 \text{ mN/m}$ <sup>11</sup>. Lipid bilayers rupture at area changes of about 4%, hence one can often assume that the area of a lipid bilayer is constant. It was found, that the morphology of fluid lipid bilayer vesicles can be well described by the famous Helfrich bending energy

$$E_b = \int \frac{\kappa}{2} (2H - C_0)^2 + \bar{\kappa} K dA \quad (3)$$

where  $H$  is the curvature,  $K$  Gaussian curvature,  $A$  the surface area of the vesicle and  $\kappa$  the bending rigidity,  $\bar{\kappa}$  Gaussian bending rigidity and  $C_0$  spontaneous curvature. This expression is valid as long as the lateral dimensions of the membrane are much bigger than its thickness (sheet approximation) and assumes constant volume and area. For example giant unilamellar vesicles (GUVs) have lateral dimension in the order of  $>10 \mu\text{m}$ , while a typical lipid bilayer is only  $5 \text{ nm}$  thin, and their morphologies are, in general, well described by (3)<sup>12</sup>. If one considers the special case for a spherical vesicle of radius  $R$  and vanishing spontaneous curvature, we find  $H^2 = \frac{1}{R^2}$  and see that  $dA \sim R^2$ . In this case the free energy doesn't depend on the size of the vesicle and the bending rigidity becomes the only parameter. Hence, the bending rigidity sets the typical energy scale for fluid lipid bilayer vesicles and is found to be of the order of  $10-100 k_B T$ . Detailed analysis of the Helfrich free energy shows that most vesicle morphologies can be described by only three parameters, the reduced volume  $v = \frac{3}{4} V / (\pi R^3)$ , spontaneous curvature and bending rigidity<sup>12</sup>. The bending rigidity is sensitive to not only the lipid species but also phase state (thickness of the bilayer), inclusions and absorbed molecules such as sugars and salts<sup>13</sup>.

### 1.3.1 Morphologies of adhering vesicles

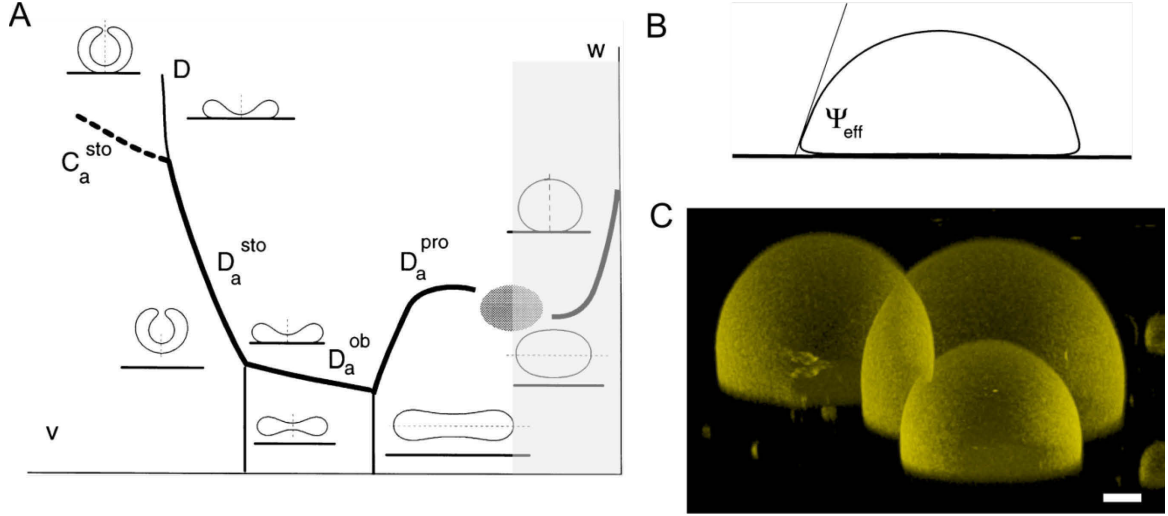


Figure 1-5 – A) Morphology diagram for vesicles close to an adhesive surface. The thick line indicates a first order transition from free to adhered state. The shaded area indicates vesicles usually used in our experiments,  $v$  and  $w$  have the meaning as described in the text (Figure adapted from Ref. 14) B) Definition of the effective contact angle in the case of strong adhesion, the real contact angle is always  $180^\circ$  as the membrane exhibits no kinks C) Artistic rendering of three vesicles adhering to a polylysine coated surface as obtained by confocal microscopy, scale bar  $5\mu\text{m}$

When a vesicle comes into close contact with a planar wall, which exhibits some sort of short ranged attractive interaction with the membrane, the vesicle will spread on the surface. In reminiscence of droplets, this can be understood as a wetting transition. However, in the case of vesicles, change in morphology will cost significant bending energy and the area is conserved. Balance between attractive interactions, tension and bending energy leads to the morphologies of adhering vesicles shown in Figure 1-5A. The free energy of an adhering vesicle of vanishing spontaneous curvature to a planar wall is

$$\Delta G_{adh} = \frac{1}{2} \int \kappa H^2 dA + \Sigma \Delta A - W A_c \quad (4)$$

$A_c$  is the area in contact with the surface of adhesion energy  $W$ ,  $\Sigma$  is tension. The morphological diagram was solved<sup>14</sup> and was found to depend on two parameters,  $w = WR^2/\kappa$  and  $v = \frac{3}{4}V/(\pi R^3)$  and is schematically shown in Figure 1-5. Interestingly, in the case of strong adhesion, one can define a contact angle  $\psi_{eff}$  reminiscent of what is known for the spreading of droplets on planar surfaces (Figure 1-5B).

$$W = \Sigma(1 + \cos(\psi_{eff})) \quad (5)$$

From an experimental point of view, this quantity is not as useful as it is for droplets, because tension is not a material parameter, but depends on the initial membrane tension and reduced volume of the particular vesicle. Both parameters are experimentally not easily controlled.

If one looks at an adhering vesicle, we see that the membrane is divided into two segments. We will call the two segments either “free” or “adhered” membrane segment. This is a simple model for a membrane which is exposed to (two) different environments, which is the case for many membranes in biological systems, as we will see in the Chapter 1.4.2. If the membrane is made of two or more lipids which exhibit different interactions with the planar wall, we expect that the lipid composition will reflect the affinities of the lipids for the two segments. In case of lipids which do not mix ideally, this composition change should lead to a change in phase state and was studied theoretically<sup>15</sup> and explored experimentally in Chapter 4.

## 1.4 Cell membranes as compartments

The idea of compartments is closely connected to what is understood about how life evolved. Without compartments the building blocks (and products of them) would have been too diluted, in what is known as the primordial soup. Apparently these early dividers of compartments have evolved into what we now see as the cell membranes. Among other functions and features, they still perform their initial function: To separate inside from outside, or in the context of cells: separate *life* and *death*. However, to maintain life, energy is needed, hence it must be also possible for certain molecules to cross this barrier. These two properties make up the definition of a membrane: A membrane is a semipermeable divider which allows certain molecules to pass and stops others. Apart from these basic features, biological membranes also serve other purposes. They host a number of membrane proteins and are found in different morphologies and compositions within individual cells and whole organisms. Depending on their location, they perform specific functions. For example, the plasma membrane (the most outer membrane of a cell), has functional roles in cell-cell signalling, adhesion, cell migration and is also the target for many drugs.

### 1.4.1 Components and structure of the plasma membrane

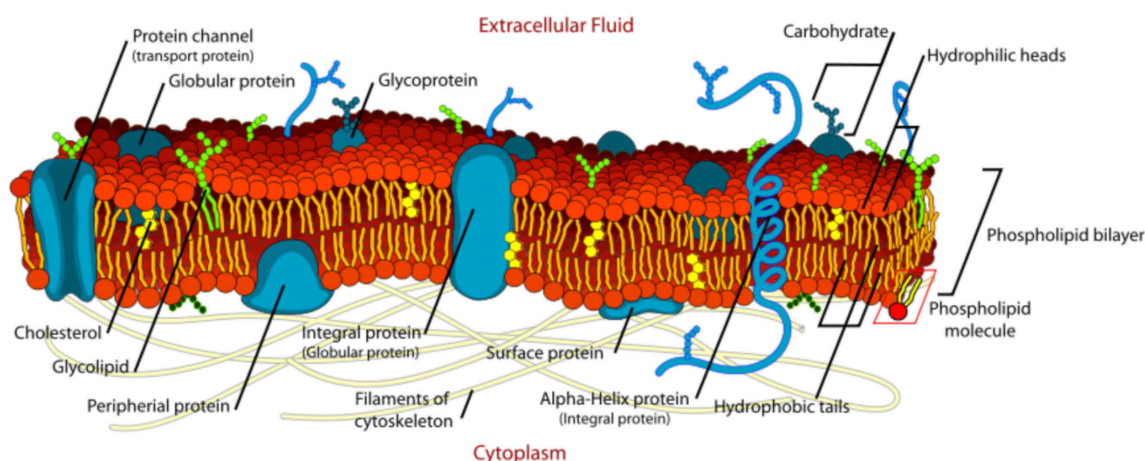


Figure 1-6 – Schematic drawing of the plasma membrane, the density of components is reduced for visibility. Image by Mariana Ruiz.

Out of the different membranes found in cells, we now focus on the plasma membrane of eukaryotes, schematically shown in Figure 1-6. In the following, membrane and plasma membrane will be interchanged. Roughly four different membrane components



can be identified: Lipids, proteins, sugars and a supporting cytoskeleton meshwork. Considering this diversity, the fundamental idea of the fluid mosaic model from 1972 was “that an analogy exists between the problems of the structure of membranes and the structure of proteins. The latter is tremendously diverse in composition, function and *detailed* structure. [...] generalizations about proteins have been very useful in understanding the properties and functions of protein molecules. Similarly, valid generalizations may exist about the ways in which the proteins and lipids are organized in an intact membrane”<sup>16</sup>. Based on the, at that time, known features of biological membranes, the idea of a 2 dimensional (lipid) liquid matrix in which proteins (freely) diffuse was proposed. Since then, the view on biological membranes was refined in mainly three aspects: a) The emphasizes on local heterogeneity in composition, shape (curvature) and between leaflets; b) Membranes are a crowded environment and their components frequently interact with each other; c) The functional role of lipids. The extensions of the original model can be motivated by some observations: Many components of receptor-ligand complexes are diluted on the cell membrane and without local aggregation functions could not be performed. Heterogeneity of the plasma membrane has been observed over different length and timescale, between the typical size of a cell ( $\mu\text{m}$ ) and lifetime (days) to nm sized assemblies with lifetimes down to ms<sup>17-19</sup>. The idea of a heterogeneous membrane is closely connected to the concept of cell polarization.

The functional role of lipids can be understood by their heterogeneity; a typical erythrocyte membrane consists of about 100 different lipids<sup>4</sup> (p.16). While this could be actually an argument, that the specific lipid type doesn't matter, one has to realize that the cell invests energy to specifically sort these lipids between the different membranes and even leaflets of a single membrane. A number of different diseases are specifically attributed to the miss-sorting of membrane lipids<sup>20</sup>. Additionally, the specific morphology of membranes found within cells, for example of the mitochondria, points to a functional role of the membrane morphology. For example, membrane curvature was found to sort membrane components<sup>21</sup>. Beside these specific functions, the structural role of lipids should not be forgotten. If one extracts the other components (say proteins and sugars), they wouldn't reassemble into a dividing barrier and the membrane structure will be lost. However, a membrane can be formed of lipids solely.

To complete the short description of the plasma membrane, two more structures should be mentioned: (a) The free plasma membrane is covered by protective carbohydrate coat (called glycocalyx, Figure 1-7) which has to be displaced before the functional groups on the plasma membrane can be accessed. (b) The plasma membrane is supported by the cytoskeleton, consisting of polymerized filaments connected at specific sites to the membrane. The cell can exert substantial forces by use of these filaments.

A lot more could be said about structure and biological function of the plasma membrane<sup>1</sup>. In the next section we will focus on one particular class of membrane-bound proteins performing a specific function in the cell.

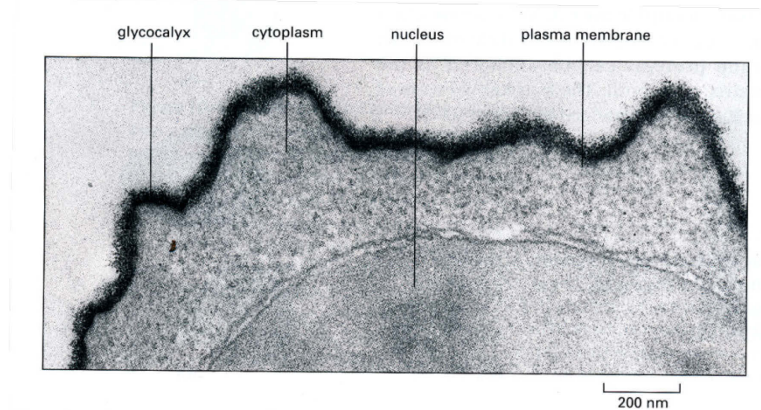


Figure 1-7 – TEM image of a cell. The glycocalyx can be clearly seen as the thick fuzzy dark line, from Alberts <sup>1</sup> p. 502

### 1.4.2 Adhesion and Polarization of Cell membranes

In biological systems, the plasma membrane is almost never isolated. Cells are found to adhere to the extra cellular matrix (ECM) or to other cells of the same or different species<sup>22, 23</sup>. These bonds are established by specialized proteins on the membrane (called cell adhesion molecules, CAMs) which, depending on the particular molecule, bind either to a range of different targets or are highly specific for only one binding partner. Single bonds can span a range of free adhesion energies ( $\sim k_B T$ – $35 k_B T$ ). Adhesion by CAMs is relevant for a number of processes, e.g. cell migration, formation of cell-cell junctions and to the immunological and neuronal synapse. Several different classes of CAMs are established depending on their function, sequence and binding targets, shown in Figure 1-8 left. Arguably, the most general categories are CAMs that bind to alike CAMs (haemophilic) or bind to ligands (heterophilic). Another systematic differentiation is the length of the CAMs. Because these molecules are bound to a membrane, the distance between molecules needs to be closely matched for the molecules to bind, in stark contrast when molecules are solubilized. This is why non-specific forces between membranes need to be considered, even if individual CAMs are specific. To understand this, consider two membranes and a hemophilic adhesion protein (Figure 1-8 right). Two segments are depicted. In one case, non-specific attraction dominates, leading to close contact of the membranes and as molecules are free to diffuse, adhesion proteins are excluded by steric interactions from this membrane segment and do not bind. In the other case, non-specific repulsive (stabilizing) forces dominate, allowing for binding. The interplay of the two energetic minima can lead to a miscibility gap and domain formation. Various theoretical and experimental models have investigated such interactions<sup>15, 22, 24-30</sup>. In analogy, one can think of macromolecules, as found in the glycocalyx, to act as “repellers” interfering with the binding of individual CAMs. Both steric and membrane-membrane interactions, such as hydration energy, electrostatics and thermal undulations, contribute to non-specific forces in the context of cell adhesion<sup>23</sup>.

Upon cell-cell adhesion, a rough sequence of events can be followed: As we saw in Figure 1-7, the cell is covered with the protective layer of the glycocalyx. Thus, to enable “shorter” molecules to bind, big macromolecular repeller must be first displaced out of the adhering membrane segment. Because individual protein species

on the membrane are dilute (typical numbers are  $100/\mu\text{m}^2$  per species), the specific CAMs must now be recruited to the adhering segment, in the simplest case by diffusion. However, when CAMs bind, they not only mechanically stabilize the cell but trigger signalling. This leads to the recruitment of further receptors by active processes. This can result in the formation of domains of complexes as seen in T-Cell adhesion to an antigen presenting lipid bilayer<sup>24</sup>. In addition to the above discussed domain formation due to length mismatch, various other mechanisms for domain formation in adhering membrane segments have been proposed, such as electrostatic blister formation, lipid-lipid, lipid-protein and protein-protein interactions<sup>23, 31-34</sup>. At this point it is interesting to note that one can identify roughly three different length scales which can play a role during cell adhesion: The size of the total adhesion zone between two membranes can be up to the same order as the cell size. Smaller domains between micrometre- to nanometre-sized domains can exist because of favourable interactions between complexes. Finally, molecular interactions play a role in specific receptor-ligand pairs.

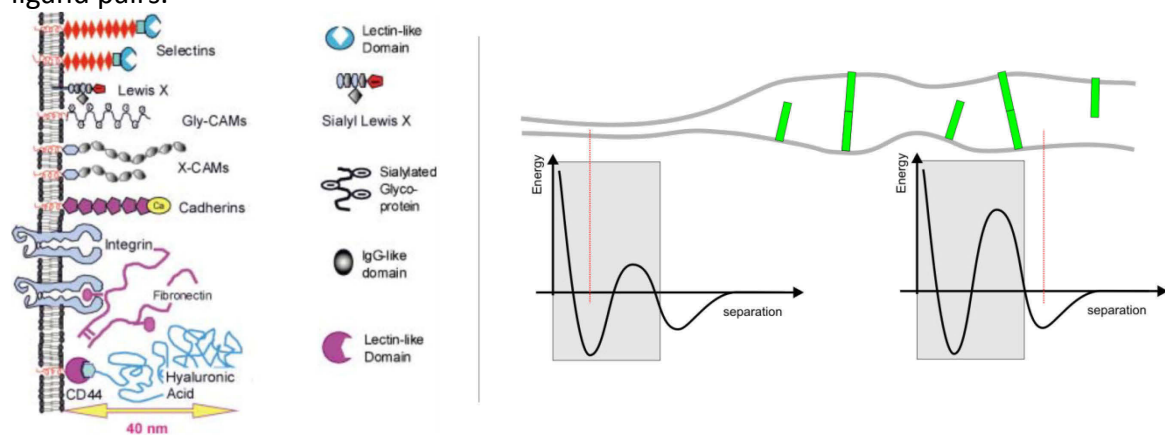


Figure 1-8 – Left: Different classes of CAMs, adapted from Sackmann and Smith<sup>22</sup>. Right: Schematic of two membrane segments exhibiting different membrane-membrane separation due to non-specific interactions (grey), modulating specific binding (green rods)

### 1.5 Biomimetic models of the plasma membrane

Returning to the idea of Singer and Nicolson to ignore the *detailed* structure and find general principles which are conserved among different biological membranes, several models have been explored in order to capture different aspects of biological membranes. Extensive work was done on pure-lipid models. Of particular relevance are GUVs, which are on the dimension of a typical cell. A number of biologically important morphological transitions as fission, fusion and adhesion can be induced and studied in GUVs<sup>11, 12</sup>. Because GUVs can be observed with light microscopy, phase separation can be directly visualized by the use of fluorescent probes. This aspect will be described in more detail in Chapter 2.1. Liquid-Liquid  $\text{L}_\alpha\text{-L}_\beta$  phase separation is considered to be a model for lipid rafts. The definition of rafts is: “Membrane rafts are small (10–200 nm), heterogeneous, highly dynamic, sterol- and sphingolipid-enriched domains that compartmentalize cellular processes. Small rafts can sometimes be stabilized to form larger platforms through protein–protein and protein–lipid interactions”<sup>33</sup>. The proposed lifetime between ms and  $\mu\text{s}$  and size of nanometres is outside the range of direct imaging methods (up to now). Rafts remain a hypothesis which has resulted in

quite some controversy<sup>35</sup>. Independently of this discussion, I would like to note that GUVs which exhibit phase separation are certainly a valid model to observe micrometre sized, local, heterogeneity (domains). It is interesting that one can mimic domains using only a few different lipid species.

If one considers the abundance of proteins bound or inserted into the plasma membrane, it should be not of too much surprise, that recent experimental and theoretical models, consider protein-lipid membranes. Here, proteins (or model molecules) are either reconstituted into lipid-only model membranes (bottom up approach) or pieces of the the plasma membrane of living cells is extracted into giant plasma membrane vesicles (GPMVs) (top down). GPMVs are “blebbed” or lysed from the plasma membrane from cells under chemical stresses<sup>36</sup>. They are a relatively new model system and are interesting because they reconstitute the complex lipid, protein and carbohydrate mixture of the plasma membrane but obtain the morphology of GUVs which is accessible to many experimental and theoretical methods.

Another model membrane system are supported lipid bilayers (SLBs), which represent single bilayer sheets absorbed on a planar surface. They have the advantage that they are compatible to surface characterization methods such as atomic force spectroscopy (AFM) and total internal reflection fluorescence (TRIF) microscopy. However, they are intrinsically asymmetric (as one side is exposed to the support) and under high tension. Extensions to these methods induce spacer groups between the bilayer and supportive surface or create partly free standing bilayers<sup>37, 38</sup>.

## 2 Methods

In this chapter methods used through this work are discussed. Specific measuring parameters and settings are given in the corresponding chapters.

### 2.1 Confocal microscopy

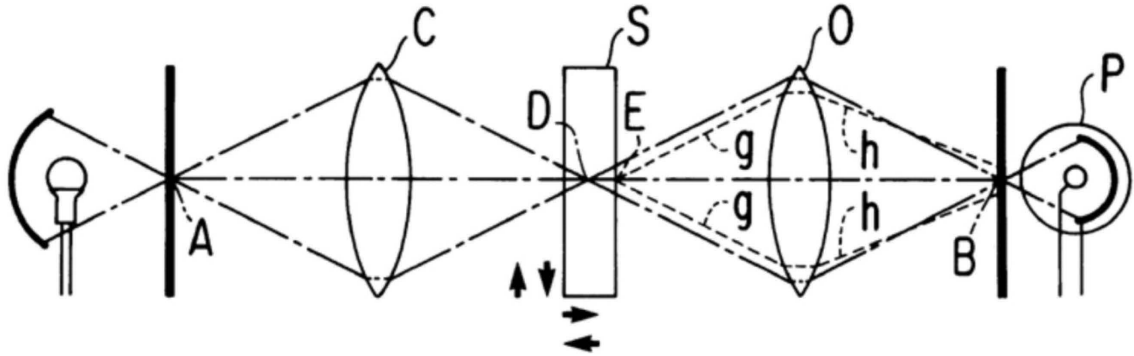


Figure 2-1 – Optical path of a confocal microscope. A-Illumination pinhole, C-Condenser lens, D-image plane. Light from the cone E cannot pass the pinhole B in front of the detector P. O objective lens. Arrows indicate the scanning operation. Figure adapted from Pawley and Masters<sup>39</sup>

Conveniently, study of GUVs can be performed with light microscopy. Even if morphologies of GUVs can be observed using phase contrast microscopy, which is a label free technique, throughout this thesis small amounts of lipid-conjugated dyes are added. These dyes usually show partitioning between different lipid phases, thus information about the phase state can be directly obtained. The used dyes can be excited in the visible light range and relax by a pathway which again emits a photon of slightly lower energy and hence longer wavelength. This frequency shift, leads to a significant reduction in background signal, because the image is spectrally separated from the exciting wavelength. A further reduction of background signal and hence enhancement of achievable resolution is produced by a confocal microscope. The key principle of the confocal microscope is a small pinhole in front of the detector, which blocks the out of focus light (Figure 2-2). Now only light from virtually a point, which lateral extension is due to the wave nature of the light and limits the resolution, is collected. The finite size of the point spread function limits the lateral resolution to:

$$d_{xy} = \frac{0.37\lambda}{NA} \quad (6)$$

Where  $\lambda$  is the wavelength of the (emitted) light and NA the numerical aperture of the lens. High NA water immersion lenses have  $NA=1.2$  and a typical wavelength of  $\lambda \approx 500nm$  gives  $d_{xy} \approx 154nm$ . To obtain a two- or three-dimensional image of a specimen, one needs to move this point in lateral and vertical direction (scanning) by moving the specimen or laser position. This scanning and digitalization operation should fulfil the Nyquist condition by oversampling the smallest structure to be resolved by a factor of two. A number of other parameters influence the obtained image quality and contrast. Obviously the obtained image depends on the sensitivity and noise of the detector, the amount of photons emitted by the dye, which number depends on the excitation energy of the laser. Different technical implementations of

photon detectors exhibit different degrees of sensitivity (down to single photons). Noise always limits the achievable signal-to-noise ratio  $\frac{S}{N}$  and the fundamental limit (for a classical detector) is the shot (or Poisson) noise due to the statistical variation of arriving photons<sup>39</sup>

$$\frac{S}{N} = \sqrt{n_p} \quad (7)$$

where  $n_p$  is the number of arriving photons. Other noise sources are electronic noise in the detector and flickering of the dye. Dye molecules exhibit varying spectra, molar extinction coefficients and quantum yield. Dye characteristics are only linear in their characteristics within certain limits. The local environment, e.g. pH and molecular density, might influence brightness and spectra of dyes. From Figure 2-2, we also see that dyes are of similar size as the lipid molecules. When dyes are used, not only to study the morphology of the membrane, one hopes to extract information about the attached lipid species. In this case, the molecular dimensions have to be seriously considered. For example, MD simulations of the dye DiIC18 in fluid DPPC membranes indicate dye localization inside the hydrophobic core of the membrane which is rather unexpected considering the presence of charges in the hydrophilic region (Figure 2-2 right).

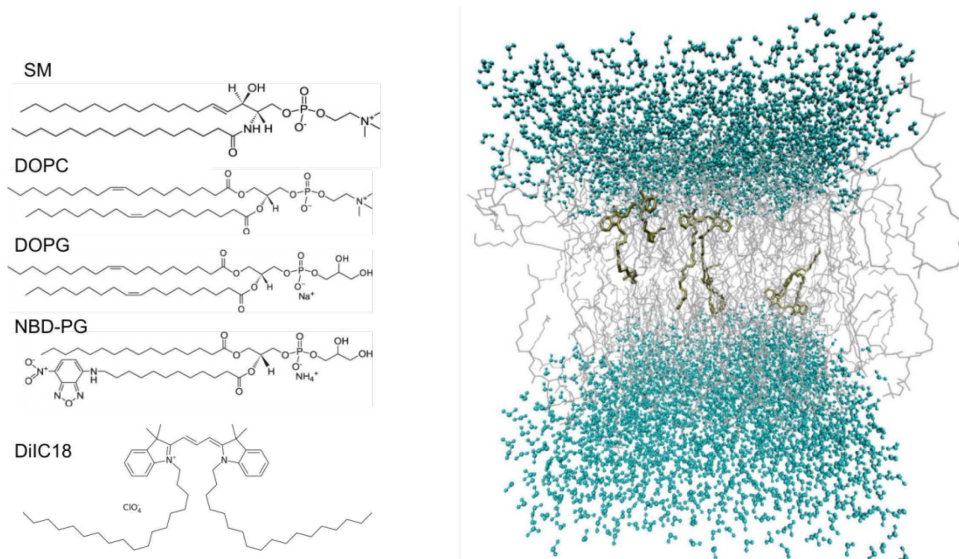


Figure 2-2 – Left: Some lipids used in model membranes and two dyes (NBD-PG and DiIC18). NBD-PG is labelled in the fatty acid chain and DiI is conjugated with two carbohydrate chains. Right: Snapshot of a MD simulation, DPPC membrane with the dye DiIC18, adapted from Gullapalli, et al.<sup>40</sup>

## 2.2 Total internal reflection fluorescence microscopy

Consider a propagating light wave inside a medium of refractive index  $n_1$ , which strikes the boundary to a medium of refractive index  $n_2 < n_1$ . Depending on the angle of incidence, a part of the light is reflected or passes the interface. At angles (from the

interface normal) higher than a critical angle, which can be derived by Snell's law, light is always reflected from the interface<sup>41</sup>

$$\arcsin(\theta_c) = \frac{n_2}{n_1} \quad (8)$$

Due to the wave nature of light, even at an angle higher than  $\theta_c$  an evanesce field decays inside the medium of  $n_2$ . The decay length is set by the angle and refractive indexes  $n_1, n_2$  and in typical biological application (glass-water interface)  $d_{pen} \approx 80-200\text{nm}$  and the intensity follows<sup>41</sup>

$$I_{pen}(d) = I_0 \exp\left(-\frac{d}{d_{pen}}\right) \quad (9)$$

Where  $I_0$  is the evanesce field intensity at the interface. Fluorophores, close to the interface, are excited by the evanesce field and emitted light can be collected by the same lens used to focus the excitation light, just as in epifluorescence microscopy. This is the working principle of a TRIF microscope.

### 2.3 Determination of $T_{mix}$

Figure 2-3 shows a GUV (DOPG:eSM:chol) exhibiting domains. By an external water bath the temperature of the GUV can be controlled and domain formation and mixing can be directly observed. Typically temperature is changed by  $0.5-1^\circ\text{C}$  steps and the membrane is left to equilibrate for 2-5 Minutes. By observation of a vesicle population the average transition temperature  $T_{mix}$  of a particular lipid mixture can be obtained. To check for artefacts induced by photooxidation of the dye, the vesicles can be cooled down to check if membrane demixes at the same temperature  $T_{mix}$ . The used dye DiIC18 partitions into the liquid disordered phase.

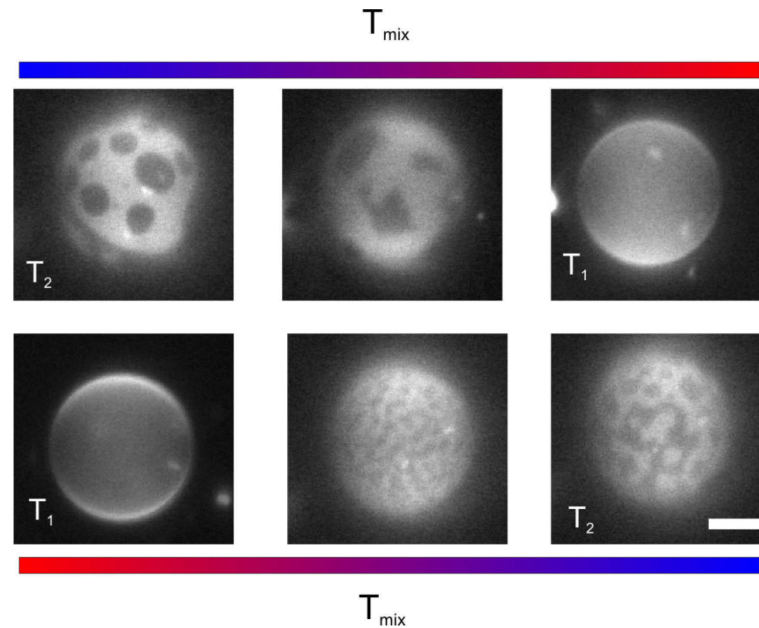


Figure 2-3 The same vesicle observed by epifluorescence microscopy at different temperatures. Upper row: At  $T_2$  the vesicle exhibits optically resolvable domains. The temperature is ramped up fast ( $1^\circ\text{C}/\text{min}$ ) to a temperature



$T_1$  where the vesicle appears homogenous. Rapid cooling leads to spinodal decomposition (lower row). The shown vesicle is not let to equilibrate during the cooling process. Scale bar  $10\mu\text{m}$

## 2.4 Fluorescence recovery after photobleaching (FRAP)

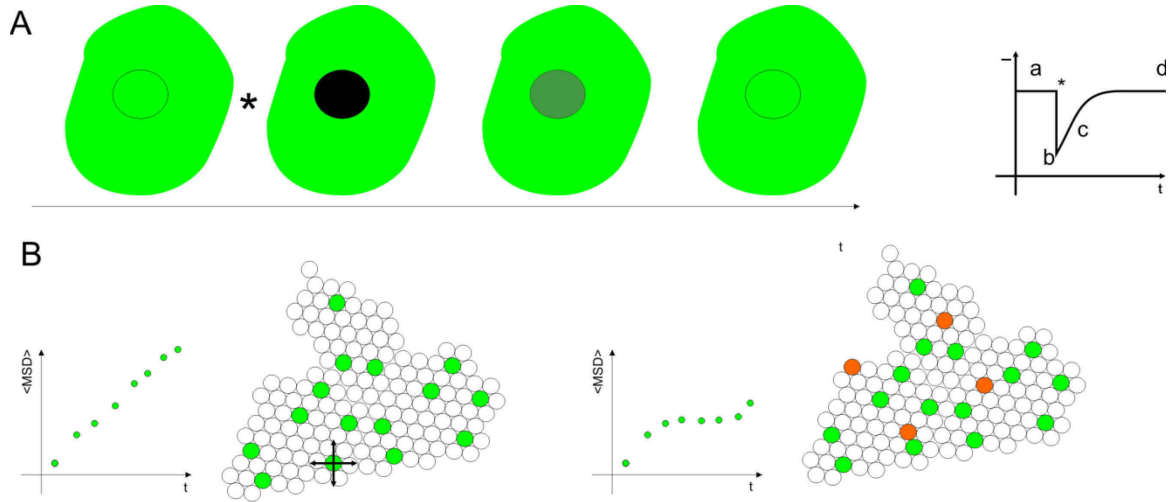


Figure 2-4 A) Schematic of a lipid bilayer stained with a green dye. The circular region of interest (ROI) is bleached by a strong laser pulse at \*. Recovery can be followed by the average intensity in the ROI. B) Two different mechanisms for recovery. Left: free diffusion, right: diffusion and binding and unbinding at immobile locations indicated by an orange circle.

To study the diffusion and dynamics of fluorescent probes (and hopefully the attached molecules), FRAP can be used. When dyes are excited by light, they can be irreversibly (at least on relevant timescales) be trapped in a state where they lose fluorescence, for example by change in conformation induced by the excitation light. Usually this is an artefact complicating fluorescent imaging. However, when dyes are bleached fast by a strong laser pulse, the subsequent recovery of fluorescence can be used to understand the dynamics of the system. This is shown Figure 2-4A in the case of a bilayer where some lipids are conjugated to a dye. After a short and strong laser pulse, all molecules in the region of the bleaching pulse appear dark. Care has to be taken that the duration of the pulse is at least 5-10 times shorter than the typical recovery time, so one can assume that the dye concentration is constant on the edge of the bleached area. Fluorescence is recovered by diffusion of bright molecules from the surrounding region into the bleached region. If the reservoir of unbleached lipids is big compared to the bleached section, and the bilayer is completely fluid and without defects, full recovery is obtained. The diffusion coefficient can be obtained by fitting<sup>42</sup>

$$\frac{I_{free}(t)}{I_0} = \exp\left(-\frac{\tau_d}{2t}\right) \left( \mathcal{J}_0\left(\frac{\tau_d}{2t}\right) + \mathcal{J}_1\left(\frac{\tau_d}{2t}\right) \right) \quad (10)$$

to the recovery curve, where  $I_0$  is the fluorescent intensity before bleaching,  $\mathcal{J}_{0,1}$  are modified Bessel functions of first kind and  $\tau_d$  the fit parameter, with the diffusion coefficient  $D_{free} = r_{frap}/\tau_d$  where  $r_{frap}$  is the radius of the bleached spot. If, instead



of pure lipids, we consider molecules attached to the bilayer which can diffuse and undergo binding (such as proteins), the mechanism of recovery is more complex. A relevant example would be a case where molecules can bind on fixed binding sites that appear immobile (Figure 2-4B). Now a molecule can undergo diffusion and one or more binding and unbinding reactions before it reaches the bleached area. This is reflected in the reaction diffusion equations:

$$\begin{aligned}\frac{\partial[L]}{\partial t} &= D_{free} \nabla^2[L] - k_{on}[L][R] + k_{off}[RL] \\ \frac{\partial[R]}{\partial t} &= -k_{on}[L][R] + k_{off}[RL] \\ \frac{\partial[RL]}{\partial t} &= k_{on}[L][R] - k_{off}[RL]\end{aligned}\tag{11}$$

$[L]$ ,  $[R]$ ,  $[RL]$  are concentration of ligand, receptor and complexes of these two. In the above example  $R$  are the orange dots and (mobile) green  $L$ . This model was solved<sup>43</sup> by Fourier transformation, for the case of nearly fixed free receptor concentration  $\frac{\partial[R]}{\partial t} \approx 0$  and the averaged, normalized, fluorescent intensity  $\overline{I_{bind}}$  follows:

$$\begin{aligned}\overline{I_{bind}}(p) &= \frac{1}{p} - F_{eq} \left( 1 - \mathcal{K}_1(qr_{frap}) \mathcal{J}_1(qr_{frap}) \right) \left( 1 + \frac{\tilde{k}_{on}}{p + k_{off}} \right) \\ &\quad - \frac{1}{F_{eq}} \frac{1}{p + k_{off}} \\ F_{eq} &= \frac{k_{off}}{\tilde{k}_{on} + k_{off}} \\ q^2 &= p/D_{free} \left( 1 + \frac{\tilde{k}_{on}}{p + k_{off}} \right)\end{aligned}\tag{12}$$

$r_{frap}$  is the radius of the bleach spot,  $\mathcal{J}_1$  and  $\mathcal{K}_1$  are modified Bessel functions of the first and second kind, and  $p$  is the Laplace variable,  $\tilde{k}_{on} = [R]k_{on}$  and  $k_{on,off}$  have the usual meaning as binding “on” and “off” rates. The result can be numerically transformed back to the time domain and fitted to the recovery curve.

## 2.5 Image analysis

Usually images are obtained by confocal microscopy which yields several images of the individual planes of the specimen (“stacks”). To quantify the fluorescent intensity from a stack,  $I_{stack}$ , two methods are commonly employed. The 3d dimensional structure can be projected onto a 2d plane yielding intensity  $I_{proj}$

$$I_{proj}(x_0, y_0) = \max_z(I_{stack}(x_0, y_0, z))\tag{13}$$

When the long axis of the point spread function and normal vector of the membrane

are parallel, the membrane can be considered two dimensional and the resulting image is the convolution of the point spread function with a 2D-plane. In this case, an estimate for the fluorophore concentration is directly obtained from  $I_{proj}$ . Alternatively,  $I_{stack(x,y,z)}$  can be fitted to a Gaussian along a suitable trajectory. The amplitude of the Gaussian gives the fluorophore concentration.

## 2.6 Preparation of model membranes

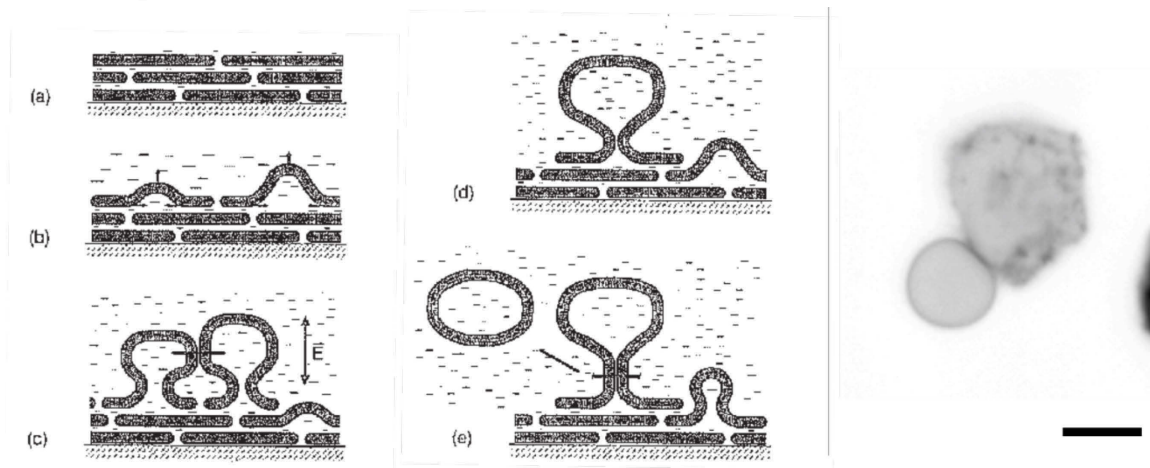


Figure 2-5 – Left: Different stages (a-e) of GUV electroformation, adapted from Luisi and Walde <sup>44</sup>. Right: epifluorescent micrograph of a HEK cell budding a GPMV (inverted contrast). Scale bar 10μm

**GUVs** can be conveniently prepared by electroformation: Lipids dissolved in chloroform are spread on a conductive electrode, usually a platinum wire or indium tin oxide. The chloroform is evaporated rigorously in low pressure conditions and subsequently the lipid film is hydrated in an aqueous solution. By application of a time varying electric field, vesicles are grown from the lipid film. The process is not completely understood but some steps can be identified, see Figure 2-5. By osmotic pressure (enhanced by the movement of ions in the solution by the electric field) a bud nucleates in the bilayer stack b) The electric field acts on the local inhomogeneity of the bilayer stack c) further swelling d)-e) The bud pinches off. Because solvated molecules are encapsulated into the vesicles and the yield of GUV is usually rather high, the vesicle suspension can be diluted before the experiments and concentration gradients across the membrane of about 1:10 are readily obtained by dilution. Commonly vesicles are prepared in a sucrose solution and then diluted in a glucose solution. The sugar asymmetry leads to contrast in phase-contrast microscopy and to sedimentation to the bottom of the chamber due to gravitational forces, which is beneficial for use with an inverted microscope.

**GPMVs** are derived directly from the plasma membrane of *in-vitro* cultured cells. Incubation with Dithiothreitol (DTT), Paraformaldehyde (PFA) or N-Ethylmaleimide (NEM)<sup>45, 46</sup> leads to budding of 10-20μm sized vesicles. The region of vesicle growth is depleted from actin filament and GPMVs grow by osmotic pressure. A GPMV still connected to a HEK cell is shown in Figure 2-5. Eventually GPMVs are cleaved from the cell by an unknown mechanism and can be collected from the supernatant of the solution as cells remain attached to the culture flask. GPMVs are a relatively new

system in the field of membrane models and not completely characterized, even if their extraction was already described in 1978<sup>45</sup>. It is known, that GPMVs reconstitute the gross of transmembrane proteins and lipids<sup>47</sup>, however the concentration of some proteins is altered and lipid asymmetry is at least partly lost. Membrane composition and phase state also depend on the particular chemicals and conditions of the extraction process<sup>48</sup>. This is probably not only a consequence of the GPMV mechanism growth, but also reflects the fact that cells are apoptotic and die during the process.

**Supported Lipid Bilayers (SLB)** can be prepared by incubation of SUVs or LUVs on cleaned glass slides. Individual liposomes adhere to the surface and initially stay intact. The planar bilayer can now grow by two pathways<sup>49</sup>. Either individual vesicles burst on the surface or diffuse until they fuse with other vesicles and eventually burst. These pathways depend on parameters as surface roughness, vesicle density and lipids. In both cases, a planar bilayer adhering to the surface is obtained.

### 3 Modulating vesicle adhesion by electric fields

GUVs have emerged as a versatile model membrane system<sup>11, 50-52</sup>. Applications reach from models of biological membranes to micro-reactors. In this work, we employ them to study adhesion. While in biological systems adhesion is usually ensured by specific adhesion molecules, unspecific forces are always at play. Here, we exploit these interactions and study the adhesion of GUVs to a solid support whereby adhesion is driven by an external electrical potential.

Adhesion of GUVs has been previously explored theoretically or using various experimental approaches, see e.g. Refs.<sup>53-59</sup>. During adhesion, the vesicle undergoes a shape transformation and repulsive membrane undulations against the rigid surface are suppressed. This energetic cost is balanced by the (attractive) interaction between the surface and the vesicle. Generally, an attractive force can be provided either by specific ligand-receptor pairs or by non-specific interactions. Some examples of the latter are provided in the following. Bernard et al. have used polylysine-coated surfaces to induce adhesion of electrically neutral GUVs<sup>60</sup>. In another work, reflection interference contrast microscopy was used to study adhesion of GUVs to a positively charged surface coated with 3-amino-propyl-triethoxy-silane<sup>55</sup>. In a more recent study, the non-specific interaction between a pinned lipid membrane patch from a GUV and a substrate coated with the relatively inert protein bovine serum albumin was studied and the resulting interaction potential strength was extracted from analysis of membrane shape and fluctuations<sup>61</sup>. Other studies explored the adhesion of positively charged GUVs to a planar supported lipid bilayer where the interaction was influenced by changes in bulk pH and hence by modulating the surface charge of the membranes<sup>31, 62</sup>. In all of these works, adhesion was either established in the system by a fixed attraction potential, was irreversible or with no possibility to directly modulate adhesion of the same vesicle.

Here, we introduce a novel method to induce reversible adhesion of GUVs by means of an externally applied electric potential. The advantage of the approach is that the adhesion strength can be varied easily and gradually on the same vesicle. This method enables single-vesicle studies as the GUV can be observed before and after adhesion. The process resembles what is known as electrowetting of (aqueous) droplets on a solid support, see e.g.<sup>63, 64</sup>. We compare two different methods to calculate the adhesion energy from the vesicle morphology assessed with confocal microscopy, investigate the partitioning of a fluorescent lipid analog between the unbound vesicle cap and the bound membrane segment, and measure the lipid diffusivity.

### 3.1 Materials and Methods

#### 3.1.1 Vesicle preparation and imaging

Vesicles were prepared by electroformation (see Ref<sup>65</sup> and Chapter 2.6). Chloroform stock solutions of 1,2-dioleoyl-*sn*-glycero-3-phosphocholine (DOPC) and 1,2-dioleoyl-*sn*-glycero-3-phospho-(1'-*rac*-glycerol) (sodium salt) (DOPG) were mixed at molar ratio 80/20 and final lipid concentration of 4 mM. The lipids were obtained from Avanti Polar Lipids (Alabaster, AL). At neutral pH, DOPG imparts a negative surface charge to the formed vesicles. If not indicated differently, the fluorescent analog DiIc18 (2-[3-(1,3-dihydro-3,3-dimethyl-1-octadecyl-2H-indol-2-ylidene)-1-propenyl]-3,3-dimethyl-1-octadecyl-, perchlorate, Molecular Probes, Eugene, OR) was added to the lipid mixture at a concentration of 0.1 mol%. For the dye distribution measurements, 1 mol% of the fluorescent dye NBD-PG (1-palmitoyl-2-12-[(7-nitro-2-1,3-benzoxadiazol-4-yl)amino]dodecanoyl-*sn*-glycero-3-[phospho-*rac*-(1-glycerol)] (ammonium salt), Avanti Polar Lipids, Alabaster, AL) was added. In total, 10  $\mu$ L of the stock solution were spread on two conductive glasses coated with indium tin oxide (ITO). To eliminate trace amounts of chloroform, the glasses were kept between 2 and 2.5 hours under vacuum at room temperature. They were then assembled to form a chamber of 2 mL volume that was filled with sucrose solution (17 mg/ml) buffered with 2 mM HEPES pH 7.4, containing 1 mM EDTA and with a final osmolality of 63 mOsmol/l. All chemicals were obtained from Sigma. Electroformation was carried out at 10 Hz sinusoidal voltage of 630 mV RMS for 2 hours and at 300 mV and 5 Hz for additional 30 minutes. The vesicles were harvested from the chamber and left to equilibrate overnight at room temperature. Part of the vesicle suspension was mixed with an isoosmolar buffered glucose solution at volume ratio of 1:2 (to a final volume of 90  $\mu$ L). To provide excess area for adhesion, the vesicles were deflated before imaging by letting water from this vesicle suspension to evaporate at room temperature for 40 minutes. The steady increase in osmolality (to a value of approximately 88 mOsmol/l as measured by the decrease in mass during evaporation) deflated the vesicles in a smooth manner. The density difference between the outside and inside solutions led to sedimentation of the vesicles to the bottom of the chamber. When required, the solution conductivity was measured with SevenEasy (MettlerToledo, Switzerland). Imaging was performed on a Leica confocal SP5 setup. DiIc18 was excited with a 581 nm laser line (diode-pumped solid-state laser) and PG-NBD was excited using a 488 line (Argon laser). The fluorescence signal was collected between 565-670 nm and 494-642 nm, respectively. In some experiments, the reflection from the surface of ITO cover glass facing the solution was visualized by scanning with the 488 nm laser line in reflection mode and detecting the reflected light in the range 485-490 nm. Because the difference between the refractive indices of the objective immersion medium (water) and the sugar solution in the vesicle suspension is far below a percent, spherical abbreviations are

negligible (see e.g. Ref. <sup>7</sup>) and were not considered for correcting the vesicle images in z-scans.

### 3.1.2 Fluctuation analysis

We measured the bending rigidity of the DOPC/DOPG vesicles by fluctuation analysis of the thermally induced motion of the membrane. Details of the method are published elsewhere<sup>66</sup>. Experiments were performed on an Axiovert 135 microscope (Zeiss, Germany) using a 40× objective in phase contrast mode. Imaging was done with a fast digital camera HG-100K (Redlake Inc., San Diego, CA) using a mercury lamp HBO W/2 as a light source. We acquired a total of 3600 snapshots per vesicle with exposure time of 200  $\mu$ s. Only vesicles with clearly visible fluctuations and no visible defects were considered for analysis. No difference in the bending rigidity was found for vesicles in sucrose buffer or diluted in glucose buffer in the used sugar concentration range and within the experimental uncertainty.

### 3.1.3 Setup of the adhesion chamber

The adhesion chamber consisted of two ITO coated cover glasses with thickness of 0.17 mm (ITO film thickness < 100 nm, Präzisions Glas & Optik GmbH, Iserlohn, Germany), which were separated by a rubber spacer of 1 mm thickness. The vesicle suspension was not in contact with the spacer and was surrounded by air as shown in Figure 3-1. The chamber was sealed to prevent evaporation during the experiment. Because the ITO film is transparent, vesicles could be observed with a usual inverted (confocal) microscope setup. The ITO glasses were connected with conductive copper tapes to an external signal generator (Model 33220A, Agilent Technologies Deutschland GmbH, Böblingen, Germany) and direct current (DC) voltage was applied with the bottom glass connected to the positive terminal. In series with the voltage source, the electric current was measured using a digital multimeter (Model 2000, Keithley Instruments, Inc., Cleveland, Ohio). The whole chamber was held together by two custom-made metal plates and fitted on the stage of the microscope.

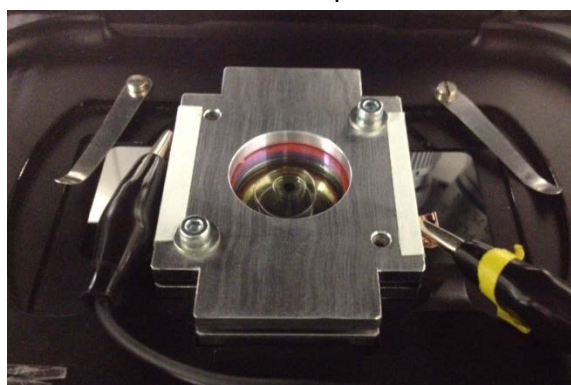


Figure 3-1 - Picture of the experimental chamber fixed on an inverted confocal microscope. Connectors to left and right lead to the DC-voltage source. The transparent ITO glasses can be seen in the middle of the picture. The red spacer is not in contact with the vesicle suspension.

### 3.1.4 Quenching assay and fluorescence intensity measurements

NBD-PG located in the outer leaflet of the vesicles membrane was quenched by reduction with dithionite<sup>67</sup>. We first prepared 1 M stock solution of sodium dithionite (Sigma) in the sucrose buffer used for vesicle preparation. Then 1  $\mu\text{L}$  of this quenching buffer was pipetted into 100  $\mu\text{L}$  of vesicle suspension in sucrose buffer. The solution was gently stirred to ensure homogenous distribution of the quenching agent. The vesicles were then incubated for 15 minutes and consecutively diluted in isoosmolar glucose buffer as done with vesicles not treated with quencher. On the timescales of the observations, no or insignificant leakage of quenching agent into the vesicle interior occurred. The quenching of the external leaflet of the vesicle membrane was confirmed by the decrease of fluorescence to about half the original value (fluorescence from both leaflets).

Fluorescent intensities of quenched and unquenched vesicles were quantified by the peak of a Gaussian fit to the intensity line profile through the membrane normal to the cover glass. The peak value of the Gaussian was then used for further analysis. An example for the fitting for an unquenched and quenched vesicle is shown Figure 3-2. In addition to single vesicle studies, we also obtained statistically relevant results by examination of at least 8 different vesicles from two different batches. Vesicles that exhibited defects such as pinning to the surface or did not react to the external voltage because of local surface defects were not considered for further analysis. For all measurements, the settings of the confocal setup were kept fixed.

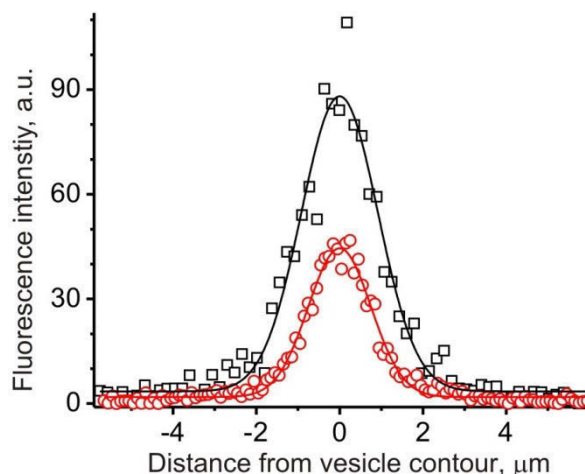


Figure 3-2 - Examples for the intensity profiles across the membranes of an unquenched vesicle (red diamonds) and a quenched vesicle (black squares) adhering to the ITO glass. The profiles were fitted with a Gaussian (OriginPro 8.6) and the peak value taken as an indicator of dye concentration.

### 3.1.5 Fluorescence recovery after photobleaching (FRAP) measurements

NBD-PG was bleached using the 488 line of the confocal microscope. A circular spot with diameter 5  $\mu\text{m}$  in the xy plane both in the adhering membrane segment and at the north pole of a vesicle was bleached for 420 ms. Afterwards, imaging was done at non-bleaching laser intensity for 7 s. The intensity-time trace was then fitted to the

commonly used one-component recovery model<sup>68</sup>. At least 5 individual bleaching curves per vesicle were obtained.

### 3.1.6 Image processing and extraction of the adhesion energy from the vesicle contour

The adhesion energy was extracted from the global shape of the vesicle. In the absence of membrane spontaneous curvature, the equilibrium shape of a homogeneous vesicle adhering to a planar substrate is determined by the bending rigidity of the membrane and the adhesion energy per unit area  $W$ , as well as the total membrane area  $A$  and enclosed volume  $V$  of the vesicle. This minimum energy shape can, in general, only be calculated numerically. In the limit of very strong adhesion  $WA/\kappa \gg 1$ , however, the vesicle maximizes the area bound to the substrate by adopting the shape of a spherical cap, see Figure 3-3 A, with effective contact angle  $\theta_0$  defined solely by the constraints in the total membrane area and volume of the vesicle<sup>53, 69</sup>.

$$\frac{8-9\cos\theta_0+\cos 3\theta_0}{12\sqrt{\pi}(2-2\cos\theta_0+\sin^2\theta_0)^{3/2}} = \frac{V}{A^{3/2}} \quad (14)$$

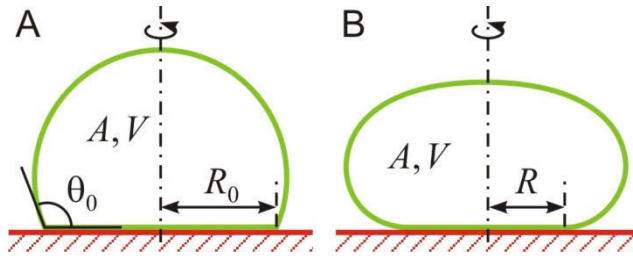


Figure 3-3 - Sketches of the same vesicle with total area  $A$  and enclosed volume  $V$  (A) in the limit of very large adhesion energy and (B) when subject to a finite adhesion energy. In (A), the shape is that of a spherical cap and the values of the effective contact angle  $\theta_0$  and the radius of the adhering membrane segment  $R_0$  are fixed by  $A$  and  $V$  through eq. (1). In (B), the shape deviates from a spherical cap and the radius of the adhering membrane segment  $R < R_0$  is given by eq. (2).

The bound part of the vesicle is a flat disc of radius  $R_0 = \sqrt{\frac{A(1+\cos\theta_0)}{\pi(3+\cos\theta_0)}}$ . For finite values of the adhesion strength, see Figure 3-3 B, the deviations of the vesicle shape from the spherical cap limit can be calculated analytically, and the actual radius of the adhering membrane segment  $R$  is given by<sup>69</sup>

$$R = R_0 - \sqrt{\frac{2\kappa}{W}} \frac{\cos(\theta_0/2)}{1+\sin(\theta_0/2)} + O\left(\frac{\kappa}{W\sqrt{A}}\right). \quad (15)$$

One can finally turn around eq. (15) to find the lowest order approximation to the adhesion strength

$$\frac{W}{\kappa} \approx \frac{2}{(R-R_0)^2} \left( \frac{\cos(\theta_0/2)}{1+\sin(\theta_0/2)} \right)^2. \quad (16)$$



For each vesicle, we capture a series of confocal images of the vertical cross section of the vesicle for increasing values of the applied voltage, see Figure 3-4. The vesicle contour is then identified manually. Assuming that the shapes are axisymmetric (which is confirmed from 3D projection images of the adhered vesicle), we can integrate this contour, and the total membrane area  $A$  and enclosed volume  $V$  of the vesicle can be calculated at each stage. Both the area and the volume of the vesicles are found to remain constant within experimental error as the voltage is increased. In addition, the radius of the adhering membrane segment  $R$  can be directly measured and is found to increase with increasing applied voltage. By inserting the measured values of  $A$  and  $V$  into eq. (14) and solving it numerically, we obtain the values of the effective contact angle  $\theta_0$  and radius of the adhering membrane segment  $R_0$  corresponding to the spherical cap limit. These calculated values, together with the measured value of the radius of the adhering membrane segment  $R$ , can then be inserted in eq. (16) to obtain the dimensionless adhesion energy per unit area  $W/\kappa$ . This process was repeated for each vesicle at each value of the applied voltage. The corresponding error  $\Delta\left(\frac{W}{\kappa}\right)$  is determined by linear propagation of the experimental uncertainties  $\Delta A$ ,  $\Delta V$  and  $\Delta R$  in eq. (16). Finally, an average value over all vesicles of the adhesion energy per unit area is computed, for each applied voltage, by calculating the weighted arithmetic mean of all measured values of  $W/\kappa$  for different vesicles at a certain voltage, with weight given by the inverse variance  $1/\left[\Delta\left(\frac{W}{\kappa}\right)\right]^2$ .

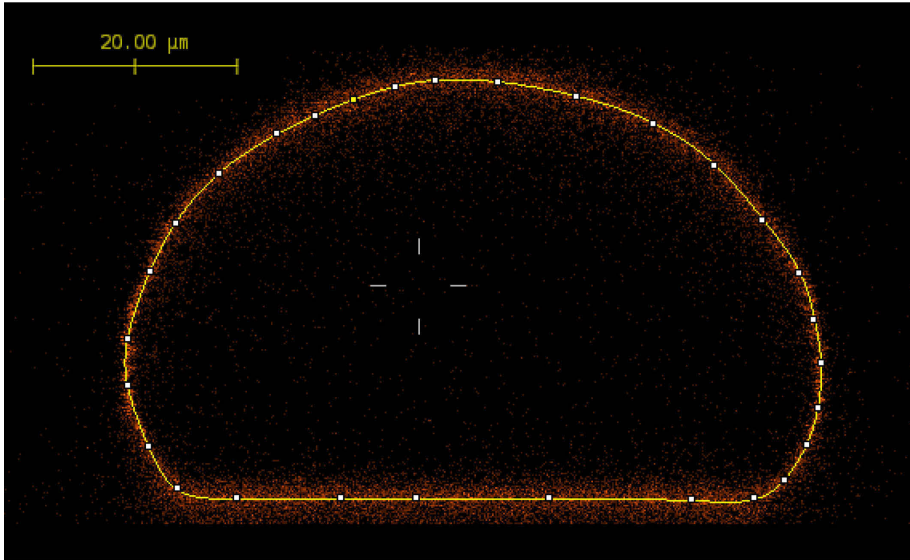


Figure 3-4 - Vertical cross section view of an adhering vesicle (at 1V) as obtained by confocal microscopy. The manually extracted contour which is used in the further analysis of the vesicle area and volume is shown in yellow.

### 3.1.7 Assessing the membrane tension

The membrane tension of the vesicle can be estimated in a similar manner as the adhesion strength, by considering the deviations of the vesicle shape from a spherical cap, which corresponds to the limit of strong adhesion. The free energy  $F$  of the vesicle can be approximated by<sup>69</sup>

$$F = -W\pi R_0^2 + 8\sqrt{\pi\kappa W A} \frac{1 - \sin(\frac{\theta_0}{2})}{\sqrt{3 + \cos \theta_0}} + O(\kappa) \quad (17)$$

where we use the same notation as in the previous section. In mechanical equilibrium, the tension  $\Sigma$  of the vesicle membrane will then be given by<sup>70</sup>  $\Sigma = -\frac{\partial F}{\partial A}\bigg|_V$ , taking into account that both  $R_0$  and  $\theta_0$  depend on the vesicle area. One thus finds for the tension

$$\Sigma = \frac{W}{1 + \cos \theta_0} - \sqrt{\frac{4\pi\kappa W}{A}} \frac{\sqrt{3 + \cos \theta_0} [2 \sin(\frac{\theta_0}{2}) + \cos \theta_0]}{1 + \cos \theta_0} + O(\kappa/A) \quad (18)$$

which represents the well-known Young relation for liquid droplets, together with a correction accounting for the bending rigidity of the membrane. Introducing eq. (16) in eq. (18) in order to eliminate the adhesion strength, we can estimate the tension of the membrane by simply measuring its enclosed volume  $V$ , total area  $A$  and radius  $R$  of the adhering membrane segment

$$\frac{\Sigma}{\kappa} \approx \frac{1}{(R_0 - R)^2 \left[ \sin(\frac{\theta_0}{4}) + \cos(\frac{\theta_0}{4}) \right]^4} - \sqrt{\frac{8\pi}{A}} \frac{1}{R_0 - R} \frac{2 \sin(\frac{\theta_0}{2}) + \cos \theta_0}{\sin \theta_0 + 2 \cos(\frac{\theta_0}{2})} \sqrt{3 + \cos \theta_0} \quad (19)$$

where we remind that  $R_0$  and  $\theta_0$  are determined by the measured volume and area *via* eq. (14).

### 3.1.8 Deducing the adhesion energy from the contact curvature

Because the membrane cannot exhibit a kink in the contact region, the microscopic contact angle is always smooth with a contact curvature of<sup>54</sup>

$$R_c = \sqrt{\frac{\kappa}{2W}}. \quad (20)$$

We extracted this contact curvature from 10 adhering vesicles at different adhesion strengths, by fitting the contour in the contact zone with a circle. To find the optimal circle radius we used a refined fitting method, in which we follow the goodness of fit while increasing the part of the membrane segment considered for fitting and select the fit with the best adjusted coefficient of determination. A typical example is shown in Figure 3-5. This optimal radius is assigned to the contact curvature  $R_c$  and eq. (7) is

used to estimate the adhesion energy independently of the method based on whole-vesicle contour described above.

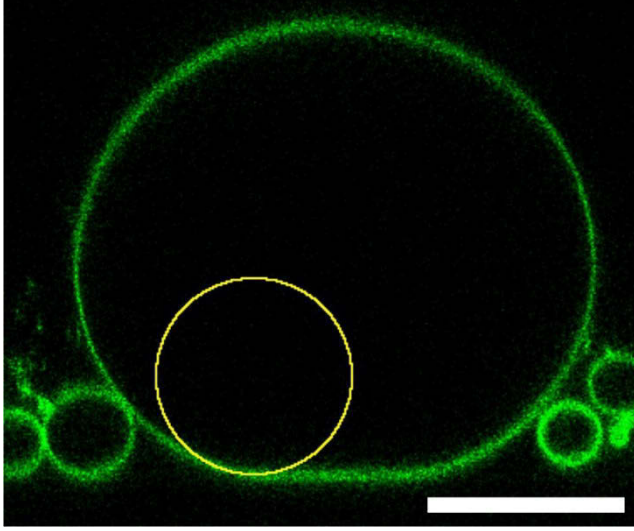


Figure 3-5 - Circle of best fit (yellow) in the contact zone of an adhering vesicle (confocal side view). The scale bar is 25 $\mu$ m.

### 3.1.9 Numerical solution and parameter estimation of the charge regulated PB equation

We solve the Poisson Boltzmann equation for the dimensionless electrostatic potential  $\psi = e\phi/k_B T$

$$\nabla^2 \psi = \kappa^2 \sinh \psi \quad (21)$$

where  $\kappa^{-1} = (\epsilon_0 \epsilon_r k_B T / 2n_0 e^2)^{1/2}$  is the Debye length for a symmetric monovalent salt of bulk concentration  $n_0$  and dielectric constant  $\epsilon_r$ . We did not control the salt concentration of the used buffers directly and the concentration of free ions is set by the buffer, titration and impurities in the used reagents. By conductivity measurements we find an equivalent ionic strength to a 2mM NaCl solution which corresponds to  $\kappa^{-1} \approx 7nm$ . The special boundary condition  $-\alpha \nabla \psi \cdot \mathbf{n} = \frac{e^{-(\psi+\psi_0)}}{(1-\phi)/\phi + e^{-(\psi+\psi_0)}}$  self consistently accounts for the charge regulation due to lipid exchange with an lipid reservoir. Here,  $\psi_0$  denotes the resting potential of a isolated membrane and is set to -100mV,  $\mathbf{n}$  is the normal vector of the lipid plane,  $\alpha = a\epsilon_0 \epsilon_r k_b T / e^2$  with  $a = 70\text{\AA}$  as the surface area of a typical lipid and  $\phi = 0.2$  is the fraction of charged lipids. The boundary condition was derived by Ben-Shaul et al<sup>71, 72</sup>. The ITO surface is considered as an ideal (current blocking) electrode where the charges  $Q_e = C_{if}(V - V_0)^2$  are fixed by the applied potential and the capacitance of the ITO-electrolyte interface and is set to  $C_{if} = 8 \cdot 10^6 \text{ F/cm}^2$ <sup>73</sup>. Solutions are computed using COMSOL v3.5a for 10 separations between  $l = 0.1 \cdot \kappa^{-1}$  to  $4 \cdot \kappa^{-1}$  on a 1 dimensional mesh consisting of 60 elements. The contour plots are generated by spinodal interpolation between the discrete simulation results.

### 3.2 Results and Discussion

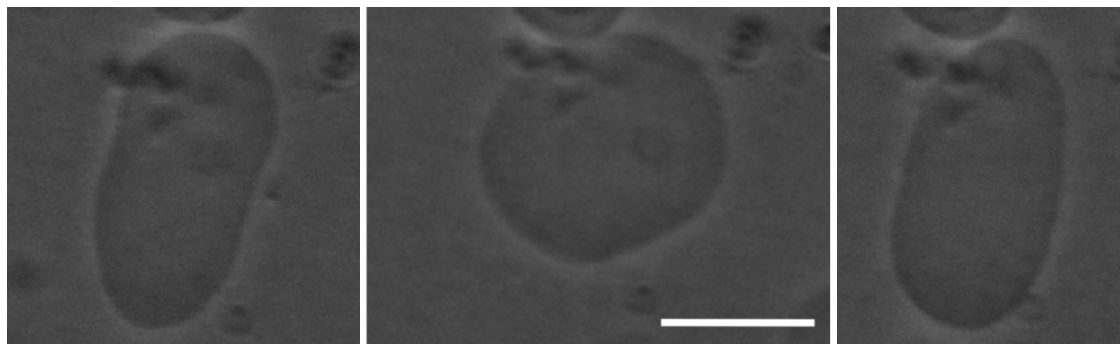


Figure 3-6 - Phase contrast images of a very deflated vesicle consecutively exposed (from left to right) to 0V, 1.2V and 0V external voltage undergoing nearly complete reversible shape change from prolate to adhered back to prolate shape. Scale bar corresponds to 20 $\mu$ m.

Adhesion of a deflated GUV is shown in Figure 3-7. In the absence of DC field, the vesicle exhibits thermal fluctuations, which are suppressed as adhesion sets out at a threshold voltage of about 0.8 V. The vesicle undergoes a shape transition from an unbound to a bound state and the thermal undulations in the lower part of the vesicle in close contact with the ITO surface are inhibited. With further increase in external voltage, adhesion is smoothly regulated by the applied voltage and the vesicles spread further over the surface increasing the area of the adhering membrane segment. Adhered vesicles exhibit a sharper contact angle with the surface similarly to droplets. However, an important difference is that GUVs cannot adapt their surface area freely. Electroformed vesicles are characterized by different initial tensions and degree of deflation in the same batch and we could observe that more tense vesicles do not wet the surface as much as well-deflated vesicles. After the voltage is switched off, the membrane segment in the contact area is again free to fluctuate and the contact angle approaches 180°. The shape change induced by adhesion can be completely reversible, see Figure 3-6. In some cases however, the original overall vesicle shape is not completely recovered indicating a change in the vesicle area-to-volume ratio during adhesion. To probe for changes in the volume, we used phase contrast microscopy to check for leakage of sucrose encapsulated in the vesicles due to formation of pores. No decrease in contrast over the whole range of used voltages was observed (data not shown). Hence, no or only an insignificant amount of leakage occurred due to the adhesion. The vesicle volume as deduced from shape analysis was also found constant. We thus speculate that change in the area-to-volume ratio results from a change in the apparent vesicle area. It is plausible that during adhesion, membrane reservoirs such as tubes or membrane invaginations are pulled to the vesicle surface. Electroformed GUVs are known to frequently exhibit such hidden membrane reservoirs<sup>50, 74</sup>.

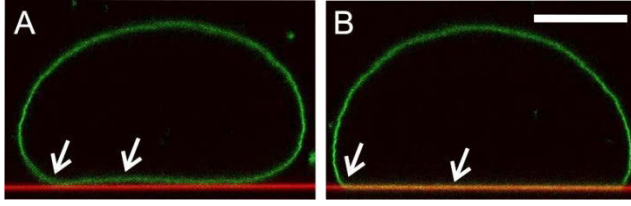
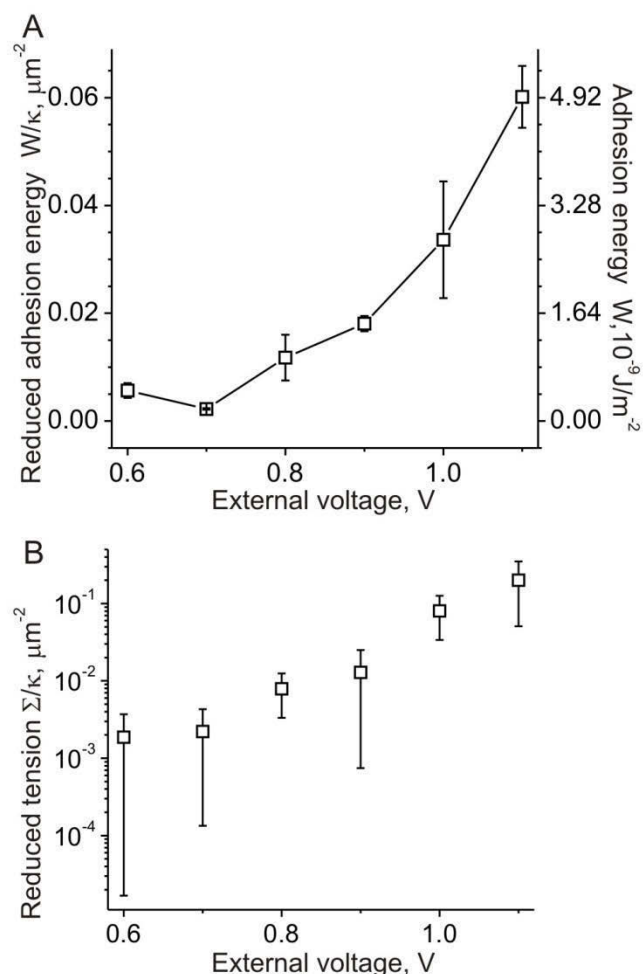


Figure 3-7 - Confocal images of the vertical cross sections of a GUV made of DOPC/DOPG 80/20. The scale bar represents 20 $\mu$ m. The membrane fluorescence is shown in green and the reflection from the ITO surface is shown in red. (A) Non-adhering vesicle in the absence of applied voltage. (B) Same vesicle adhering to the substrate upon application of 1 V DC field. Arrows indicate the suppression of membrane fluctuations in the vicinity of the surface due to adhesion and the appearance of a sharp contact angle.

### 3.2.1 Calculated adhesion energies at varied external potential

We extracted the adhesion energy from the overall vesicle shape as detected by confocal microscopy images recorded for different external potentials, see Figure 3-4. To the best of our knowledge, this is the first time the adhesion energies were directly calculated from vesicle images obtained by confocal microscopy. In agreement with the optical observations, at a threshold voltage of around 0.8 V, a sharp monotonic increase in adhesion energy was measured.

Because the method yields only the reduced adhesion energy  $W/\kappa$ , we have independently measured the bending rigidity  $\kappa$  by fluctuation analysis of nonadhering vesicles, see section Materials and Methods. In total, 20 vesicles were analyzed. For the bending rigidity measured at 23°C, we obtained  $\kappa \cong 20 \pm 2 k_B T$ , where  $k_B T$  is the thermal energy with  $k_B$  the Boltzmann constant and  $T$  the temperature. The found value for the bending rigidity is significantly lower than that measured for DOPC/DOPG 90/10 membranes at pH 5<sup>75</sup>, indicating a rather strong dependence of the bending rigidity on the protonation state of the lipids and hence the surface charge of the membrane as well as the used buffers<sup>13</sup>. Using the measured value of the bending rigidity and assuming that it is not influenced by the adhesion process, we were able to calculate the absolute value of the adhesion energy in our experiments, see right axis in Figure 3-4A. The explored adhesion energies are relatively low and in the regime of weak adhesion. Note that as we will show later, the lipids may redistribute between the bound and unbound part of the vesicle, which might lead to changes in the bending rigidity of the membrane. Thus, in the following, we will present the results in terms of reduced adhesion energy  $W/\kappa$ .



**Figure 3-8 - Adhesion energy and membrane tension in DOPC/DOPG 80/20 vesicles adhering to an ITO substrate at varied applied external potential. (A) Adhesion energies of overall 24 vesicles at different external potentials. The data is obtained from analysis based**

From the overall vesicle shape, we were also able to extract the induced tension as described in section Materials and Methods. As expected, with increasing external voltage, the tension imposed on the adhering vesicle increases, see Figure 3-4 B. Even though the tension increases by approximately two orders of magnitude, the absolute values of the induced tension are relatively low and orders of magnitude below the lysis tension ( $\sim 10 \text{ mN/m}$ ). This is also corroborated by the membrane undulations in the unbound part of the adhering vesicles visible even at the highest applied external voltages. We conclude that the main energetic cost, which is balanced by the attractive potential, originates in the bending of the lipid bilayer.

We compared the data for the adhesion energy obtained from the whole-contour analysis with results obtained with a second method, namely using the contact curvature of the membrane in the contact zone with the surface (see section Materials and Methods for details). The adhesion energies were calculated following both methods for a total of ten vesicles at different external potentials. Generally, the

results from the two approaches agree well, see Figure 3-9. Both methods have high uncertainties at higher adhesion energies for the following reasons. The measured parameters (e.g. area of the adhering membrane segment) used by the whole-contour method saturate towards high adhesion energies, while the contact-curvature method suffers from approaching the diffraction limit when detecting the curvature radius.

For the adhesion energies explored here, the membrane in the contact zone adopted curvature of up to around  $1/(7 \text{ } \mu\text{m})$ , see right axis in Figure 3-9. This curvature is not very high, but potential use of other types of electrodes (allowing access to higher potentials) might allow reaching even higher curvatures, making this approach useful for exploring curvature-driven processes in membranes.

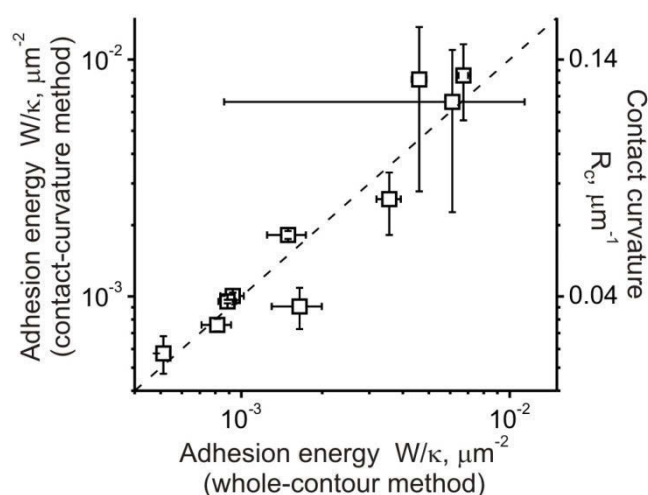


Figure 3-9 - Comparison of data for the adhesion energy assessed via the whole-contour method (x axis) and from the contact-curvature method (left y axis; the right y axis shows the membrane curvature in the contact zone,  $R_c$ ). The dashed line has slope one and represents ideal agreement between the two methods.

### 3.2.2 Redistribution of lipids in the adhering membrane segment

After having demonstrated that vesicle adhesion can be smoothly and reversibly regulated by the external potential, we investigated whether lipid composition of the unbound and bound membrane segments is altered with adhesion. For this purpose, we employed the fatty-acid labeled NBD-PG (see Figure 2-2), which possesses the same head group as that of the negatively charged DOPG, and is thus indicative for the behavior of this lipid when varying the external potential. We hypothesized that since electrostatics might be the driving force for adhesion, the negatively charged species in the membrane may exhibit redistribution once the external potential is applied.

During the experiments, no phase separation as characterized by micrometer-sized domains was observed under fluorescence suggesting that the adhered and unbound membranes remain in the same fluid phase state. The membrane fluidity was confirmed by the measured diffusion coefficient of NBD-PG assessed with FRAP measurements. At 1.1 V external voltage, we found no difference between the diffusion coefficient measured in the adhering membrane segment and the vesicle cap,

suggesting that diffusion of the bound membrane is not hindered by the adhesion process. On the average, the diffusion coefficient of NBD-PG was found to be  $2.4 \pm 0.2 \mu\text{m}^2/\text{s}$ .

We compared the apparently free diffusion in the bound part of the membrane in our system to diffusion in supported lipid bilayers (SLB) prepared on ITO surfaces (i.e. the same substrate material as in our setup). The diffusion in such SLBs is twice slower compared to that in free-standing bilayers<sup>76</sup>. We conclude that the lack of slowdown in the lipid diffusion in our system is due to the weak adhesion and, thus, the rather thick water layer between membrane and substrate in our setup.

Even though the fluidity and diffusivity in the adhering membrane segment is not altered, measurements of the fluorescence intensity of the NBD-PG probe in the adhering membrane segment suggest that the lipid composition in the adhered patch of the vesicle changes during the adhesion process. Figure 3-10 shows typical results for the fluorescence intensity in the adhering membrane segment of a GUV normalized by the value in the absence of applied potential. With the onset of adhesion, the normalized fluorescent intensity drops down. This intensity change results from migration of the dye from the adhering to the free membrane segment. We exclude the possibility of a change in fluorescent brightness of NBD-PG in the adhering membrane segment as the overall fluorescence intensity of the vesicle is preserved during the voltage sweep. Additionally, NBD fluorescence was found to be constant in the pH range between pH 5 and pH 9<sup>77</sup>. Bleaching of the dye was also not observed for the employed laser intensities and exposure times (data not shown). Since NBD-PG is depleted from the adhering membrane segment, we expect that the intensity in the cap of the vesicle would increase resulting from dye enrichment, see sketches in Figure 3-10. However, the quantification analysis and measurements in single-vesicle experiments, were too imprecise because of the presence of micrometre-sized fluctuations of the membrane. In addition, because of the larger area of the unbound membrane compared to that of the adhering membrane segment, the expected increase in fluorescence should be smaller than the intensity change of approximately 10 % measured for the adhering membrane segment. In other words, the expected change in brightness of several percent is below the statistical uncertainty of measurements in the cap region.



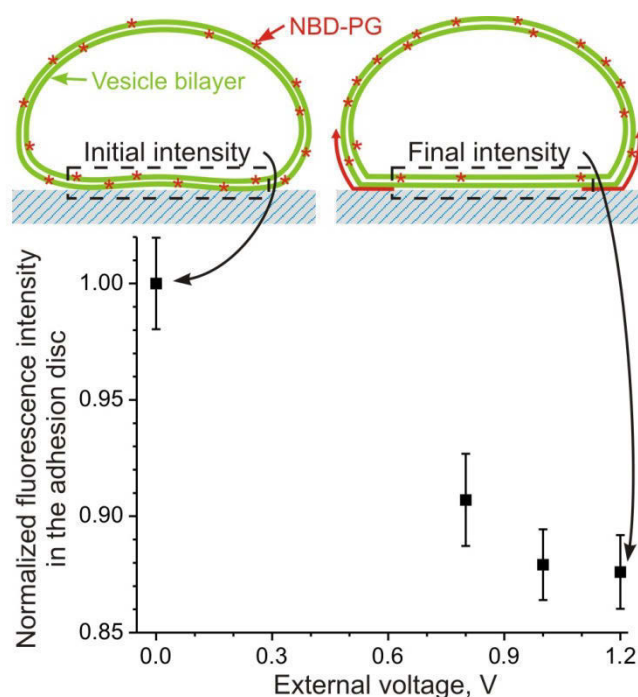


**Figure 3-10** - Normalized fluorescence intensity from NBD-PG in the adhering membrane segment of a (unquenched) vesicle exposed to different external potentials corresponding to different adhesion strengths. The sketches above illustrate the depletion in the adhering membrane segment of NBD-PG (red asterisks) from the outer leaflet of the vesicle upon adhesion to the substrate, see text for details.

To further examine the changes in bilayer composition in the adhering membrane segment and to probe whether the dye depletion occurs in both leaflets, we performed a quenching assay, in which the fluorescence of the outer leaflets of the vesicles before exposing them to adhesion is quenched irreversibly by sodium dithionite. We then measured the fluorescence intensity from the inner leaflet of the vesicle as a function of applied potential, similarly to the measurements in Figure 3-10 on unquenched vesicles. To obtain statistically relevant data we quantified the fluorescence intensity ratio of adhering to free membrane segment of an ensemble of vesicles exposed to different external potentials and hence adhesion strengths. The raw data in terms of ratio of the fluorescent intensity of adhering membrane segment to that in the unbound part is shown in Figure 3-11. While for unquenched vesicles (with fluorescence from both leaflets), adhesion energies and fluorescence ratio of adhering to free membrane segment were found highly correlated (Spearman's rank correlation coefficient  $\rho < 0.0001$ ,  $n = 8$ ), fluorescent intensity and adhesion energy for quenched vesicles (fluorescent signal from the inner leaflet only) was not correlated significantly ( $\rho = 0.37$ ,  $n = 12$ ). This outcome suggests that only the outer leaflet senses the changes in the surface potential of the ITO glasses. The result is consistent with previously reported data on SLBs demonstrating that the substrate affects the lipids only in the proximal or basal side of the SLB but not the distal leaflet of the membrane<sup>78, 79</sup>.

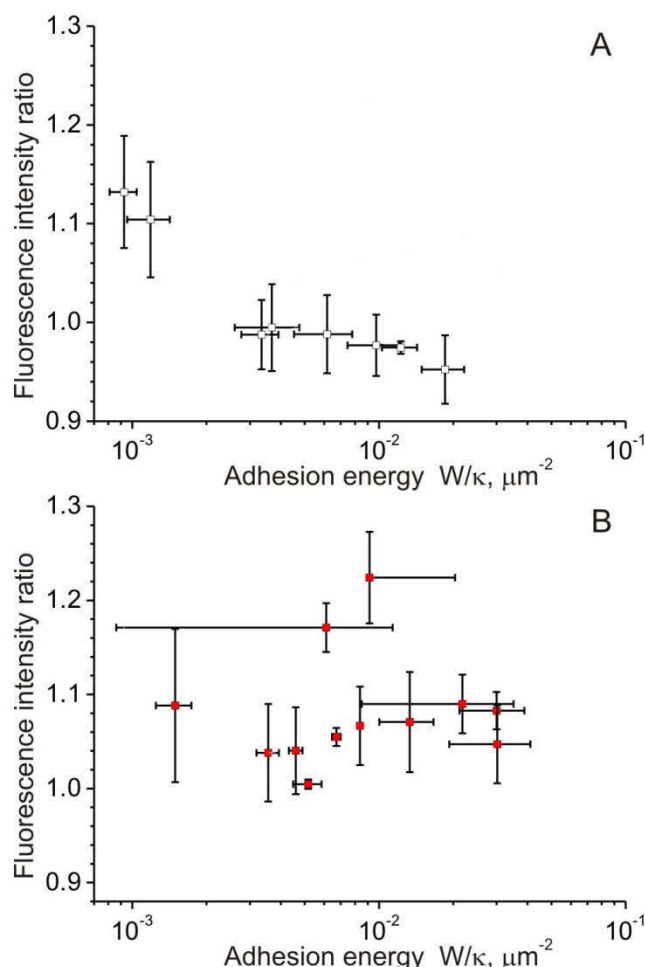


**Figure 3-11 - Ratio of fluorescent intensity measured in the adhering and free membrane segment for two different ensembles of vesicles: unquenched (A) and with quenched external leaflet (B). The vesicles were imaged at different external potentials and then the corresponding adhesion energies were calculated by the whole-contour method. In the unquenched vesicles, the dye is depleted from the adhering membrane segment with increasing adhesion. For the vesicles with quenched external leaflet (B), no such trend is observed suggesting that the applied external potential and the adhesion process induce dye redistribution only in the external leaflet of the vesicles.**

For the unquenched vesicle in Figure 3-10, the change in fluorescence intensity in the adhering membrane segment amounts to a decrease of around 12 % at the highest applied voltage. Assuming that the dye is depleted only in the outer vesicle leaflet, leaving the inner one unaltered (as also suggested by our quenching experiments), this would imply that around 25 % of the lipid dye has migrated from the adhering membrane segment to the unbound vesicle cap.

### 3.2.3 Mechanism of induced adhesion and lipid depletion

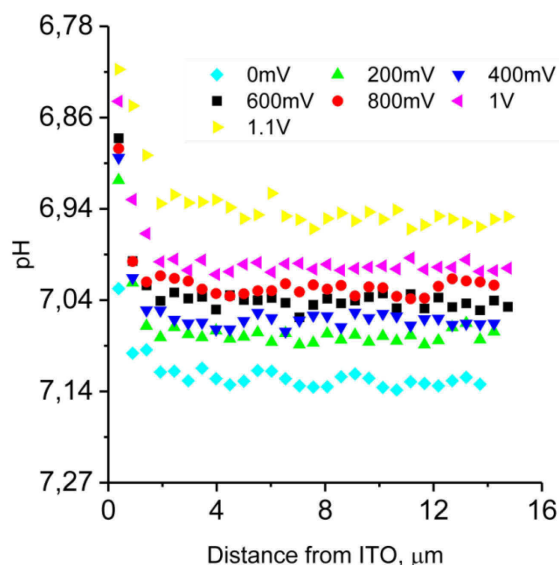


Figure 3-12 - The pH change in the buffer in the vicinity of the bottom ITO glass as a function of the external potential was measured using the pH-sensitive dye SNARF (seminaphthorhodafluor, Life Technologies) which was added at concentration of  $10 \mu\text{M}$  to the buffer. The intensity ratio between the green and red peak signal of the dye was converted to pH based on calibration measurements in solutions of known pH. The maximal decrease in pH was measured directly (sub  $\mu\text{m}$  distance) at the ITO glass surface but is still above pH 6.

The depletion of the negatively charged NBD-PG from the adhering membrane segment is somewhat puzzling. Initially, we expected enrichment of the negatively charged molecules in the adhering membrane segment due to the positive charges on the ITO electrode. This did not turn out to be the case. To explain this effect, we first need to understand which forces act on the lipid in the two membrane segments (free and adhered). We find no evidence for a significant electrostatic field inside the solution chamber, which could result in pulling the vesicle towards the electrode surface (via electrodeformation or electrophoresis). We tested this in two ways. First, we measured the electric current between the ITO glasses and the DC voltage source. In the explored voltage range, the current always stayed below  $5 \mu\text{A}$ . Taking the contact area between the vesicle suspension and the ITO glass ( $\cong 79 \text{ mm}^2$ ) and the measured conductivity of the buffer ( $\cong 250 \mu\text{S/cm}$ ), for the electric field we find about  $6.25 \text{ V/m}$ . This field strength is two orders of magnitude lower than the electric field typically needed for vesicle electrodeformation<sup>51, 80</sup>. Second, we filled the chamber with vesicles in pure sucrose solution where gravitational forces on the vesicles are absent and the vesicles are freely floating in the bulk of the chamber. Upon application of the external potential, the vesicles did not experience any drag toward the bottom electrode and no morphological changes were observed over the timeframe of hours. We therefore conclude that there is only insignificant charge transfer into the solution and that the external potential indeed mainly alters the

surface potential, which is then screened within the Debye length ( $\sim 7$  nm) in the vicinity of the electrodes. This is also corroborated by the measured pH value, which was found to be approximately constant over the used voltage range (see Figure 3-12) indicating insignificant amount of products from electrochemical reactions at the electrode. In the following we focus on short ranged forces on the ITO surface. Around neutral pH the ITO surface exhibits a negative surface charge due to dissociation of hydrogen bonds to solution. The observed adhesion might be a balance between electrostatic repulsion by the negative charges on the electrode (which would be decreased by the applied potential) and van der Waals interaction similar to DLVO theory for colloids. However, when experiments are conducted in high salt concentrations (100mM NaCl), where electrostatic contributions are largely screened, vesicles do not adhere at any applied voltage. Hence van der Waals forces alone seem not to be sufficient for adhesion in this system. Consequently, electrostatic forces are driving the observed adhesion. One needs to remember that coulomb interactions are screened by the free ions in solution and we examine this effect on basis of the Poisson Boltzmann theory of ion condensation around charged bodies in solutions. The (electrostatic) pressure between two charged plates with distance  $D$  (ignoring edge effects) with charge densities  $\sigma_1, \sigma_2$  (in the Debye Hückel limit of low surface potentials) is proportional to<sup>81</sup>

$$\Pi(D) \sim \frac{\sigma_1 \sigma_2 \cosh(\kappa D) + \sigma_1^2 + \sigma_2^2}{2 \sinh^2 \kappa D} \quad (22)$$

For large separations and oppositely charged plates, the pressure is attractive and also reflects the intuition that the attraction is proportional to charge density on either surface. In the limit of small separation the pressure goes as  $\Pi(D) \sim \frac{(\sigma_1 + \sigma_2)^2}{2 \sinh^2 \kappa D}$  and is always repulsive, also for dissimilar signs of surface charges, expect for the special case  $\sigma_1 = -\sigma_2$ . This effect can be understood by the overlap of the ion clouds as the two plates approach. Because of the requirement of charge neutralization there is always a finite number of charges between the two plates. This leads to a buildup of osmotic pressure and hence repulsion on small plate separations. The above result is derived for the boundary condition of fixed charges. In our system the charges in the adhered membrane segment are not fixed but mobile. Specifically, the vesicles exhibit an adhered and free membrane segment where lipids can exchange (constrained by the entropic and electrostatic cost of the lipid exchange). Therefore, for an adhered vesicle, there is an optimal density of charged lipids in the adhesion segment that should be close to the charge density on the ITO surface. At zero external voltage, the surface potential of the electrode is negative. The application of the external potential shifts it towards the point of zero charge (electrically neutral). The onset of electrostatic attraction is expected to start at low positive potentials (and low surface charges on the ITO electrode). The lipid bilayer has a rather high surface charge of about -0.04

$\text{C/m}^2$ . Hence the adhered membrane segment should be depleted of negative charges to match the surface charges on the ITO electrode as observed in our experiment.

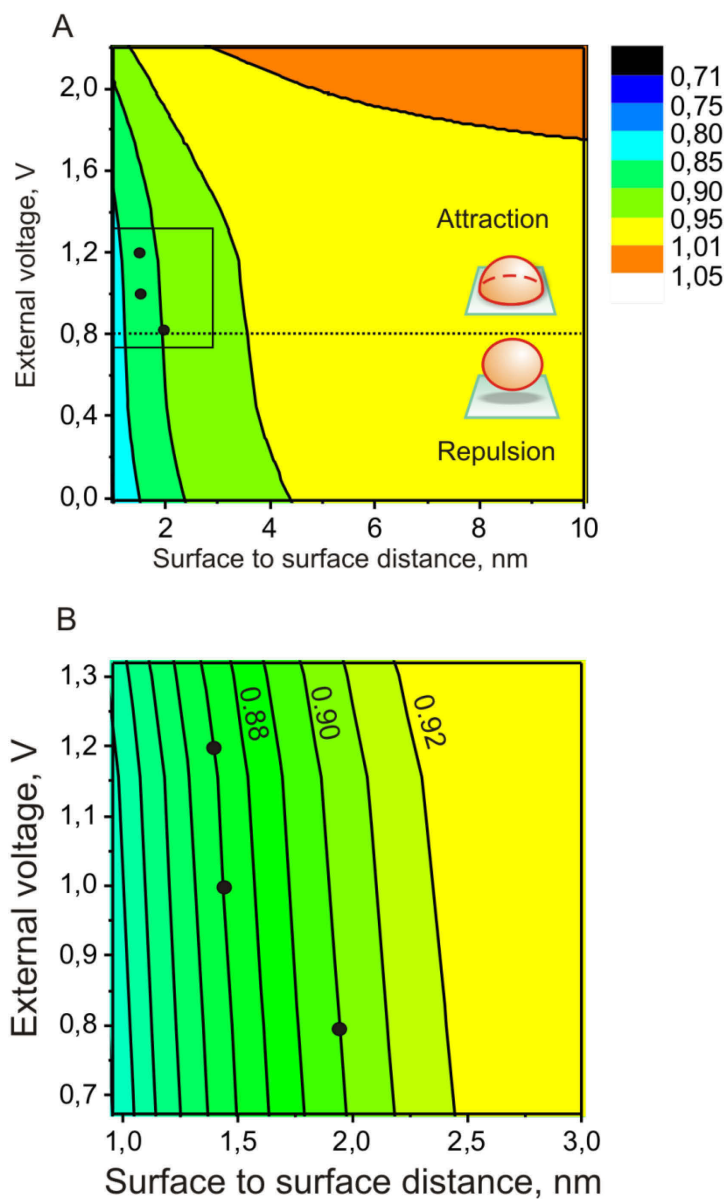


Figure 3-13 - (A) Color code and contour lines show the simulated normalized composition of the adhering membrane segment at different bilayer-surface distances and external voltages. The broken line indicates the onset of adhesion as experimentally measured (B) Insert shows the observed experimental fluorescent intensities (Black dots)

The effect of surface charge regulation due to lipid mobility was included in the work of Ben-Shaul et al<sup>71, 72</sup> for the case of DNA and protein absorption on a lipid bilayer. We numerically solved the model for our geometry and parameters of a planar adhering membrane segment. The only free parameter is the voltage where adhesion is induced (in other words the potential of zero charge, which we set to 0.8V, see Figure 3-8). Depending on the surface charge on the electrode (which is set by the external

potential) and the bilayer-surface distance different membrane composition are obtained and color-coded in Figure 3-13. As expected from the reasoning above, a wide range of potentials and membrane-surface distances exist, where adhesion to the positively charged electrode is induced, but negatively charged lipids are expelled from adhering membrane segment. For reference the measured fluorescent intensities at different voltages are also shown, note that we did account for the depletion of the outer bilayer only, as measured independently by the quenching experiments. The extracted bilayer-surface distance lies between 1 and 2 nm and is in good agreement with previous studies on supported lipid bilayers<sup>82</sup>. Please note that other membrane-surface forces like undulation-, hydration- and van der Waals-forces are not considered here and hence we do not calculate a local energetic minimum but only the solution to the PB equation with fixed surface potential and membrane-surface distance.

### 3.3 Conclusions and Outlook

We developed a novel approach to induce adhesion of GUVs to a planar substrate based on the application of an external potential. The adhesion strength can be smoothly regulated by the turn of the knob of the DC source. To calculate the adhesion energies, we used a method which relies on the overall vesicle shape as obtained via confocal microscopy. This is advantageous as adhesion energies of GUVs are usually calculated by the contact curvature, which is only accessible by sophisticated techniques such as reflection interference contrast microscopy and for high adhesion energies. In the current study, the adhesion energies are in the weak adhesion regime because of the limited voltage range explored. This limitation is due to the onset of an electrical current by the initiation of electrochemical reaction on the substrate surface at higher potentials. The limiting voltage is a property of the used electrode material (ITO) and, presumably, can be tuned by passivation of the surface by e.g. a polymer layer as used in electrowetting applications. Our approach for inducing controlled and tunable adhesion of vesicles to a substrate is facile and easy to implement and depending on the electrode polarity, it should be also applicable to positively charged membranes.

We found depletion of the negatively charged membrane species NBD-PG, between the unbound segment and the adhesion zone of the vesicle and have shown that this is consistent with a theory on the Poisson Boltzmann level which explicitly accounts for lipid mobility. Quenching experiments have shown that only the outer leaflet composition is changed by the interaction with the support. This suggests that (compositional) interleaflet coupling is weak in fluid DOPC/DOPG membranes. We also note that the asymmetric lipid distribution should generate nonzero spontaneous curvature in the membrane. Our results imply that even relatively weak nonspecific forces can induce asymmetry and thus spontaneous curvature in biomimetic and

biological membranes therefore remodeling membrane compartments<sup>83</sup>. Finally we have shown that diffusion in the adhering membrane segment is not at all or only slightly hindered compared to that in the unbound membrane. This result might be also relevant for experimental approaches employing supported membrane bilayers (as e.g. in studies based on total internal reflection fluorescence). Compared to commonly used SLBs, in our system there is only a minimal membrane-surface interaction and the bilayer is practically free. We also note that the vesicles are effectively immobilized on the ITO surface and do not move due to convection, which would otherwise negatively affect measurements. This immobilization may in practice be employed in studies of membrane properties. In the next chapter we use the here developed method in the study of phase separated vesicles.

## 4 Adhesion of multicomponent vesicles

Vesicles with phase separated domains have been extensively studied in their morphology and phase changes due to various specific and non-specific molecular interactions<sup>9, 84-89</sup>. While they are an interesting and complex system to study on their own, a lot of interest has emerged in them, as a model for the plasma membrane of biological cells. While the existence of, presumably, nanoscopic domains in the plasma membrane reassembling the liquid ordered phase found in simple three component model membranes in thermodynamic equilibrium is under discussion<sup>33</sup>, giant unimellar vesicles (GUVs) with microscopic domains are certainly an interesting model for the plasma membrane, which exhibits inhomogeneous distribution of its components on many length and timescales (cell polarization). In biological systems, cells are almost never isolated, but in contact with other cells or the extracellular matrix. However, often studies on biomimetic membranes are conducted using free floating GUVs or completely adhered supported lipid bilayers. Only a few studies were conducted on adherent GUVs which exhibit phase separation. Unspecific adhesion of vesicles exhibiting fluid-fluid coexistence was studied in Ref.<sup>10</sup> and some redistribution of membrane domains was observed. Zhao, Wu and Veatch<sup>85</sup> studied the interaction of GUVs adhering via specific linkers to a supported lipid bilayer. To our knowledge the non-specific adhesion of phase separated multicomponent GUVs to planar substrates was not studied experimentally, even if recent theoretical results indicate strong effects<sup>28</sup>. In the crowded environment of inter and extracellular space, membranes will always exhibit some degree of non-specific interaction. To study such effects, we induce adhesion of GUVs by an external electrical potential, which enables controlled and reversible studies on single vesicles (Chapter 3)

Before we present the results, we first recap some nomenclature. Consider a vesicle close to a planar wall. If the interaction between the wall and the membrane is attractive, the vesicle partially “wets” the surface. Therefore, two segments are obtained, the spherical free membrane cap and the bound segment. If the attraction is due to the interaction between the lipids and the surface, the lipids will have a different chemical potential in the free and adhered segment. If now the vesicle consists of two or more lipids species, the lipids will have a difference in their chemical potentials *between* each other. Hence, the composition of the two segments should then reflect differences in chemical potential. In the case of binary mixtures and strongly adhering vesicles, the behaviour was systematically studied theoretically<sup>28</sup>. It was found that adhesion can suppress, induce or confine phase separation in either membrane segment. Here, we study the interaction of GUVs composed of mixtures of DOPG/eSM/cholesterol close to a surface with variable charge. Complex remodelling of the membrane segments was found depending on adhesion energy, lipid composition



and temperature. We find that GUVs can undergo a change in their phase state, budding transitions and altered lipid diffusivity when adhesion is induced.

### 4.1 Methods

#### 4.1.1 Determination of the miscibility temperature of free vesicles

Multicomponent vesicles are prepared as described in Chapter 3.1.1 and left to sediment in the chamber shown in Figure 4-1. The chamber consists of two ITO glasses which are sandwiched together and separated by a 0.5mm thick spacer. To study miscibility temperature of non-adhering vesicles, no external voltage generator was connected (open circuit potential) and the chamber was brought into thermal contact with a temperature controlled water bath. Usually the temperature was changed in 1-2°C steps and vesicles were left to equilibrate for 5 minutes between temperature steps. Calibration measurements have shown, that the temperature of the vesicle suspension is within 0.1°C of the temperature of the connected water bath. Vesicles were observed by epifluorescence on a Zeiss Axiovert 200 using a 40x0.6 air objective. The temperature at which 50% of the vesicle population is phase separated was noted as the miscibility temperature. Depending on the vesicle composition, the transition region was found to be rather narrow (1-2°C), where between 10 and 90% vesicles are phase separated or homogenous. Compositions close to the phase boundary exhibited a broader distribution in their composition. This was sometimes exploited to study vesicles of slightly different compositions within one batch. For example, even at room temperature, a significant fraction of 2/6/2 GUVs exhibit domains, indicating a slightly higher fraction of DOPG. In this way a wide range of compositions can be studied.

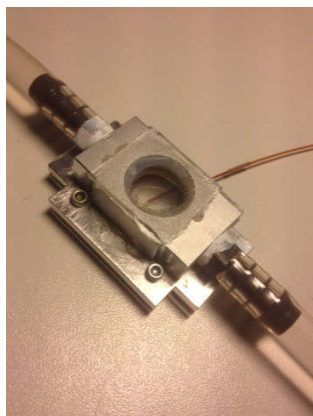


**Figure 4-1** – Experimental chamber. In the center, the two ITO glasses can be seen. The temperature bath is connected on the top. The temperature probe on the right is placed in the chamber only for calibration.

#### 4.1.2 Study of phase changes in adhering multicomponent GUVs

To study adhesion, GUVs were usually left to sediment onto the ITO surface and the external voltage was changed gradually from 0V up to 1.4Vdc. In some cases, the voltage was also stepped up from 0V to 1.2Vdc to induce adhesion instantly. If not indicated otherwise, vesicles were left to equilibrate after adhesion is induced for up to 15 minutes. In general, morphological changes appear either fast (minutes) or vesicles are stable during the experimental time of one to two hours. In some adhering vesicles the phase miscibility temperature was measured. Here, the miscibility temperature of the free vesicle was measured first as described above. Adhesion at 1.2Vdc was induced just above the measured miscibility temperature. Subsequently the

temperature was lowered and the new miscibility temperature at which domain nucleation in the two segments was observed was recorded.

### 4.1.3 Intensity measurements

We have measured the intensity of the membrane dye DiIc18 in both the adhering and free membrane segment. For these measurements we have only considered vesicles which exhibit either homogenous fluorescence or a  $I_d$  domain on the cap. We measured the fluorescent intensity in normal direction to the ITO surface in both the adhering segment and pole of the free segment. In this way we could exclude polarization effect of the dye or effects associated with different sizes of the membrane segment in the confocal volume.

## 4.2 Results

### Miscibility temperatures in DOPG/eSM/chol membranes

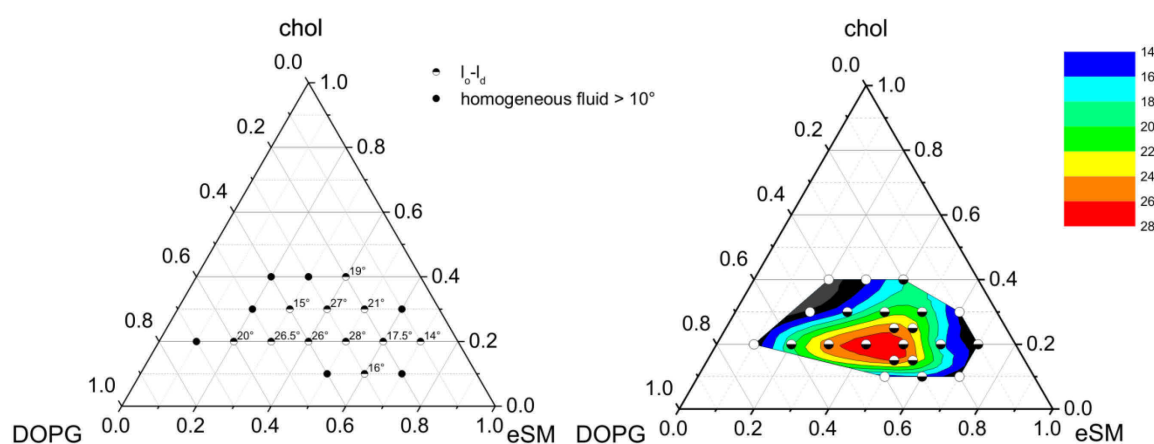


Figure 4-2- Left: Measured miscibility temperatures for different membrane compositions in free (nonadhering) GUVs. Filled points indicate no observed macroscopic phase separation down to 10°C. Right: Interpolation between data points, colours indicate temperature in °C

First we studied the miscibility temperatures of the fluid-fluid coexistence region of the DOPG/eSM/chol mixture (Figure 4-2) in free GUVs. The miscibility temperature inbetween the experimental data points was then determined by linear interpolation and subsequent smoothing by B-splines. In this way, continuous phase boundaries in the explored temperature range can be obtained. The algorithm does not take into account any thermodynamic rules, which has to be done manually. The boundary extracted in this way at 25°C is shown in Figure 4-3.

#### 4.2.1 Adhesion induces heterogeneous responses in phase separated GUVs

When the GUVs are left to sediment onto an ITO surface one can modulate the charge of the ITO surface by an external electric potential and induce adhesion, as described in Chapter 3.2.1. We first keep the temperature constant at 25°C and study the morphology of the vesicles by confocal microscopy (Figure 4-3). Domains of different

phases can be visualized by partitioning of the fluorescent dye DiIc18 that is incorporated into the membrane. DiIc18 strongly partitions into liquid disordered domains.

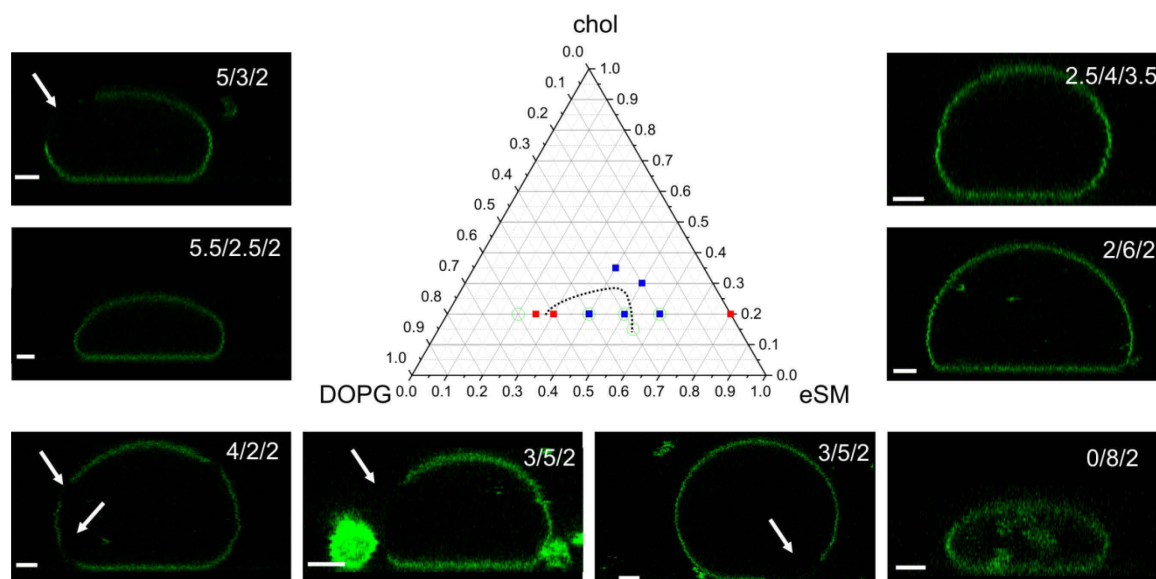


**Figure 4-3-** Different morphologies (vertical confocal cross sections) of adhering vesicles obtained during experiments. Arrows indicate liquid ordered domains. In the Gibbs diagram, blue points indicate compositions where no change in DiIc18 partitioning between the bound and unbound segments was found, and red where partitioning between the segments was measured. Green circles indicate compositions where no significant change in the miscibility temperature between free and adhered vesicles was found. The dotted line is the coexistence boundary as found from Figure 4-2. Scale bars 5 $\mu$ m, all voltages between 1.1 and 1.3Vdc

As the vesicle morphology is changed from being close to a sphere, to a shape close to a spherical cap, some domain redistribution is always observed. In some vesicles also a clear change in phase state due to adhesion was observed by the disappearance of optically resolvable domains. (Figure 4-4 left). In other vesicles both membrane segments however appear to remain in the same phase state as before adhesion. This is reflected in a vesicle of different composition (Figure 4-4 right), when the temperature was raised 1-2°C above the transition temperature and then lowered again. Domain nucleation can be observed at the same temperature (<0.1°C) in both segments at the same miscibility temperature as measured before adhesion. This indicates that both membrane segments are in the same phase state. It was difficult to find a single composition which would reproducibly change its phase state due to adhesion. A possible explanation would be an effect of membrane tension. The initial GUV tension is heterogeneous within one population at the beginning of an experiment due to the preparation method of the vesicles, however theoretical and experimental results indicate only a small effect of tension on membrane phase state<sup>90</sup>. Other effects complicated the study of adhesion induced changes in phase state. We found that vesicles undergo budding transitions in the cap, close to the rim of the

adhering segment. These transitions are described in detail further down. Because budding changes the overall vesicle composition, the final vesicle composition of the mother vesicle is not known exactly. Due to long observation times of individual vesicles, artefacts due to lipid oxidation by the fluorescent dye also cannot be completely excluded, even if dye concentration was low and illumination was kept minimal. In the following, we study the different phenomena in more detail.

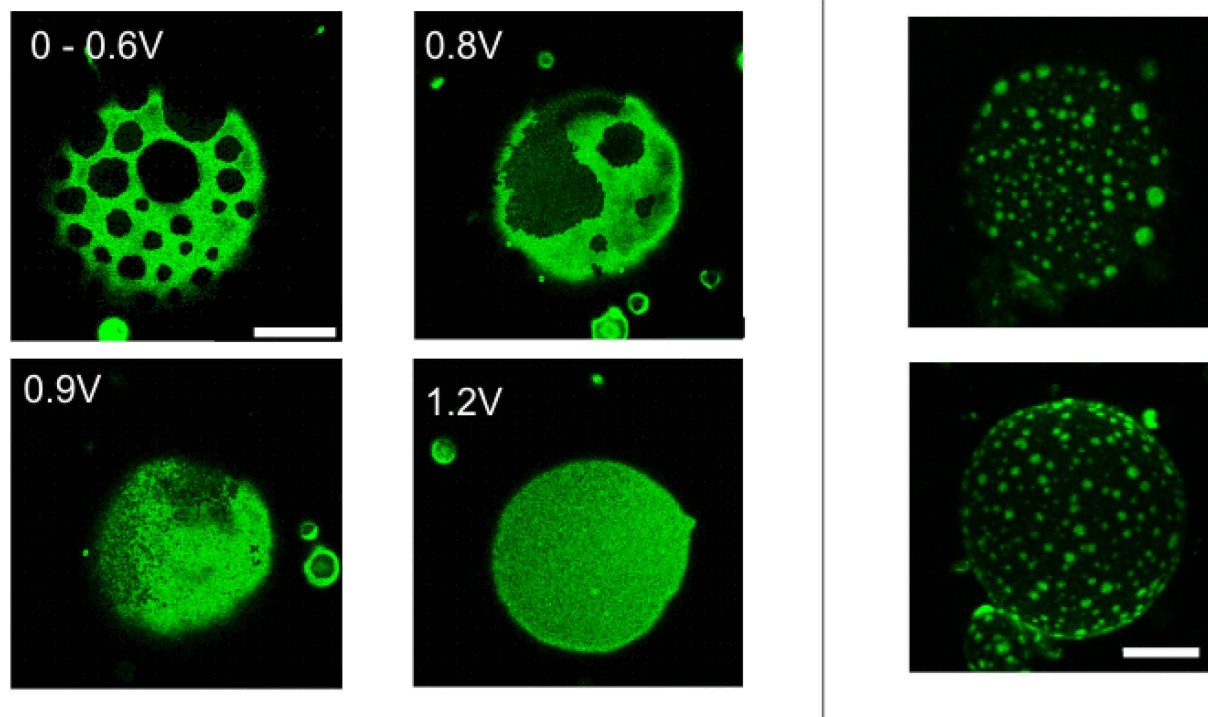
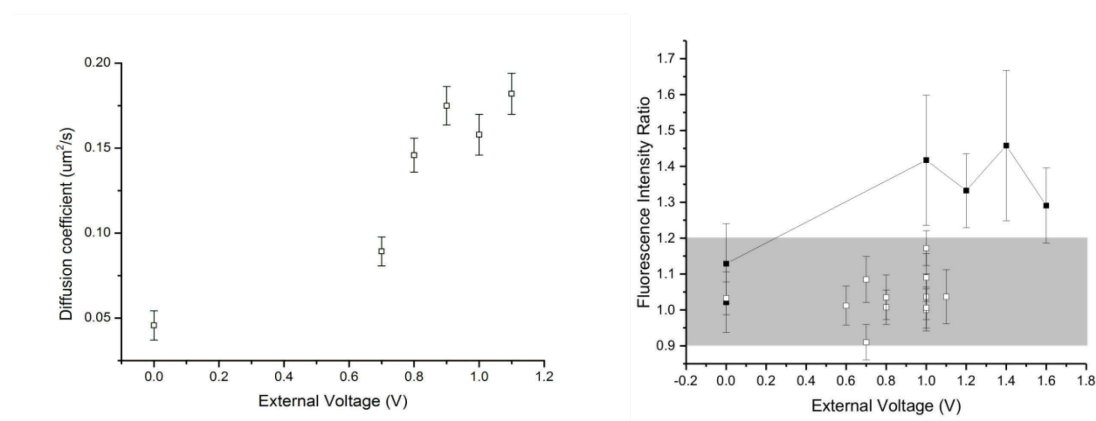


Figure 4-4 - Left: The adhering membrane segment of a deflated GUVs (3/5/2). The vesicle undergoes domain coarsening and subsequent disappearance of domains upon adhesion. The voltage was ramped up fast (<5minutes). Domains in the free segment also disappear (not shown). Scale bar 5 $\mu$ m. Right: Adhering vesicle (at 1.5Vdc) after a temperature cycle just above the miscibility temperature of the free vesicle. Upper: (x,y) view of the adhering membrane segment. Lower: Maximal projection of the free segment. Upon cooling domains nucleate in both segments. Scale bar 10 $\mu$ m.

#### 4.2.2 DiIC18 redistribution by adhesion depends on the initial membrane composition

We studied the fluorescence intensity of the phase sensitive dye DiIC18. When the dye is included in DOPC:DOPG 8:2 GUVs, which are fully miscible in all proportions, we see no significant change in fluorescence over the whole range of adhesion energies (up to about  $5 \cdot 10^{-9} \text{ J/m}^2$ , see Chapter 3.2.1 ). This is advantageous, because it indicates that the dye interacts only minimally with the surface. This is probably because DiIC18 is buried in the hydrophobic core of the membrane as indicated by MD-simulations (see Figure 2-2)<sup>40</sup>. The insignificant dye partitioning also confirms that the DOPC:DOPG vesicles do not change their phase state due to adhesion, as it is expected. We then studied vesicles made of eSM:chol. GUVs made of the composition 8:2 appear homogenous and are absent of optically resolvable domains. At room temperature,

this composition is close to the miscibility gap and this is reflected in a broad distribution of the DiIc18 dye between vesicles. However the dye distribution on individual (free) vesicles is homogenous. In contrast to the DOPC:DOPG vesicles, adherent eSM:chol vesicles do show an adhesion induced dye partitioning between the two membrane segments (Figure 4-5 right). The partitioning of DiC18 into the adhering segment indicates that compared to the unbound cap, here the membrane is more fluid, in other words enriched in cholesterol. To further support this finding, we measured by FRAP the diffusion coefficient in the adhering membrane segment at different adhesion energies (Figure 4-5 left). For free GUVs we find good agreement with the diffusion coefficient of eSM:chol membranes of similar composition measured by FCS<sup>91</sup>. Strikingly, compared to values measured for free (nonadhering) GUVs, the diffusion coefficient is more than three times higher in the adhering membrane segment after adhesion is induced. The increase in diffusion coefficient is fully consistent with the increase in cholesterol content. The magnitude of change seems to be unexpectedly high, but can be understood by the initially low cholesterol content. Indeed, if we assume that the eSM content changes by only 25%, the cholesterol content is doubled, the membrane should be then far inside the liquid phase in good agreement with published values<sup>91</sup>. In summary, we find that adhesion in this system is capable of changing the composition of eSM:chol membranes and the membrane marker DiIc18 is a sensitive to membrane phase state by partitioning into the two vesicles segments.



**Figure 4-5 - Left:** Diffusion coefficient of DiIc18 as measured by FRAP in eSM:chol 8:2 membranes at RT, data is shown from a single representative vesicle. **Right:** Partitioning of the membrane fluidity marker DiC18 in DOPC:DOPC (squares) and eSM:chol (line) membranes at RT. Grey indicates insignificant changes.

Next we looked at the phase state of the two segments in membranes with more complex composition, namely the ternary mixture DOPG:eSM:chol. As expected, the DiIc18 fluorescent intensity is not significantly changed during adhesion in compositions far away from the fluid-fluid coexistence region (Figure 4-6 A), which reflects the behaviour of fully miscible DOPC:DOPG membranes. However, we also find

only minute change in the fluorescent intensities of the liquid ordered domains in phase-separated GUVs for 4/4/2 and 3/5/2 membranes. (Figure 4-6 B). This is in contrast to the expectation of a strong modulation of the phase state due to adhesion. It could be argued that the employed technique is not sensitive enough but we note that we did register the composition change in eSM:chol vesicles by the same method. Measurement of the miscibility temperature of free and adherent vesicles close to compositions in question, indicated by green circles in Figure 4-3 also indicate a small change in phase state: We measured the miscibility temperature of the free vesicles and the miscibility temperatures of adhered and unbound membrane segments in adhering vesicles. Modulation of the adhesion energy by an external potential on the same vesicle, enables us to measure these quantities before and after adhesion. Again we find that transition temperatures are not changed significantly ( $<1^{\circ}\text{C}$ ) and domains nucleate in both free and adhered segment at the same temperature ( $<0.1^{\circ}\text{C}$ ). Together with the results of DiIC18 fluorescence we conclude that vesicles of the composition 4/2/2 and 3/5/2 are (thermodynamically) stable against adhesion-induced composition change and hence phase state.

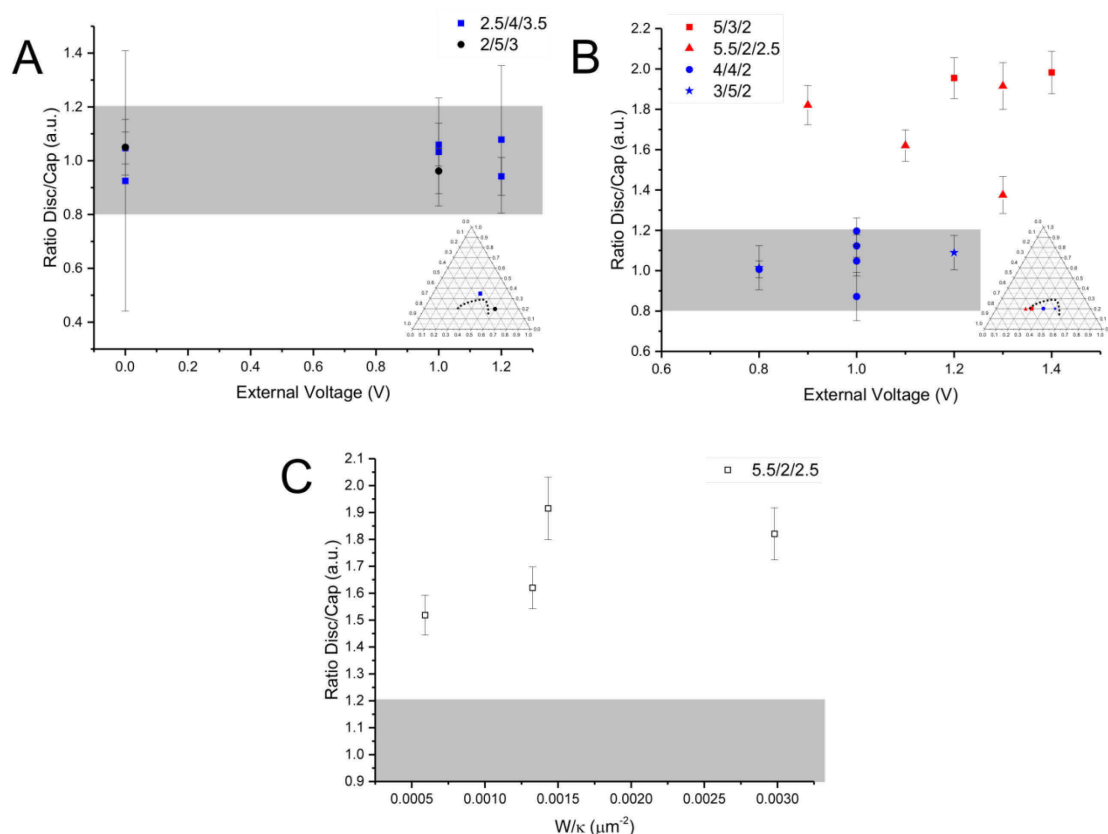


**Figure 4-6 – A)** No significant changes of DiIC18 partitioning between the two segments, adhered and unbound, in two compositions that appear homogenous at RT **B)** Only Vesicles close to the critical composition show partition of the membrane marker DiIC18. Each data point is an individual vesicle. **C)** DiIC18 is enriched in the adhering membrane segment with increasing adhesion energy. Data obtained from an individual vesicle at different voltages.



In contrast, we find a significant change in DiIc18 intensity in the compositions 5/3/2 and 5.5/2.5/2 (Figure 4-6 B). While the exact critical point in the DOPG/eSM/chol system is not known, the two composition are close to the critical point of DOPC/eSM/chol 5.2/1.5/3.3<sup>7</sup>. Generally, we find enrichment of the DiIc18 in the adhering membrane segment. Dye distribution is found to be rather heterogeneous within one batch. However, when the fluorescent signal of an individual vesicle at different adhesion energies is followed, a clear trend is observed (Figure 4-6 C). Consistent with the eSM:chol results, DiIc18 is enriched in the adhering segment. We would expect a difference in the miscibility temperature of the two segments in such a vesicle (not measured).

### 4.2.3 Domains coarsen in the adhering membrane segment

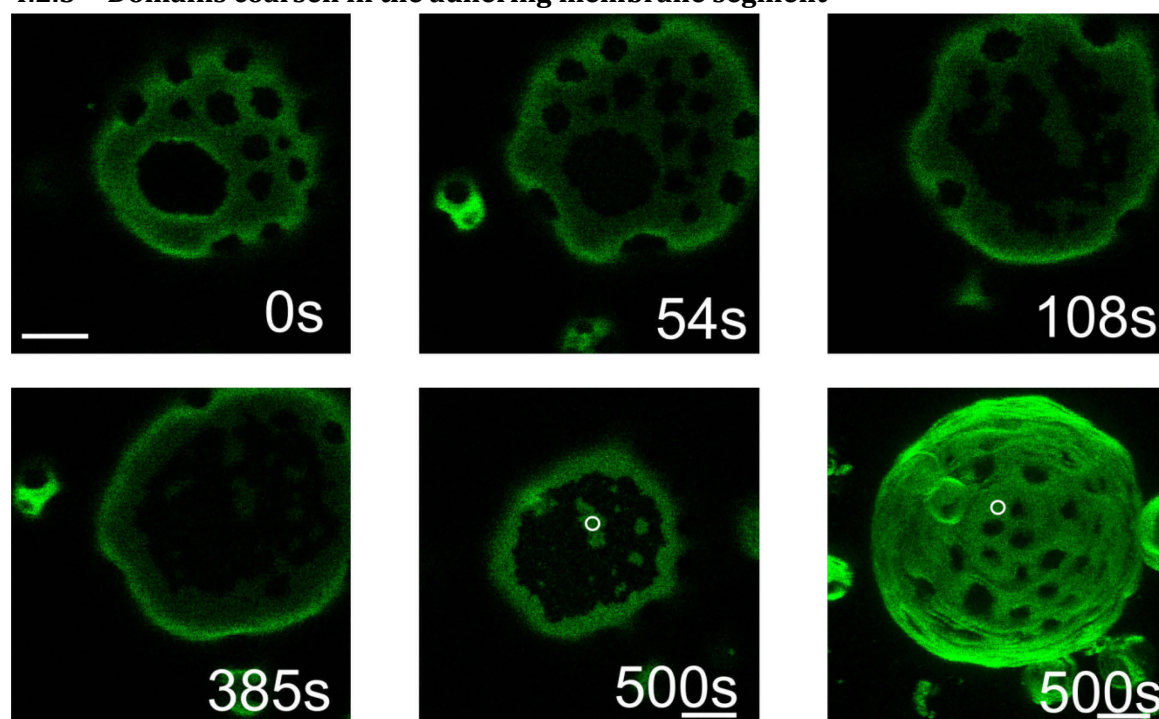


Figure 4-7 – Confocal images(x,y) of the adhering segment of a vesicle exhibiting small domains. The voltage is ramped up from 0V to 1.2Vdc at 0s. The white circle indicates regions with equal DiIc18 intensity. Scale bars 5μm. The last two images show the adhering segment and the maximal projection of the free segment.

Vesicles, which exhibit small domains when adhesion is induced, can undergo domain coarsening as shown in Figure 4-7. At t=0 the adhesion is induced and within minutes the vesicle spreads on the surface and small domains fuse. It is known, that small domains can be kinetically trapped in deflated vesicles due to differences in bending rigidities<sup>92</sup>. As the membrane adheres it acquires a flat morphology which promotes domains fusion. The  $I_o$  domain (dark) is now trapped in the adhesion zone and does not diffuse into the free segment. This is probably because the liquid ordered phase is stiffer than the liquid disordered phase, which makes it energetically preferable to obtain a flat morphology<sup>84</sup>. This domain coarsening is not necessarily an indication of a

change in phase state. Indeed, when the fluorescent intensity in the two spots indicated by the white circles is compared, almost identical values are obtained.

#### 4.2.4 Adhesion-induced budding transition depend on the membrane phase state

When homogeneous vesicles that are made of compositions far away from the miscibility gap and adhesion energies are high, buds are often formed close to the contact line of the adherent GUVs. Usually, they appear as outward spherical buds, which are connected to the mother vesicle (Figure 4-8). They can also diffuse along the membrane surface and sometimes appear to detach. Additionally, their fluorescence intensity becomes inhomogeneous across different buds, strongly indicating that they are of heterogeneous lipid composition. Indeed, one can directly observe sorting of membrane components between the mother vesicle and bigger buds. The mother vesicle shown in Figure 4-8 (right) undergoes demixing at a higher temperature than the connected bud. The budding process is consistent with the quenching experiments conducted in Chapter 3.2.2, which show that adhesive forces only act on the outer membrane leaflet. This will induce spontaneous curvature in the bilayer, which can relax by a budding transition<sup>93</sup>.

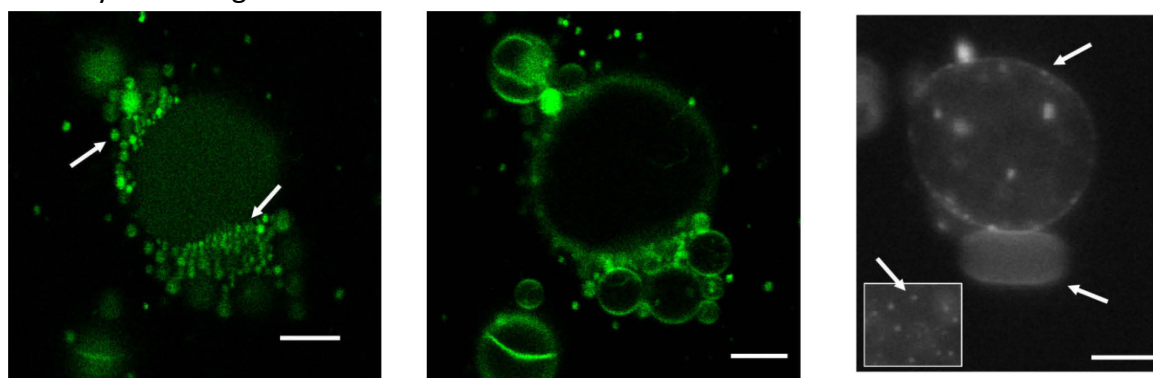


Figure 4-8 – Left, Middle: 5.5/2.5/2 @ 1.3Vdc, RT, Adhering membrane segment. Adhesion induces the formation of buds with heterogeneous DiIc18 densities. Buds are typically between 1 $\mu$ m and 3 $\mu$ m Right: 2/6/2 18 °C EPI Fluorescent micrograph indicates domains in mother vesicle but homogenous appearance of the bud as the temperature is lowered, insert shows the focal plane of the upper pole of the mother vesicle, domains are indicated by an arrow. Scale bars 10 $\mu$ m

In the previous section, we have established that phase separated vesicles are stable against adhesion-induced phase change and compositional differences between the two segments are expected to be small when far from the critical point. Indeed, budding is not observed for vesicles deep within the two phase coexistence region. Close to the critical point, phase separated vesicles show only a few buds in the contact line. We find direct experimental evidence for the proposed trapping of membrane composition: The vesicle in Figure 4-9 is adhering at room temperature and only moderate budding is observed (left). The vesicle is then heated to about 40°C and left to relax back to room temperature. Now the vesicle exhibits strong budding and macroscopic phase separation disappears in the adhesion zone (right).



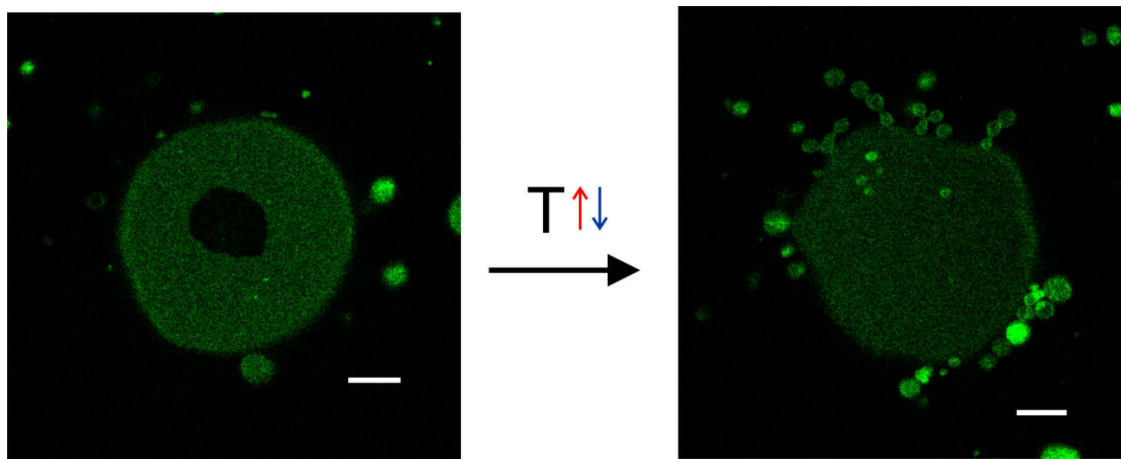


Figure 4-9 – Adhering membrane segment of a vesicle of composition 5/3/2 @ 1.3Vdc before (left) and after (right) the temperature is cycled above the main melting temperature and back to RT. Scale bar 10 $\mu$ m.

## 4.2.5 Liquid ordered domains in the contact line of adherent vesicles

To our surprise, vesicles of the 4/4/2 composition can exhibit domains, which presumably are in the liquid ordered phase, at the contact line (Figure 4-10). These domains are liquid, as seen by their fluctuating boundaries and diffuse only in one dimension (along the contact line); indeed if two domains meet they fuse as expected for fluid domains. Some vesicles exhibit a closed domain (circular stripe) along the rim of the contact line. This configuration is stable on the timescale of hours.

## 4.2.6 Domains with reduced contrast close to the critical composition

In a fraction of vesicles belonging to the 5/3/2 composition, domains with about half the fluorescent intensity of the liquid disordered phase can be observed in the adhesion segment (Figure 4-10 right). One can speculate that these domains only exist in one membrane leaflet.

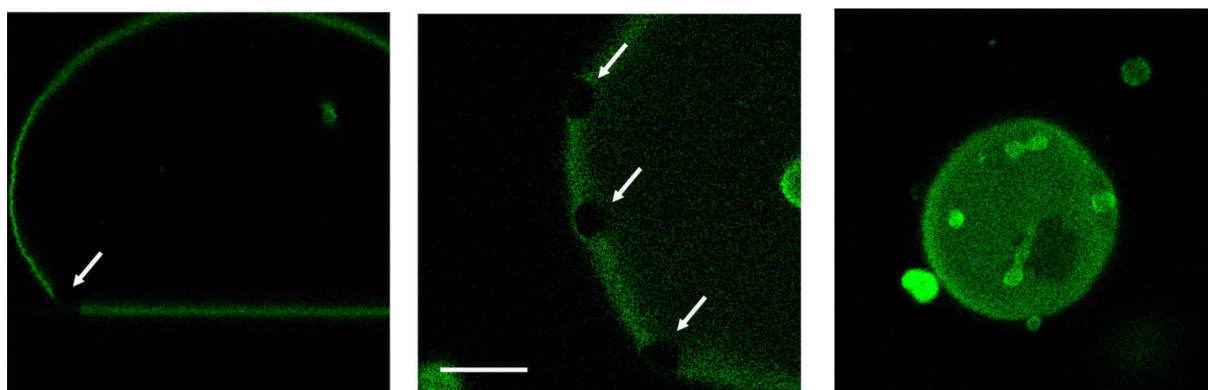
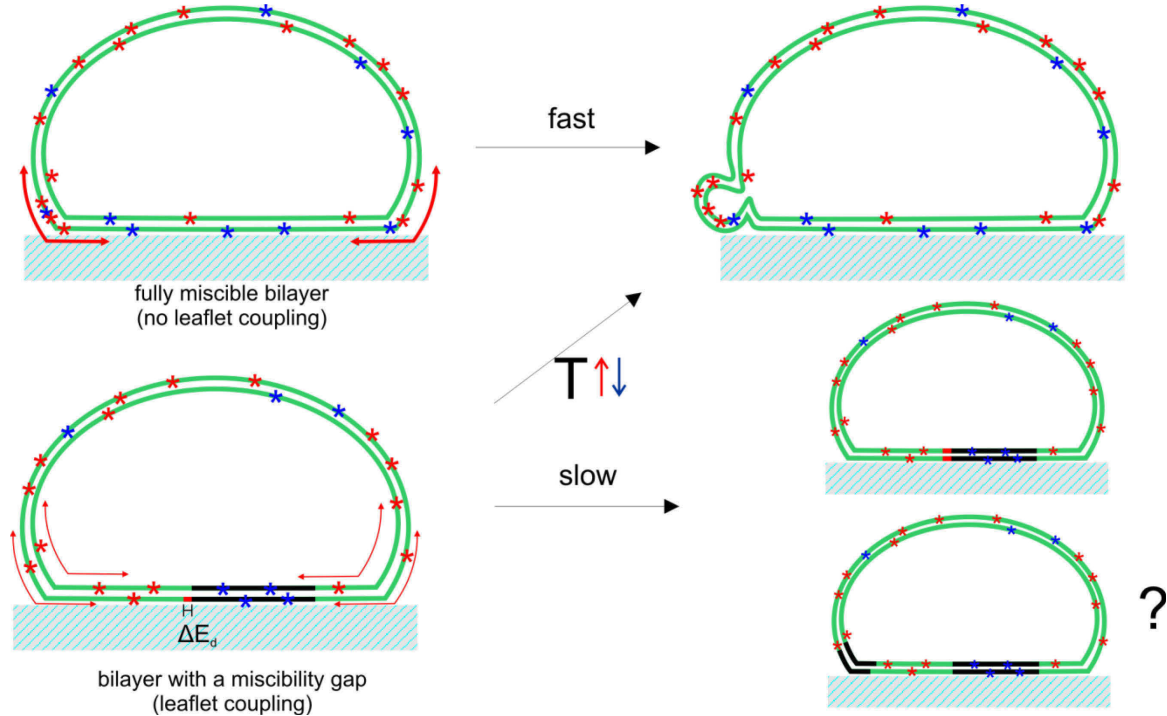


Figure 4-10 – (Left, Middle): Confocal side view (x,z), adhering membrane segment (x,y) of a vesicle (4/2/2), arrows indicate liquid ordered domains. Right: Adhering membrane segment (5/3/2) with a domain of about half the DiIc18 fluorescence intensity of the liquid disordered phase. Scale bar 10 $\mu$ m

### 4.3 Discussion

#### 4.3.1 Upon adhesion, membrane phase state and composition are significantly changed only close to a critical point



**Figure 4-11 - Sketch of the observed compositional and budding transition.** Stars indicate two different lipid species. Left: Arrows indicate lipid flows. The lower right image indicates the observed liquid ordered domain in the contact line. The mismatch energy due to sorting lipid in only the outer leaflet is sketched in the lower left.

The phase state of lipid bilayers in the liquid-liquid miscibility gap depends on various stimuli as salt, lipid charge and protein absorption<sup>8</sup>. This is of little surprise as lipid-lipid interaction energies are small and e.g. salt directly affect area per lipid and hence phase state. In other cases modulation of the membrane phase state is only observed close to a critical point, for example by specific adhesion of GUVs by linkers or the absorption of a protein crystal coat on GUVs<sup>94</sup>. We also observe that the phase state of DOPG/eSM/chol seems to be surprisingly robust when vesicles are far from the critical point. We therefore wondered what determines this stability. Adhesion in our system only acts on the outer leaflet lipids directly (as we have shown in Chapter 3.2.2). Recent theoretical and experimental results show that lipid bilayers of phase separated membranes show compositional coupling between the two bilayer leaflets. While the molecular mechanisms are not completely understood one can define a mismatch energy which depends on the change in composition  $\phi$  from the relaxed state  $\phi_0$ ,  $E_d = \Lambda(\phi - \phi_0)^2$ , with the coupling constant  $\Lambda$  in the order of  $10^4 \text{ k}_B\text{T}/\mu\text{m}^2$ <sup>95</sup>. We estimate the sensitivity of our methods to assess phase state differences to about 10% compositional change in the segments. The mismatch energy is then magnitudes bigger than the adhesion energy in our system of  $E_d \gg W \approx 2 \text{ k}_B\text{T}/\mu\text{m}^2$ . We can therefore

expect that the mismatch energy does play a role when phase separated vesicles adhere. Figure 4-11 shows a speculation how such a mechanism could work. We know that the electrostatic interaction, which we modulate in our system, only directly affects the lipids in the outer leaflet in DOPC:DOPG membranes and we have no reason to believe that this is different in the more complex DOPG:eSM:chol membranes. We also know, that lipids will redistribute according to their energetic preference between the two segments in completely fluid DOPC:DOPG membranes, adhered and unbound. This will lead to a lipid flow between the two segments (shown in the upper part Figure 4-11). At the contact line the compositional gradient between the two flows will be biggest. One can imagine the contact line between two coloured water streams which meet in a channel and induce turbulence. In analogy the lipid composition is highly heterogeneous and dynamic at the contact line and differs from the composition of the inner leaflet, all leading to the nucleation of buds. Additionally, the higher membrane curvature and proximity to the adhesive surface in the contact line could also contribute to the budding. We directly observe the heterogeneous DiC18 distribution in buds. In contrast, if one now considers a phase-separated vesicle which is adhered, the lipid flow is restricted by the mismatch energy. When an individual lipid, which exhibits some preference for the adherent segment, diffuses into the adhering segment, it lowers its energy by the interaction with the surface; however the compositional coupling makes the net energetic contribution unfavourable. Only when two lipids of the same adhesive species diffuse in a coordinated fashion into the adhering segment, the energy of the system is minimized. But since diffusion in the both leaflets is presumably uncorrelated, this is an unlikely, hence a slow process (lower part of Figure 4-11). This leads to an energetic barrier which traps the two membrane segments in their composition. Additionally, when the composition of both leaflets has to change, this imposes a higher total entropic cost which has to be balanced by the adhesive forces. Importantly, theory predicts that lipid bilayer coupling diverges close to a critical point<sup>96</sup>. This is fully consistent with our observations, where change in membrane phase state is only observed close to a critical point. Other results are also supportive of this mechanism. We observe budding only when membranes are far from the liquid-liquid coexistence region in their composition or by thermal quenching. The slow equilibration and hence slow lipid exchange between the segments in phase separated adherent GUV could also trigger the observed nucleation of domains in the contact line, which is otherwise difficult to explain due to the high bending rigidity of liquid ordered domains.

#### 4.3.2 Relevance to the immunological gap: Dynamic budding transition due to lipid flows between segments

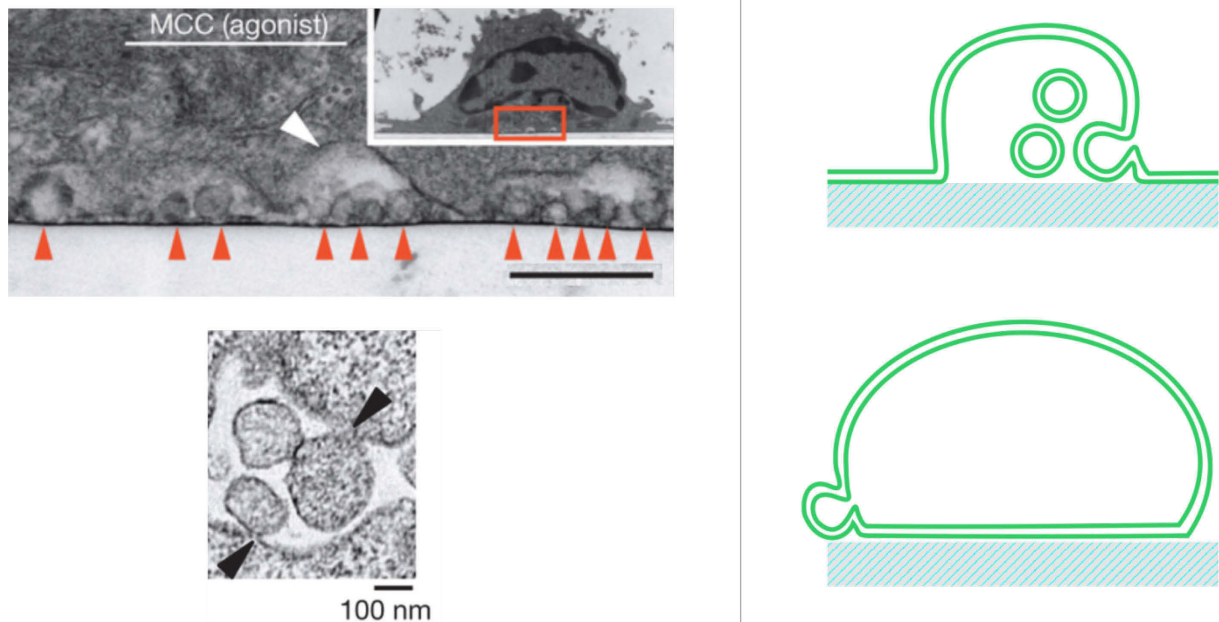


Figure 4-12 – Left: Figures adapted from Choudhuri, et al.<sup>97</sup>. TEM micrograph of the immunological synapse model. Red arrows indicate extracellular buds, white arrow the plasma membrane. Scale bar 500nm. Lower image: Buds are connected by a neck in the contact line when the ESCRT-III machinery is knocked out. Right: Membrane morphology extracted from the TEM (upper) and vesicle morphology in this work (lower). Not to scale.

Somewhat independent of the mechanism proposed above for bistable budding transition of membrane exhibiting domains, the observed phenomena can be compared to biological systems. Recently, extracellular buds in the model of an immunological synapse of T-Cell and antigen presenting cells were described (Figure 4-12)<sup>97</sup>. Here T-Cells adhered to a supported lipid bilayer presenting MCC-I-E and ICAM-1 proteins and complex reorganization of surface expressed T-Cell receptors (TCRs) can be observed. Extracellular vesicles enriched in TCRs are found in the extracellular space in the adhesion segment. TEM micrographs indicate the location of these vesicles in pockets of the plasma membrane. When part of the protein machinery involved in the fission of buds is knocked out, buds connected to the plasma membrane appear. Additionally, the plasma membrane is depolymerized of the actin filament making a membrane mediated budding process relevant. Inspection of the membrane morphology reveals that the plasma membrane seems to be segmented into a free cap and an adhered segment, which is reassembled by the system we investigated. Strikingly buds appear only at the contact line. We therefore suspect that the budding process could be triggered due to segmentation and flow of membrane components between the two segments. Note that the free plasma membrane segment appears to be bigger than the volume filled by buds making it unlikely that

budding precedes the segmentation of the membrane. Consistent Zhao, Wu and Veatch<sup>85</sup> has shown partitioning of membrane components between specifically bound and unbound membrane segments in plasma membrane extracted vesicles (GPMVs) which are close to a critical point. The budding transition observed by us depends on the proximity to a critical point, indicating that cells might exploit this mechanism to tune their membrane composition to avoid unspecific budding but still allow for selective budding transitions.

### 4.4 Conclusion

The adhesion of multicomponent vesicles, that exhibit phase separation, show various interesting effects, which are potentially biological relevant. We observed that bilayers which within in the miscibility gap are robust in the membrane composition and hence robust against non-specific adhesive perturbations in the explored region of adhesion energies. Such a mechanism is plausible to support homeostasis of cells, as a cell cannot tolerate non-specific interactions to segment the membrane and lipid composition randomly. At the same time, lipid density fluctuations are necessary to establish local domains such as the immunological gap. We show that even if two membrane segments are of a lipid composition which does not favour budding, budding can occur at the contact line where lipids are mixed. Buds appear in the absence of protein machinery. We have proposed a simple mechanistic model, based on interleaflet coupling, for the observed transitions. Interleaflet coupling, and hence also the kinetic trapping, diverge as the critical point is approached. The plasma membrane is thought to be tuned close to a critical point making such a mechanism feasible. When leaflets are free to adjust their composition, buds appear due to the generation of spontaneous curvature. The bistability induced by adhesion allows for compositional or temperature-triggered budding transitions. Kinetic trapping of membrane composition provides also a generic explanation why asymmetric adhesion to phase separated membranes is often observed to influence the phase state only close to a critical point. It would be interesting to study the proposed mechanism in more detail.

## 5 Specific adhesion by CD47- SIRP $\alpha$ complexes

Cell adhesion molecules are vital for many biological processes and are a key player in cell signalling. While well-established methods are available to measure the binding affinity  $K_{a,3d} = [RL]/[R][L]$ , where  $[R]$ ,  $[L]$  and  $[RL]$  are bulk concentrations of unbound receptor, ligands and their complexes, the *in-sito* situation is complicated by the fact that these proteins are bound to a membrane. Recent theoretical and model-membrane studies predict strong modulation of the binding affinity, due to membrane fluctuations and cooperative binding effects, which can be captured by a two dimensional binding constant  $l \cdot K_{2d} = K_{3d}$ , where  $l$  is a characteristic length scale<sup>29</sup>. Fluorescence Recovery after Photobleaching (FRAP) and single molecule techniques have been employed to study two dimensional receptor-ligand binding in whole cell models<sup>43, 98, 99</sup>. While the obtained results are highly relevant to understand how low affinity complexes initiate signalling, accurate measurement in living cells suffer from the usual heterogeneity and active processes in biological systems. The binding affinity reported for TCR complexes was found to vary four orders of magnitude depending on the location of the membrane<sup>99</sup>. Adhesion complexes can be studied by reconstitution into biomimetic lipid bilayers<sup>22</sup>, however developing minimal models for native membrane proteins is challenging, because proteins need to be first purified, which often cleaves the membrane anchor, and then reconstituted into synthetic membranes. Hence, specific strategies are needed for each protein system.

We used a new method, which relies on the extraction of plasma membrane vesicles from whole cell models. Such vesicles are also called Giant Plasma Membrane Vesicles (GPMVs)<sup>46</sup>. GPMVs reconstitute a number of plasma membrane components but obtain a vesicle-like shape, reminiscent of pure lipid bilayers. Hence they reconstitute some of the compositional complexity of whole cells, but should be described by a few continuous parameters. We show that, GPMVs can be used to study the interaction of CD47 with its ligand, the signal regulatory protein SIRP $\alpha$ , which inhibits phagocytosis from macrophages<sup>100</sup>.

CD47 was recently identified as a therapeutic target as it is enriched in tumour tissue<sup>101</sup>. High CD47 concentration preclude engulfment of macrophages and *in-vivo* tumour elimination<sup>102</sup>, however the mechanism by which CD47 is enriched is not clear. Tumour tissues have a heterogeneous microenvironment where key physiological parameters diverge. Because biological molecules are usually optimised in their function, i.e. binding affinity, in normal physiological conditions, the microenvironment is an important component to understand molecular mechanisms. We found that even a slight change from pH 7.4 to a mildly acidic pH of 6, which is in the pH range of tumour tissue, determines the outcome of phagocytosis of opsonized cells by macrophages in an *in-vitro* assay (Figure 5-1). We therefore used CD47 reconstituted in GPMVs to study the effects of an acidic environment on  $K_{2d}$ . We have also characterized some

previously unknown parameters of GPMVs, such as bending rigidity and protein diffusion constant.

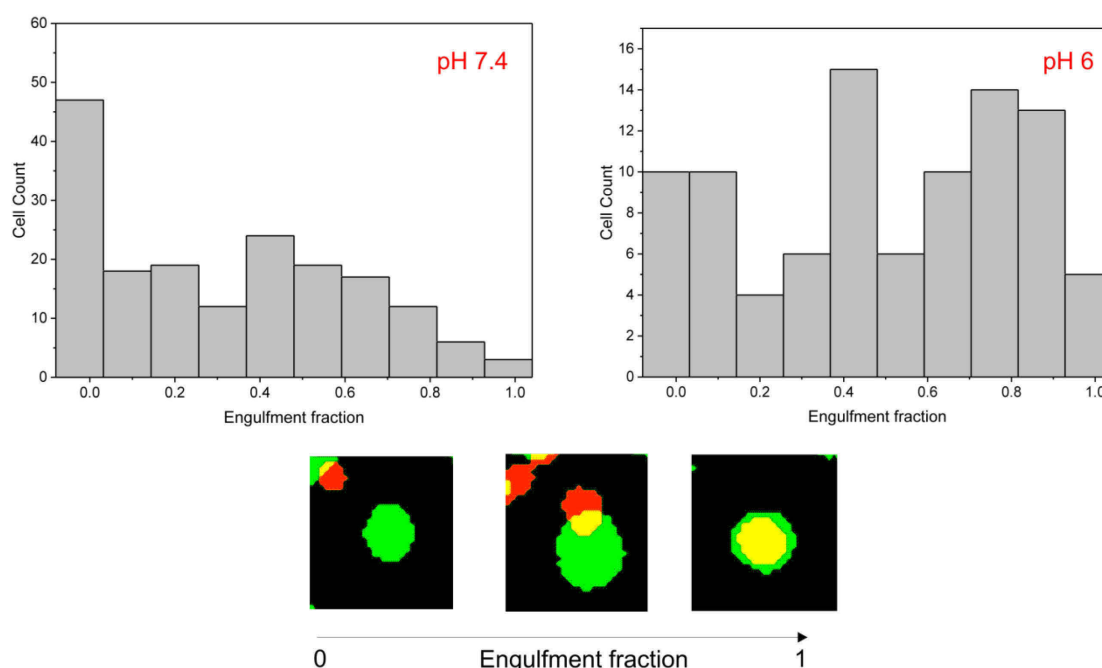


**Figure 5-1 - Enhanced uptake of opsonized A549 Cells under acidic conditions. Confocal images of the different experimental outcomes after image processing (Gaussian image filter and thresholding) Green: Macrophage, Red: A539 cell. Left: No eating, Middle: Partial engulfment Right: Complete engulfment. Top: Histogram of the different experimental outcomes in two conditions (pH6, pH7.4). For each macrophage the relative overlap between the green channel and the red channel was computed and normalized to the area of the macrophage.**

## 5.1 Methods

### 5.1.1 Phagocytosis assay

A549 Cells were opsonized with Human Red Blood Cell RBC Antibody (final concentration 250µg/5ml) for one hour at RT. Cells were washed and ladled with the dye PKH26 (Sigma-Aldrich) according to the manufacturers protocol. THP1 cells were left to adhere in standard cell 6-well culture dishes in RPMI/PMA media (initial concentration  $4 \cdot 10^5$  cells per well) for 48 hours. A549 cells were then added to the wells and incubated at either pH 7.4 or pH 6. After 75 minutes wells were washed by trypsin and uneaten A549 cells were removed by trypsinization. THP-1 was labelled by incubation with CD411b APC Antibody (2ng/ml one hour at RT). Finally cells were fixed by incubation with 4% PFA. Imaging was performed by a 10x objective on Leica SP8 system as described below. Images were processed by a Gaussian image filter, edges of cells were detected (ImageJ v1.50b), images thresholded to obtain binary images of cells. Overlap of the different channels was then calculated per cell.

### 5.1.2 Generation of HEK-CD47-GFP Cell Line, Cell culture and GPMV isolation

HEK 293T cells were transduced with a lentivector encoding CD47-GFP and puromycin resistance transgenes. Lentiviral transduction was carried out over 72hrs with a MOI of 5 and followed by puromycin selection (3µg/µl from gibco by life technologies) for 3 weeks. (Cells were transfected and supplied by Cory Alvey, UPenn). Cells were then cultured under standard condition in DMEM Media (w/o Phenol Red), 10% FBS and 1% Penicillin-Streptomycin and split every 2-3 days. Before experiments, cells were plated under identical conditions and cultured for 3 days until T25 culture wells were 90% confluent. In some cases, cells were labelled with the membrane dye DiIC18 by washing with 1ml PBS and subsequent incubation with 5 µL 0.5 mg/ml DiIC18 in ethanol for 10 minutes at 4°C. Unbound dye was washed away with PBS. GPMVs were isolated according to the protocol of by Sezgin et al<sup>46</sup>. HEK cells were incubated with 2mM DTT, 25mM PFA at 37°C for 1 hour. For experiments at varying pH, the GPMV buffer was adjusted to the desired pH at the day of the experiment.

### 5.1.3 Purification and absorption of SIRPα on glass slides

The soluble extracellular domain of SIRPα was purified as previously described<sup>103</sup>. The resulting protein is tagged by GST and we will refer to the resulting SIRPαEx-GST as to “SIRPα” in the following. SIRPα was then incubated on cleaned glass slides (2x rising with ethanol and ultra-pure water or five minutes exposure to oxygen plasma yielded the same results) for one hour in PBS at RT, concentration 34nM. Unbound SIRPα was washed away and uncovered glass surface was blocked by incubation with 1% BSA, 0.05% Tween-20 for one hour at RT. The coated glass slides were then washed in GPMV buffer at the desired pH and immediately covered with GPMV suspension.

### 5.1.4 Antibody labelling of GPMV, RBC and SIRPα

CD47 on GPMVs was labelled by incubation of B6H12 Alexa Fluor 647 Mouse Anti-Human Antibody (BD Biosciences) for one hour at RT according to the protocol of the manufacturer. RBCs were isolated from a healthy male individual, washed in PBS and incubated in the same conditions as the GPMVs with the antibody. In some experiments, SIRPα was labelled on the glass surface by incubating with rabbit anti-GST Alexa 488 (Invitrogen) at 20µg/ml for one hour at RT and subsequent washing.

### 5.1.5 Confocal imaging, FRAP experiments and Image analysis

Confocal images were obtained on a Leica SP8 system, dyes were excited using the 488 and 638 laser lines and fluorescence was collected (495-600nm and 650-750nm). To avoid cross-talk between the channels, two-colour images were always obtained sequentially. FRAP experiments were performed on the same system. A circle of 1µm in diameter was bleached using the 488 laser and recovery was observed under normal imaging conditions for 60 frames and 0.2 frames per second. The data was corrected for bleaching by dividing the intensity obtained in the bleached spot by the intensity of



an unbleached area about 20 $\mu$ m away from the bleaching spot. The background level was subtracted as estimated from the first frame after bleaching. The data was subsequently fitted to the model described in Chapter 2.4 using the routine `invlap`<sup>104</sup> and `nlinfit` (MATLAB 2014a). To estimate the diffusion of free CD47, GPMVs were bleached on the upper pole and recovery curves were fitted using the model for free diffusion (Chapter 2.4). Fluorescent intensities were quantified either by a line profile on the vesicle equator (to obtain the correlation between GFP and AntiCD47) or a line profile on the (x,z) contour in the case of adhering vesicles, both lines were 1 $\mu$ m wide. (ImageJ version 1.47). We used the peak of the resulting intensity distribution as an indicator of dye concentration in the membrane. To compare the CD47 density between RBC and GPMVs we compared the maximum projection in the centre of a labelled RBC to the fluorescent intensity at the pole of GPMVs.

### **5.1.6 K<sub>3d</sub> assay using Red Blood Cells (RBCs)**

Fresh RBCs were washed and incubated with SIRP $\alpha$  (final concentration 34nM) for one hour at RT in PBS adjusted to pH 7.4 or pH 6. GST was labelled as described before. RBCs were pelleted and unbound protein was washed away. RBCs were then imaged and the mean fluorescence in the centre of a RBC was measured in a circle of 6 $\mu$ m diameter.

### **5.1.7 LUV preparation and Zeta potential measurements**

Charged PEGgylated SUVs were obtained by mixing 79/19/2 mol% DOPC, DOPS and PEG2000-PE (Avanti Polar Lipids) solvated in chloroform, additionally 0.5mol% of the fluorescent label NBD-PG was included. The chloroform was evaporated under low pressure at 60°C for one hour. The dried film was rehydrated in PBS Buffer to a final concentration of 2mg/ml, subsequent 10 freeze-thaw cycles and extruding through a 100nm filter (Avestin Inc., Ottawa, Canada) yielded LUV of an average size of 110nm $\pm$ 5nm, as measured by light scattering. Zeta potential was measured for PEGgylated SUVs and GPMVs by electrophoresis (ZetaSizer Nano ZS, Malvern). To adjust the pH samples were titrated by addition of concentrated HCl into the 800 $\mu$ l volume of the measurement cell.

## 5.2 Results and discussion

### 5.2.1 Cd47 is reconstituted in GPMVs

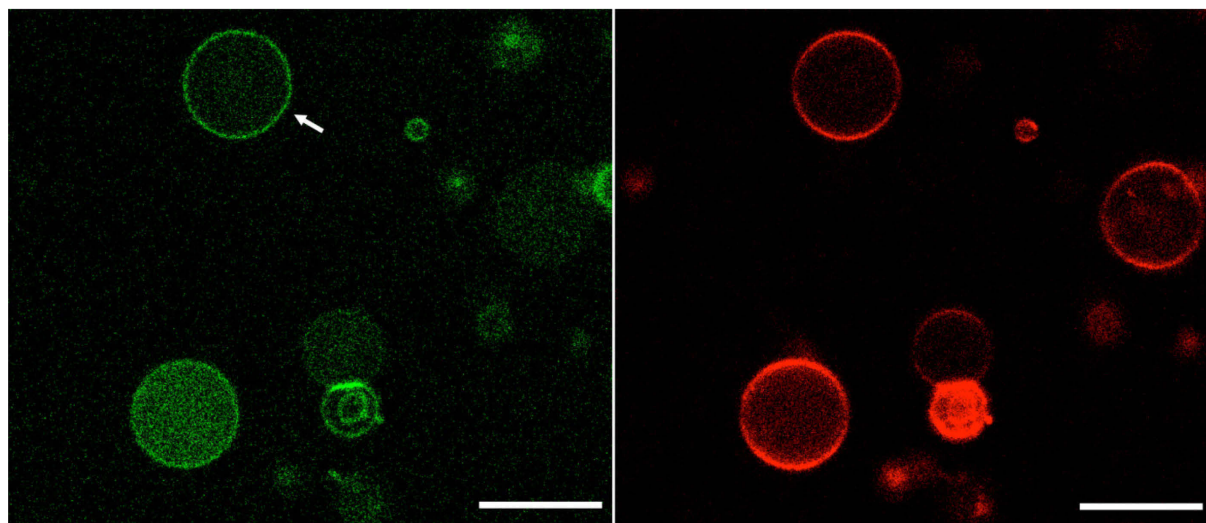
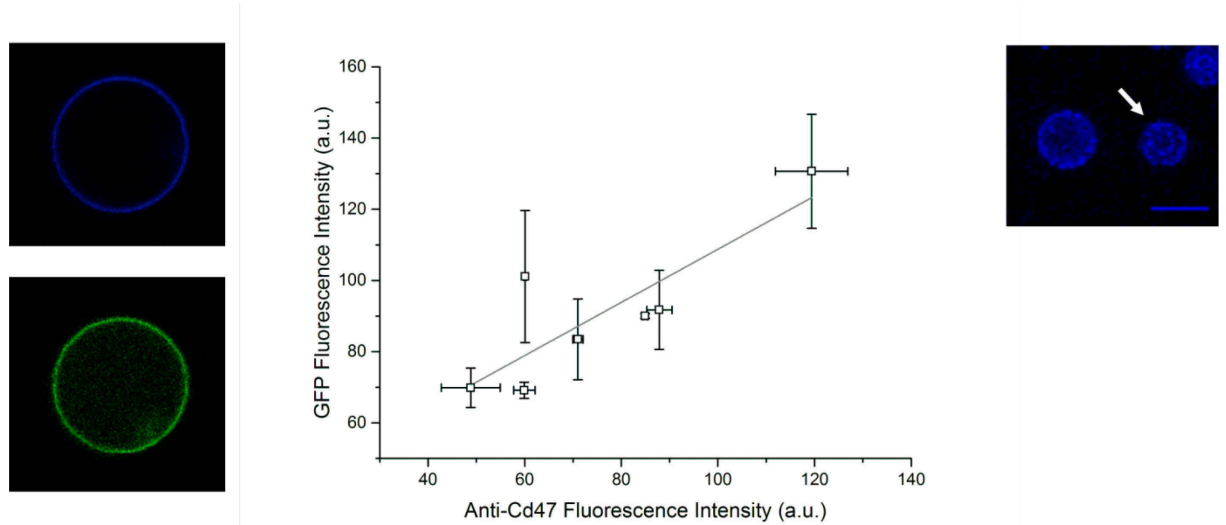


Figure 5-2 - Confocal image of isolated GPMVs. Left: GFP labelled CD47 Right: Membrane marker DiIc18. The arrow indicates a typical vesicle selected for experiments (no internal fluorescence). Scale bar 10 $\mu$ m

It is known that GPMVs reconstitute a substantial number of membrane proteins<sup>47</sup>. Indeed, when GPMVs are isolated from HEK cells which express CD47-GFP, GPMVs appear fluorescent in the green channel (Figure 5-2). Some vesicles are filled by green fluorescence. While it is not clear what the exact nature of this effect is, it is thought that this is an artefact of the vesicle isolation. The following experiments are conducted on vesicles that appear dark on the inside, indicating that CD47 is bound to the membrane only. To understand if CD47 is properly orientated and if the GFP signal corresponds to the actual CD47 concentration, GPMVs were labelled by fluorescent anti-CD47. By confocal microscopy both fluorescent signals were quantified and results are shown in Figure 5-3. Good correlation is obtained, indicating that the GFP signal is indeed a good indicator of the CD47 concentration in GPMVs. Note that the distribution of different CD47 levels within one batch of GPMVs is presumably due to the natural heterogeneity of CD47 levels in cells<sup>105</sup>. This allowed us to investigate a range of CD47 concentrations. To obtain the real concentration from the fluorescent intensities, RBCs which naturally express CD47 (about 250 molecules/ $\mu$ m<sup>2</sup> <sup>106</sup>) were labelled by the same anti-CD47 and incubated together with the GPMVs. This method enables us to estimate the absolute number of CD47 expressed on GPMVs by comparison of the fluorescent intensity. We found that, GPMVs exhibit an average concentration of about 200 CD47 molecules/ $\mu$ m<sup>2</sup>, corresponding to a fluorescent intensity of 40 a.u. at the pole of a GPMV (Figure 5-6 and Figure 5-8). As mentioned before, a number of membrane and transmembrane proteins are reconstituted in the GPMVs and we did not optimize the standard GPMV isolation protocol in any way to reconstitute membrane bound CD47. Hence, we can assume that the GPMV

membrane reconstitutes a lipid bilayer which is rather densely covered by different proteins. In the context of CD47 binding, it is instructive to think of stickers (CD47) and repeller molecules (all the other membrane bound components).



**Figure 5-3** - Upper Left: Anti-CD47 Immunostaining. Lower Left: GFP-CD47 Channel. Middle: Correlation between Anti-CD47 and GFP signal indicate functional reconstitution of CD47. Each data point is an individual vesicle. Upper right: Incubation of red blood cells together with a GPMV to estimate the CD47 concentration in real units. Arrow indicates a RBC. Scale bar 10  $\mu\text{m}$

### 5.2.2 Adhesion of CD47 expressing GPMVs to SIRP $\alpha$

After we have established that CD47 is inserted into GPMVs and is properly oriented for binding, we questioned whether it can also bind its receptor SIRP $\alpha$ . We immobilized the extracellular domain of SIRP $\alpha$  on glass slides by physisorption. To check if SIRP $\alpha$  is absorbed in a homogenous layer, we incubated the glass slides with fluorescently labelled anti-GST. On the typical length scale of GPMVs, SIRP $\alpha$  appeared homogenous, with no visible domains or defects (Figure 5-4 left). The density of absorbed SIRP $\alpha$  was estimated by comparing the fluorescent intensity of anti-GST fluorescence to the GFP signal of the vesicles, we corrected for the different dyes by linear correction in exciting coefficient and quantum yield. We find that SIRP $\alpha$  concentration on the glass surface is 20x times higher than the GFP signal. This indicates a SIRP $\alpha$  density of  $[R_0] \approx 4000$  molecules/ $\mu\text{m}^2$ , which is consistent with E-selectin densities obtained by physisorption under similar conditions<sup>24</sup>. This is below the density of a SIRP $\alpha$  monolayer at maximal packing and we can expect that BSA, which is used for blocking uncovered glass surface, fills the gaps between individual SIRP $\alpha$  molecules.

Individual GPMVs were left to sediment onto the coated cover glass by gravitational forces and imaged by confocal microscopy. Clearly SIRP $\alpha$  and CD47 bind as it can be seen by the vesicle shape (Figure 5-4 right). When the coverglass is only coated by BSA no adhesion is observed.

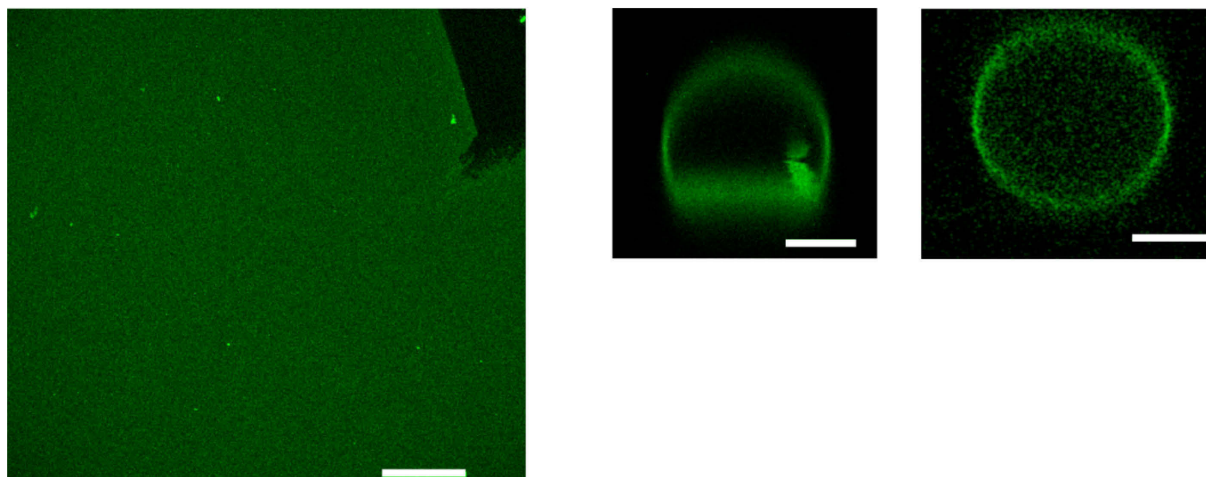


**Figure 5-4** - Left: Anti-GST staining of SIRP $\alpha$  absorbed on a glass slide. The black region is a scratch with a pipette tip to estimate the background level. Scale bar 60 $\mu$ m Right: Confocal vertical cross section (x,z) of an adhering vesicle on a SIRP $\alpha$  coated slide (left) and a nonadhering vesicle sitting on a BSA coated glass slide (right). Scale bars 5 $\mu$ m

We observed that the initial distribution of CD47 in the adhering membrane segment is not homogenous (Figure 5-5) exhibiting a ring of higher concentration in the vicinity of the rim of the adhesion zone, and equilibrates over duration of an hour to reach homogeneous distribution over the whole adhesion disc. This transient ring formation is qualitatively consistent with simulation results for a comparable system where adhesion competes to longer repeller molecules<sup>25</sup>. Because the SIRP $\alpha$ -cd47 complex is rather short (17 nm<sup>107</sup>) we can assume that repeller molecules that are “longer”, for example Integrin and glycoproteins, are excluded from the adhering membrane segment. We did not further study this phenomenon but focused on equilibrated vesicles (>1h after adhesion).

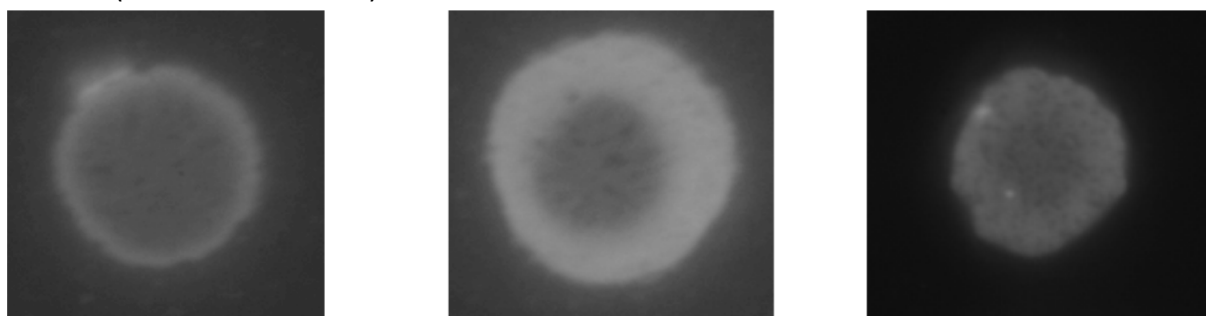


**Figure 5-5** - Typical equilibration of the adhering membrane segment observed by epifluorescence (time increases from left to right). In the first minutes a bright ring appears in the rim of the adhering segment (middle). Over the time course of an hour the distribution becomes homogenous (right). Different vesicles are shown at each time point, the adhering segment is about 15 $\mu$ m in diameter

Due to adhesion, GPMVs exhibit two membrane segments: The bound membrane in the vicinity of the SIRP $\alpha$  coated glass slide and the unbound cap. As reasoned above, these two segments should have rather different compositions. This can be quantified by measurement of fluorescent intensity of CD47-GFP in adhering and free membrane segments (Figure 5-6). As expected, CD47 is found to be enriched in the adhering

segment. In theory, one can extract the two dimensional binding constant from this data:

$$K_{2d,int} = \frac{[RL]}{[R][L]} \approx \frac{A(I_{adh} - I_{cap})}{AI_{cap}[R_0]}$$

Where brackets indicate surface concentrations of bound and free receptor and ligands, A is the proportionality factor between fluorescent intensity and real concentration and cancels out. We assumed that the concentration of free SIRPα stays virtually constant and is in excess ( $[R] \approx [R_0] \gg [RL]$ ). In practice, it proved to be difficult to obtain precise values of  $K_{2d,int}$ , presumably because of the rather low concentration of CD47 and hence low GFP intensity. This leads to big errors in the intensity quantification. We therefore used FRAP to extract  $K_{2d}$  which has been previously used to study receptor-binding kinetics in whole cell models<sup>43, 98</sup>. Here  $K_{2d}$  is obtained by the dynamics of fluorescence recovery which depends on the binding and unbinding rates.

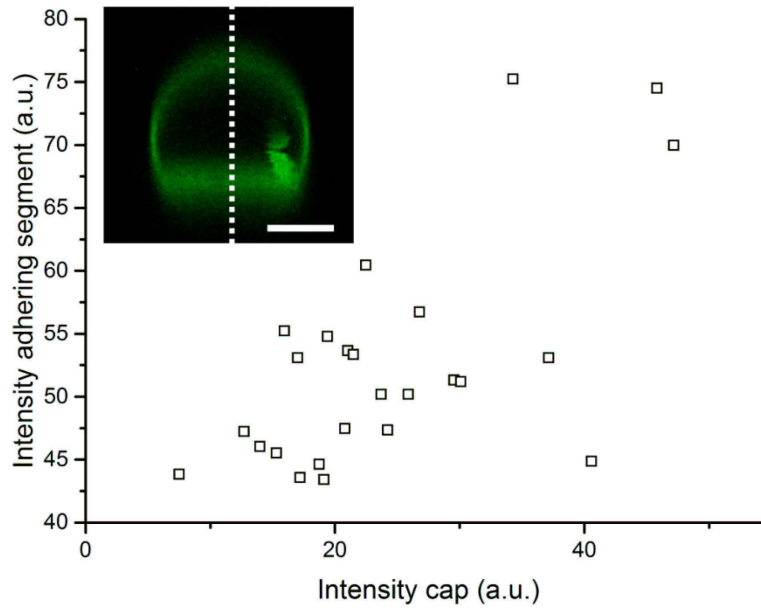
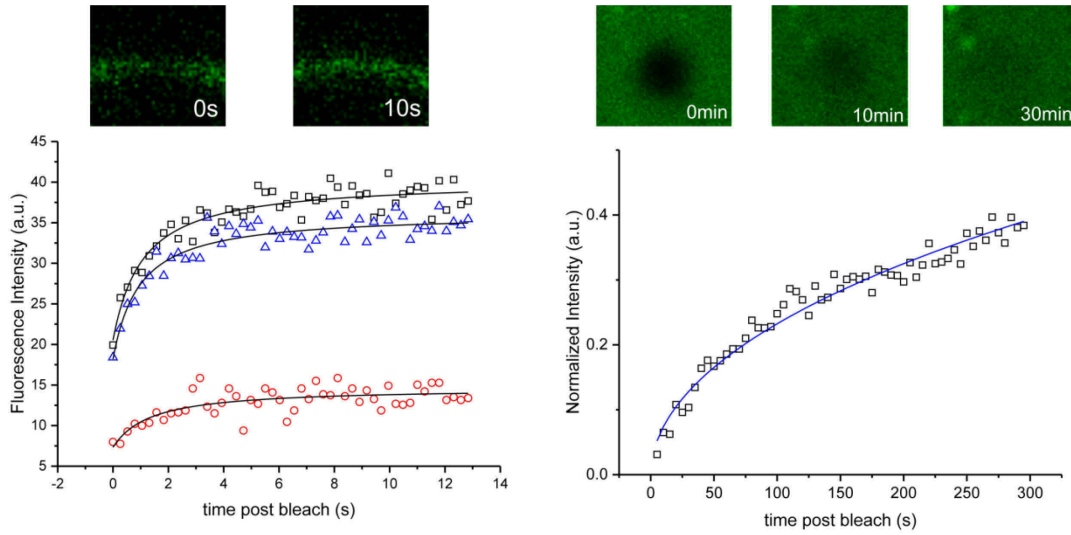


Figure 5-6 - Quantification of bound and unbound CD47 by fluorescence intensity. Left: Individual data point from different vesicles under the same conditions. The line indicates a line profile which is used to extract the fluorescence intensity. Scale bar 5μm

### 5.2.3 FRAP indicates cooperative enrichment of CD47 in the adhering membrane segment

FRAP experiment on the unbound and bound membrane segments show two different timescales. In the unbound segment, CD47 fluorescence recovers on the timescale of seconds and we find a diffusion constant of  $D_{cd47} \approx 0.12 \pm 0.02 \mu m^2/s$ . When CD47 is within the adhesion zone, recovery is about two orders of magnitude slower. Because

$K_{3d}$  of SIRP $\alpha$ -cd47 is about  $8\mu\text{M}$  with  $k_{\text{off}}$  in the order of  $\text{s}^{-1} \cdot 10^8$ , we can expect that bound CD47 stochastically unbinds, diffuses in the adhering membrane segment and eventually rebinds to vacant SIRP $\alpha$  molecules. The underlying reaction-diffusion model (see Chapter 2.4) yields a satisfactory fit to our data (Figure 5-7). Because we can only roughly estimate the SIRP $\alpha$  concentration  $[R]$  we present the results of the fit normalized by  $[R]$ . From fitting our data, we obtain estimates for  $[R]k_{\text{on}}$ ,  $k_{\text{off}}$  and  $[R]K_{2d,\text{FRAP}}$ . Note that within the bleached spot there are only about 150 CD47 molecules; hence in the first seconds of recovery only about a dozen GFP molecules contribute to the signal. The data is inherently noisy and we found that the recovered values for  $[R]k_{\text{on}}$  and  $k_{\text{off}}$  depended significantly on the starting values of the fitting routine. However, the ratio of these rates is robust, in other words  $[R]K_{2d,\text{FRAP}}$  is obtained with higher degree of confidence.



**Figure 5-7 – FRAP recovery intensity time course and confocal images of a typical recovery. Left: Free membrane segment with cross section images above, the three curves represent different vesicles. Right: Bound membrane segment with top view images above. Fit for  $[R]k_{\text{on}} \approx 4.32 \cdot 10^4 \text{ s}^{-1}$ ,  $k_{\text{off}} \approx 4.9 \text{ s}^{-1}$ . Bleached spot is  $1\mu\text{m}$  in diameter**

Figure 5-8 (left) shows the extracted  $[R]K_{2d,\text{FRAP}}$  values for individual vesicles of different CD47-SIRP $\alpha$  concentration. A clear correlation between bound complexes and  $[R]K_{2d}$  can be seen. If we assume  $[R] \approx \text{const}$ , which is reasonable for our system with  $[R_0] \approx 4000 \text{ SIRP}\alpha/\mu\text{m}^2$ , this result is a clear indication that binding is cooperative. In the case of non-cooperative binding, no correlation would be seen. This is in line with a general theory of membrane bound receptor ligand pairs which predicts cooperative binding effects by the suppression of membrane fluctuations in the vicinity of bound complexes<sup>26, 29, 109</sup>.

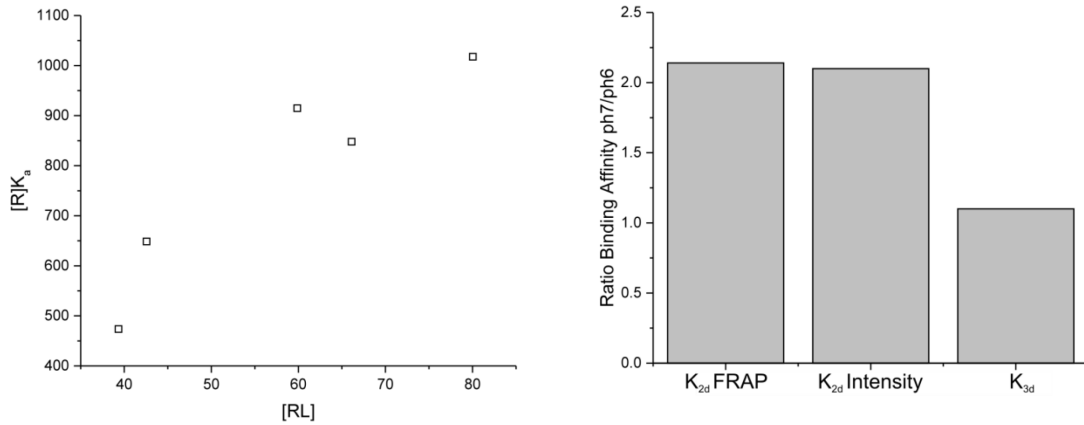


**Figure 5-8** - Left:  $[R] K_{2d,FRAP}$  obtained by FRAP, each datapoint represents a single vesicle  $[RL]$  is obtained by subtracting the fluorescent intensity in the free segment from the intensity in the adhered segment. Right: Ratio of  $K_{2d}$  and  $K_{3d}$  measured at pH 7.4 to the respective values measured at pH 6.  $K_{2d}$  values were obtained either by intensity measurements or FRAP.  $K_{3d}$  is obtained by binding soluble SIRP $\alpha$  to RBCs.

#### 5.2.4 Acidic, tumour like, conditions lead to decrease of $K_{2d}$

We isolated GPMVs at pH 7.4 and pH 6. We again incubated GPMVs on SIRP $\alpha$  glass slides and measured  $K_{2d}$  values in these two conditions. We find that  $K_{2d}$  measured by fluorescent intensities and FRAP recovery consistently yields a reduction of  $K_{2d}$  by a factor of two (Figure 5-8 right). This result leads us to ask, if reduction of  $K_{2d}$  is due to the intrinsic binding affinity of the two proteins ( $K_{3d}$ ) or a true effect of the two dimensional confinement (reflected in  $K_{2d}$ ). To the best of our knowledge there are no studies on the pH effect on  $K_{3d}$  for SIRP $\alpha$ -CD47. Therefore, we measured  $K_{3d}$  in these two pH conditions by binding soluble SIRP $\alpha$  to RBCs. No significant difference in bound SIRP $\alpha$  was measured. This leads us to believe, that the reduction in  $K_{2d}$  is at least in part due to the two dimensional confinement.

### 5.3 Conclusion

Membrane proteins reconstituted in GPMVs are suitable for assessing adhesion-related phenomena in cells. Even moderate changes in pH, compatible to those found in tumour tissue, were found to modulate  $K_{2d}$  but not the commonly measured  $K_{3d}$ . One can speculate that these results provide a possible mechanism for the enrichment of CD47 in tumour tissue. The reduced binding affinity could lead to preferential clearance of low-expressing CD47 cells in the tumours, leading to an increase in mean CD47 concentration. In the broader picture, this work highlights the importance of non-specific interactions on the binding of receptor-ligand pairs. While cell signalling is due to highly specific receptor-ligand interactions, non-specific interactions are always at play. We have shown that pH can modulate the average membrane separation which has a strong effect on binding affinity of membrane bound complexes.



## 6 Summary and Outlook

In this work three different models for membranes partitioned into two segments were studied. In the first part of the thesis a novel system to induce adhesion to planar substrates, in a reversible and controlled fashion, was described. Two features should be emphasized. We have seen, that only lipids of the outer leaflet “feel” the adhesive surface when membranes are made of lipids that are perfectly miscible. As lipids have a preference to one of the two membrane segments, this will lead invariably to the generation of asymmetry and spontaneous curvature in the membrane. In the next chapter we have seen, that adhesion induced compositional and morphological changes, depend on the phase state of the membrane. Most interestingly we have described a budding transition in the contact line between two membrane segments and discussed a possible mechanism due to dynamic lipid flows. Again this budding transition depends on the membrane phase state, opening the possibly to regulate budding transitions by active processes. In the last chapter we have shown that plasma derived vesicles can be used to study binding of proteins. This is advantageous, as proteins under interest are naturally reconstituted into GPMVs. The last chapter also links non-specific membrane interactions, studied in Chapters 3 and 4, to the adhesion due to specific adhesion complexes.



## 7 References

1. Alberts, B., *Molecular biology of the cell*. Garland Science: New York, 1994.
2. Koningsveld, R.; Stockmayer, W. H.; Nies, E., *Polymer phase diagrams : a textbook*. Oxford University Press: Oxford; New York, 2001.
3. Nagle, J. F., Theory of the main lipid bilayer phase transition. *Annual Review of Physical Chemistry* **1980**, 31, (1), 157-196.
4. Lipowsky, R.; Sackmann, E., Structure and dynamics of membranes. In Elsevier Science: Amsterdam; New York, 1995; Vol. 1A.
5. Veatch, S. L.; Keller, S. L., Seeing spots: Complex phase behavior in simple membranes. *Biochimica et Biophysica Acta - Molecular Cell Research* **2005**, 1746, (3), 172-185.
6. Feigenson, G. W., Phase diagrams and lipid domains in multicomponent lipid bilayer mixtures. *Biochimica et Biophysica Acta (BBA) - Biomembranes* **2009**, 1788, (1), 47-52.
7. Bezlyepkina, N.; Gracià, R. S.; Shchelokovskyy, P.; Lipowsky, R.; Dimova, R., Phase Diagram and Tie-Line Determination for the Ternary Mixture DOPC/eSM/Cholesterol. *Biophys J* **2013**, 104, (7), 1456-1464.
8. Patariaia, S.; Liu, Y.; Lipowsky, R.; Dimova, R., Effect of cytochrome c on the phase behavior of charged multicomponent lipid membranes. *Biochimica et Biophysica Acta (BBA) - Biomembranes* **2014**, 1838, (8), 2036-2045.
9. Vequi-Suplicy, C. C.; Riske, K. A.; Knorr, R. L.; Dimova, R., Vesicles with charged domains. *Biochimica et Biophysica Acta (BBA) - Biomembranes* **2010**, 1798, (7), 1338-1347.
10. Gordon, V. D.; Deserno, M.; Andrew, C. M. J.; Egelhaaf, S. U.; Poon, W. C. K., Adhesion promotes phase separation in mixed-lipid membranes. *EPL (Europhysics Letters)* **2008**, 84, (4), 48003.
11. Dimova, R.; Said, A.; Natalya, B.; Vesselin, N.; Karin, A. R.; Reinhard, L., A practical guide to giant vesicles. Probing the membrane nanoregime via optical microscopy. *Journal of Physics: Condensed Matter* **2006**, 18, (28), S1151.
12. Seifert, U.; Lipowsky, R., Morphology of vesicles. *Handbook of biological physics* **1995**, 1, 403-464.
13. Dimova, R., Recent developments in the field of bending rigidity measurements on membranes. *Advances in Colloid and Interface Science* **2014**, 208, 225-234.
14. Lipowsky, R.; Seifert, U., Adhesion of vesicles and membranes. *Molecular crystals and liquid crystals* **1991**, 202, (1), 17-25.
15. Weikl, T. R.; Lipowsky, R., Membrane adhesion and domain formation. *Advances in Planar Lipid Bilayers and Liposomes* **2006**, 5, 63-127.
16. Singer, S. J.; Nicolson, G. L., The Fluid Mosaic Model of the Structure of Cell Membranes. *Science* **1972**, 175, (4023), 720-731.
17. Grakoui, A.; Bromley, S. K.; Sumen, C.; Davis, M. M.; Shaw, A. S.; Allen, P. M.; Dustin, M. L., The Immunological Synapse: A Molecular Machine Controlling T Cell Activation. *Science* **1999**, 285, (5425), 221-227.
18. Sheetz, M. P., Cellular plasma membrane domains. *Molecular membrane biology* **1995**, 12, (1), 89-91.

19. Eggeling, C.; Ringemann, C.; Medda, R.; Schwarzmann, G.; Sandhoff, K.; Polyakova, S.; Belov, V. N.; Hein, B.; von Middendorff, C.; Schonle, A.; Hell, S. W., Direct observation of the nanoscale dynamics of membrane lipids in a living cell. *Nature* **2009**, 457, (7233), 1159-U121.
20. Maxfield, F. R.; Tabas, I., Role of cholesterol and lipid organization in disease. *Nature* **2005**, 438, (7068), 612-621.
21. Knorr, R. L.; Nakatogawa, H.; Ohsumi, Y.; Lipowsky, R.; Baumgart, T.; Dimova, R., Membrane Morphology Is Actively Transformed by Covalent Binding of the Protein Atg8 to PE-Lipids. *Plos One* **2014**, 9, (12), e115357.
22. Sackmann, E.; Smith, A.-S., Physics of cell adhesion: some lessons from cell-mimetic systems. *Soft Matter* **2014**, 10, (11), 1644-1659.
23. Sackmann, E.; Bruinsma, R. F., Cell adhesion as wetting transition? *ChemPhysChem* **2002**, 3, (3), 262-269.
24. Lorz, B. G.; Smith, A.-S.; Gege, C.; Sackmann, E., Adhesion of Giant Vesicles Mediated by Weak Binding of Sialyl-LewisX to E-Selectin in the Presence of Repelling Poly(ethylene glycol) Molecules. *Langmuir* **2007**, 23, (24), 12293-12300.
25. Weikl, T. R.; Lipowsky, R., Pattern Formation during T-Cell Adhesion. *Biophys J* **2004**, 87, (6), 3665-3678.
26. Krobath, H.; Różycki, B.; Lipowsky, R.; Weikl, T. R., Binding cooperativity of membrane adhesion receptors. *Soft Matter* **2009**, 5, (17), 3354-3361.
27. Weikl, T. R.; Asfaw, M.; Krobath, H.; Różycki, B.; Lipowsky, R., Adhesion of membranes via receptor–ligand complexes: Domain formation, binding cooperativity, and active processes. *Soft Matter* **2009**, 5, (17), 3213-3224.
28. Lipowsky, R.; Rouhiparkouhi, T.; Discher, D. E.; Weikl, T. R., Domain formation in cholesterol-phospholipid membranes exposed to adhesive surfaces or environments. *Soft Matter* **2013**, 9, (35), 8438-8453.
29. Hu, J.; Lipowsky, R.; Weikl, T. R., Binding constants of membrane-anchored receptors and ligands depend strongly on the nanoscale roughness of membranes. *Proceedings of the National Academy of Sciences* **2013**, 110, (38), 15283-15288.
30. Boulbitch, A.; Guttenberg, Z.; Sackmann, E., Kinetics of membrane adhesion mediated by ligand–receptor interaction studied with a biomimetic system. *Biophys J* **2001**, 81, (5), 2743-2751.
31. Nardi, J.; Feder, T.; Bruinsma, R.; Sackmann, E., Electrostatic adhesion between fluid membranes: phase separation and blistering. *EPL (Europhysics Letters)* **1997**, 37, (5), 371.
32. Almeida, P. F. F.; Pokorny, A.; Hinderliter, A., Thermodynamics of membrane domains. *Biochimica et Biophysica Acta (BBA) - Biomembranes* **2005**, 1720, (1–2), 1-13.
33. Pike, L. J., Rafts defined: a report on the Keystone symposium on lipid rafts and cell function. *Journal of Lipid Research* **2006**, 47, (7), 1597-1598.
34. McIntosh, T. J., *Lipid Rafts*. Humana Press Inc.: New Jersey, 2007; Vol. 398.
35. Cottingham, K., Do You Believe in Lipid Rafts? *Analytical Chemistry* **2004**, 76, (21), 403 A-406 A.
36. Sezgin, E.; Levental, I.; Grzybek, M.; Schwarzmann, G.; Mueller, V.; Honigsmann, A.; Belov, V. N.; Eggeling, C.; Coskun, U.; Simons, K.; Schwille, P., Partitioning, diffusion,

- and ligand binding of raft lipid analogs in model and cellular plasma membranes. *Bba-Biomembranes* **2012**, 1818, (7), 1777-1784.
37. Diaz, A. J.; Albertorio, F.; Daniel, S.; Cremer, P. S., Double cushions preserve transmembrane protein mobility in supported bilayer systems. *Langmuir* **2008**, 24, (13), 6820-6826.
  38. Steltenkamp, S.; Müller, M. M.; Deserno, M.; Hennessthal, C.; Steinem, C.; Janshoff, A., Mechanical properties of pore-spanning lipid bilayers probed by atomic force microscopy. *Biophys J* **2006**, 91, (1), 217-226.
  39. Pawley, J.; Masters, B. R., Handbook of biological confocal microscopy. *Optical Engineering* **1996**, 35, (9), 2765-2766.
  40. Gullapalli, R. R.; Demirel, M. C.; Butler, P. J., Molecular dynamics simulations of DiI-C 18 (3) in a DPPC lipid bilayer. *Physical Chemistry Chemical Physics* **2008**, 10, (24), 3548-3560.
  41. Gell, C.; Berndt, M.; Enderlein, J.; Diez, S., TIRF microscopy evanescent field calibration using tilted fluorescent microtubules. *Journal of microscopy* **2009**, 234, (1), 38-46.
  42. Soumpasis, D. M., Theoretical analysis of fluorescence photobleaching recovery experiments. *Biophys J* **1983**, 41, (1), 95-97.
  43. Sprague, B. L.; Pego, R. L.; Stavreva, D. A.; McNally, J. G., Analysis of Binding Reactions by Fluorescence Recovery after Photobleaching. *Biophys J* **2004**, 86, (6), 3473-3495.
  44. Luisi, P. L.; Walde, P. In *Giant vesicles*, Chichester; New York, 2000, Wiley: Chichester; New York.
  45. Scott, R. E., Plasma membrane vesiculation: A new technique for isolation of plasma membranes. *Science* **1976**, 194, (4266), 743-745.
  46. Sezgin, E.; Kaiser, H.-J.; Baumgart, T.; Schwille, P.; Simons, K.; Levental, I., Elucidating membrane structure and protein behavior using giant plasma membrane vesicles. *Nat. Protocols* **2012**, 7, (6), 1042-1051.
  47. Bauer, B.; Davidson, M.; Orwar, O., Proteomic Analysis of Plasma Membrane Vesicles. *Angewandte Chemie International Edition* **2009**, 48, (9), 1656-1659.
  48. Seeliger, J.; Erwin, N.; Rosin, C.; Kahse, M.; Weise, K.; Winter, R., Exploring the structure and phase behavior of plasma membrane vesicles under extreme environmental conditions. *Physical Chemistry Chemical Physics* **2015**, 17, (11), 7507-7513.
  49. Richter, R. P.; Bérat, R.; Brisson, A. R., Formation of solid-supported lipid bilayers: an integrated view. *Langmuir* **2006**, 22, (8), 3497-3505.
  50. Walde, P.; Cosentino, K.; Engel, H.; Stano, P., Giant vesicles: preparations and applications. *ChemBioChem* **2010**, 11, (7), 848-865.
  51. Salipante, P. F.; Knorr, R. L.; Dimova, R.; Vlahovska, P. M., Electrodeformation method for measuring the capacitance of bilayer membranes. *Soft Matter* **2012**, 8, (14), 3810-3816.
  52. Fenz, S. F.; Sengupta, K., Giant vesicles as cell models. *Integrative Biology* **2012**, 4, (9), 982-995.
  53. Seifert, U.; Lipowsky, R., Adhesion of vesicles. *Phys Rev A* **1990**, 42, (8), 4768-4771.

54. Rädler, J.; Sackmann, E., Vesicle-Substrate Interaction Studied by Reflection Interference Contrast Microscopy. In *The Structure and Conformation of Amphiphilic Membranes*, Lipowsky, R.; Richter, D.; Kremer, K., Eds. Springer Berlin Heidelberg: 1992; Vol. 66, pp 158-161.
55. Fang, N.; Chan, V.; Wan, K.-T., The effect of electrostatics on the contact mechanics of adherent phospholipid vesicles. *Colloids and Surfaces B: Biointerfaces* **2003**, 27, (1), 83-94.
56. Reinhard, L.; Martin, B.; Rumiana, D.; Thomas, F.; Jan, K.; Xinzhaio, Z., Droplets, bubbles, and vesicles at chemically structured surfaces. *Journal of Physics: Condensed Matter* **2005**, 17, (9), S537.
57. Gruhn, T.; Franke, T.; Dimova, R.; Lipowsky, R., Novel Method for Measuring the Adhesion Energy of Vesicles. *Langmuir* **2007**, 23, (10), 5423-5429.
58. Limozin, L.; Sengupta, K., Quantitative Reflection Interference Contrast Microscopy (RICM) in Soft Matter and Cell Adhesion. *ChemPhysChem* **2009**, 10, (16), 2752-2768.
59. Bernard, A.-L.; Guedeau-Boudeville, M.-A.; Jullien, L.; Di Meglio, J.-M., Imaging vesicle adhesion by evanescent wave-induced fluorescence. *EPL (Europhysics Letters)* **1999**, 46, (1), 101.
60. Bernard, A. L.; Guedeau-Boudeville, M. A.; Jullien, L.; di Meglio, J. M., Strong Adhesion of Giant Vesicles on Surfaces: Dynamics and Permeability. *Langmuir* **2000**, 16, (17), 6809-6820.
61. Schmidt, D.; Monzel, C.; Bihr, T.; Merkel, R.; Seifert, U.; Sengupta, K.; Smith, A.-S., Signature of a Nonharmonic Potential as Revealed from a Consistent Shape and Fluctuation Analysis of an Adherent Membrane. *Physical Review X* **2014**, 4, (2), 021023.
62. Nardi, J.; Bruinsma, R.; Sackmann, E., Adhesion-induced reorganization of charged fluid membranes. *Physical Review E* **1998**, 58, (5), 6340-6354.
63. Mugele, F.; Baret, J.-C., Electrowetting: from basics to applications. *Journal of Physics: Condensed Matter* **2005**, 17, (28), R705.
64. Mugele, F., Fundamental challenges in electrowetting: from equilibrium shapes to contact angle saturation and drop dynamics. *Soft Matter* **2009**, 5, (18), 3377-3384.
65. Angelova, M. I.; Dimitrov, D. S., Liposome electroformation. *Faraday Discussions of the Chemical Society* **1986**, 81, (0), 303-311.
66. Gracia, R. S.; Bezlyepkina, N.; Knorr, R. L.; Lipowsky, R.; Dimova, R., Effect of cholesterol on the rigidity of saturated and unsaturated membranes: fluctuation and electrodeformation analysis of giant vesicles. *Soft Matter* **2010**, 6, (7), 1472-1482.
67. McIntyre, J. C.; Sleight, R. G., Fluorescence assay for phospholipid membrane asymmetry. *Biochemistry-Us* **1991**, 30, (51), 11819-11827.
68. Soumpasis, D. M., Theoretical analysis of fluorescence photobleaching recovery experiments. *Biophys J* **1983**, 41, (1), 95-97.
69. Tordeux, C.; Fournier, J. B.; Galatola, P., Analytical characterization of adhering vesicles. *Physical Review E* **2002**, 65, (4), 041912.
70. Lipowsky, R., Coupling of bending and stretching deformations in vesicle membranes. *Advances in Colloid and Interface Science* **2014**, 208, (0), 14-24.
71. Harries, D.; May, S.; Gelbart, W. M.; Ben-Shaul, A., Structure, stability, and thermodynamics of lamellar DNA-lipid complexes. *Biophys J* **1998**, 75, (1), 159-173.

72. May, S.; Harries, D.; Ben-Shaul, A., Lipid demixing and protein-protein interactions in the adsorption of charged proteins on mixed membranes. *Biophys J* **2000**, 79, (4), 1747-1760.
73. Hillebrandt, H.; Tanaka, M., Electrochemical Characterization of Self-Assembled Alkylsiloxane Monolayers on Indium–Tin Oxide (ITO) Semiconductor Electrodes. *The Journal of Physical Chemistry B* **2001**, 105, (19), 4270-4276.
74. Vitkova, V.; Genova, J.; Bivas, I., Permeability and the hidden area of lipid bilayers. *Eur Biophys J* **2004**, 33, (8), 706-714.
75. Mertins, O.; Dimova, R., Insights on the Interactions of Chitosan with Phospholipid Vesicles. Part II: Membrane Stiffening and Pore Formation. *Langmuir* **2013**, 29, (47), 14552-14559.
76. Przybylo, M.; Sýkora, J.; Humpolíčková, J.; Benda, A.; Zan, A.; Hof, M., Lipid Diffusion in Giant Unilamellar Vesicles Is More than 2 Times Faster than in Supported Phospholipid Bilayers under Identical Conditions. *Langmuir* **2006**, 22, (22), 9096-9099.
77. Moreau, R., An evaluation of NBD-phospholipids as substrates for the measurement of phospholipase and lipase activities. *Lipids* **1989**, 24, (8), 691-699.
78. Shreve, A. P.; Howland, M. C.; Sapuri-Butti, A. R.; Allen, T. W.; Parikh, A. N., Evidence for Leaflet-Dependent Redistribution of Charged Molecules in Fluid Supported Phospholipid Bilayers. *Langmuir* **2008**, 24, (23), 13250-13253.
79. Stanglmaier, S.; Hertrich, S.; Fritz, K.; Moulin, J. F.; Haese-Seiller, M.; Rädler, J. O.; Nickel, B., Asymmetric Distribution of Anionic Phospholipids in Supported Lipid Bilayers. *Langmuir* **2012**, 28, (29), 10818-10821.
80. Aranda, S.; Riske, K. A.; Lipowsky, R.; Dimova, R., Morphological transitions of vesicles induced by alternating electric fields. *Biophys J* **2008**, 95, (2), L19-L21.
81. Ben-Yaakov, D.; Andelman, D., Revisiting the Poisson–Boltzmann theory: Charge surfaces, multivalent ions and inter-plate forces. *Physica A: Statistical Mechanics and its Applications* **2010**, 389, (15), 2956-2961.
82. Johnson, S. J.; Bayerl, T. M.; McDermott, D. C.; Adam, G. W.; Rennie, A. R.; Thomas, R. K.; Sackmann, E., Structure of an adsorbed dimyristoylphosphatidylcholine bilayer measured with specular reflection of neutrons. *Biophys J* **1991**, 59, (2), 289-294.
83. Lipowsky, R., Remodeling of membrane compartments: some consequences of membrane fluidity. In *Biological Chemistry*, 2014; Vol. 395, p 253.
84. Baumgart, T.; Das, S.; Webb, W. W.; Jenkins, J. T., Membrane Elasticity in Giant Vesicles with Fluid Phase Coexistence. *Biophys J* **2005**, 89, (2), 1067-1080.
85. Zhao, J.; Wu, J.; Veatch, Sarah L., Adhesion Stabilizes Robust Lipid Heterogeneity in Supercritical Membranes at Physiological Temperature. *Biophys J* **2013**, 104, (4), 825-834.
86. Veatch, S. L.; Keller, S. L., Organization in Lipid Membranes Containing Cholesterol. *Phys Rev Lett* **2002**, 89, (26), 268101.
87. Veatch, S. L.; Keller, S. L., Separation of Liquid Phases in Giant Vesicles of Ternary Mixtures of Phospholipids and Cholesterol. *Biophys J* **2003**, 85, (5), 3074-3083.
88. Semrau, S.; Schmidt, T., Membrane heterogeneity - from lipid domains to curvature effects. *Soft Matter* **2009**, 5, (17), 3174-3186.
89. Lipowsky, R.; Dimova, R., Domains in membranes and vesicles. *Journal of Physics: Condensed Matter* **2003**, 15, (1), S31.

90. Portet, T.; Gordon, S. E.; Keller, S. L., Increasing membrane tension decreases miscibility temperatures; an experimental demonstration via micropipette aspiration. *Biophys J* **2012**, 103, (8), L35-L37.
91. Kahya, N.; Scherfeld, D.; Bacia, K.; Poolman, B.; Schwille, P., Probing lipid mobility of raft-exhibiting model membranes by fluorescence correlation spectroscopy. *J Biol Chem* **2003**, 278, (30), 28109-28115.
92. Yanagisawa, M.; Imai, M.; Masui, T.; Komura, S.; Ohta, T., Growth Dynamics of Domains in Ternary Fluid Vesicles. *Biophys J* **2007**, 92, (1), 115-125.
93. Lipowsky, R., Domain-induced budding of fluid membranes. *Biophys J* **1993**, 64, (4), 1133.
94. Manley, S.; Horton, M. R.; Leczynski, S.; Gast, A. P., Sorting of streptavidin protein coats on phase-separating model membranes. *Biophys J* **2008**, 95, (5), 2301-2307.
95. Blosser, M. C.; Honerkamp-Smith, A. R.; Han, T.; Haataja, M.; Keller, S. L., Measurement of Interleaflet Coupling in Phase Separated Bilayers using High Shear. *Biophys J* **2015**, 108, (2), 240a.
96. Putzel, G. G.; Uline, M. J.; Szleifer, I.; Schick, M., Interleaflet Coupling and Domain Registry in Phase-Separated Lipid Bilayers. *Biophys J* **2011**, 100, (4), 996-1004.
97. Choudhuri, K.; Llodrá, J.; Roth, E. W.; Tsai, J.; Gordo, S.; Wucherpennig, K. W.; Kam, L. C.; Stokes, D. L.; Dustin, M. L., Polarized release of T-cell-receptor-enriched microvesicles at the immunological synapse. *Nature* **2014**, 507, (7490), 118-123.
98. Wu, J.; Fang, Y.; Zarnitsyna, V. I.; Tolentino, T. P.; Dustin, M. L.; Zhu, C., A Coupled Diffusion-Kinetics Model for Analysis of Contact-Area FRAP Experiment. *Biophys J* **2008**, 95, (2), 910-919.
99. Huppa, J. B.; Axmann, M.; Mortelmaier, M. A.; Lillemeier, B. F.; Newell, E. W.; Brameshuber, M.; Klein, L. O.; Schutz, G. J.; Davis, M. M., TCR-peptide-MHC interactions in situ show accelerated kinetics and increased affinity. *Nature* **2010**, 463, (7283), 963-967.
100. Oldenborg, P.-A.; Zheleznyak, A.; Fang, Y.-F.; Lagenaur, C. F.; Gresham, H. D.; Lindberg, F. P., Role of CD47 as a marker of self on red blood cells. *Science* **2000**, 288, (5473), 2051-2054.
101. Willingham, S. B.; Volkmer, J.-P.; Gentles, A. J.; Sahoo, D.; Dalerba, P.; Mitra, S. S.; Wang, J.; Contreras-Trujillo, H.; Martin, R.; Cohen, J. D., The CD47-signal regulatory protein alpha (SIRPα) interaction is a therapeutic target for human solid tumors. *Proceedings of the National Academy of Sciences* **2012**, 109, (17), 6662-6667.
102. Sosale, N. G.; Spinler, K. R.; Alvey, C.; Discher, D. E., Macrophage engulfment of a cell or nanoparticle is regulated by unavoidable opsonization, a species-specific 'Marker of Self' CD47, and target physical properties. *Current Opinion in Immunology* **2015**, 35, 107-112.
103. Seiffert, M.; Cant, C.; Chen, Z.; Rappold, I.; Brugger, W.; Kanz, L.; Brown, E. J.; Ullrich, A.; Bühring, H.-J., Human Signal-Regulatory Protein Is Expressed on Normal, But Not on Subsets of Leukemic Myeloid Cells and Mediates Cellular Adhesion Involving Its Counterreceptor CD47. *Blood* **1999**, 94, (11), 3633-3643.
104. Hollenbeck, K. J., INVLAP.M: A matlab function for numerical inversion of Laplace transforms by the de Hoog algorithm. **1998**.

105. Subramanian, S.; Boder, E. T.; Discher, D. E., Phylogenetic Divergence of CD47 Interactions with Human Signal Regulatory Protein  $\alpha$  Reveals Locus of Species Specificity: Implications for the binding site. *J Biol Chem* **2007**, 282, (3), 1805-1818.
106. Tsai, R. K.; Rodriguez, P. L.; Discher, D. E., Self inhibition of phagocytosis: the affinity of 'Marker of Self' CD47 for SIRP $\alpha$  dictates potency of inhibition but only at low expression levels. *Blood cells, molecules & diseases* **2010**, 45, (1), 67-74.
107. Hatherley, D.; Graham, S. C.; Harlos, K.; Stuart, D. I.; Barclay, A. N., Structure of Signal-regulatory Protein  $\alpha$ : A link to antigen receptor evolution. *The Journal of Biological Chemistry* **2009**, 284, (39), 26613-26619.
108. Vernon-Wilson, E. F.; Kee, W.-J.; Willis, A. C.; Barclay, A. N.; Simmons, D. L.; Brown, M. H., CD47 is a ligand for rat macrophage membrane signal regulatory protein SIRP (OX41) and human SIRP $\alpha$  1. *European Journal of Immunology* **2000**, 30, (8), 2130-2137.
109. Xu, G.-K.; Hu, J.; Lipowsky, R.; Weikl, T. R., Binding constants of membrane-anchored receptors and ligands: A general theory corroborated by Monte Carlo simulations. *The Journal of chemical physics* **2015**, 143, (24), 243136.
110. Charras, G. T.; Coughlin, M.; Mitchison, T. J.; Mahadevan, L., Life and Times of a Cellular Bleb. *Biophys J* **2008**, 94, (5), 1836-1853.

## 8 Appendix

### 8.1 List of figures

FIGURE 1-1 - A) SCHEMATIC DRAWING OF A PHOSPHOLIPID (UPPER) AND CHOLESTEROL (LOWER), SPHERES INDICATE ATOMS B) THREE DIFFERENT LIPID TYPES FOUND IN BIOLOGICAL MEMBRANES C) LIPIDS IN A BILAYER AND CLOSED LIPID BILAYER (VESICLE). NOTE THE SEPARATION OF LENGTH SCALES. FIGURES ADAPTED FROM ALBERTS <sup>1</sup> P. 479,481 .....	10
FIGURE 1-2 – FREE ENERGY OF A HYPOTHETICAL BINARY MIXTURE OF COMPOSITION $x_2$ EXHIBITING LIQUID-LIQUID SEPARATION SHOWN AT THREE DIFFERENT TEMPERATURES. MOST RIGHT: RESULTING ISOBARIC PHASE DIAGRAM. FIGURE ADAPTED WITH MODIFICATIONS FROM KONINGSVELD, ET AL. <sup>2</sup> P. 46 .....	11
FIGURE 1-3 – TWO SUBSTANCES ARE SEPARATED AT $T=0$ (LEFT). EXCHANGE OF TWO MOLECULES AT $T>0$ (RIGHT).....	12
FIGURE 1-4 – TYPICAL PHASE DIAGRAM FOR TERNARY LIPID MIXTURE OF LOW AND HIGH MELTING TEMPERATURE LIPIDS AND A STEROL. THE PHASES ARE LABELLED AS DESCRIBED ABOVE. IN THE SHADED AREA LIPID BILAYERS ARE NOT FORMED. A TIE LINE IS INDICATED. ....	13
FIGURE 1-5 – A) MORPHOLOGY DIAGRAM FOR VESICLES CLOSE TO AN ADHESIVE SURFACE. THE THICK LINE INDICATES A FIRST ORDER TRANSITION FROM FREE TO ADHERED STATE. THE SHADED AREA INDICATES VESICLES USUALLY USED IN OUR EXPERIMENTS, V AND W HAVE THE MEANING AS DESCRIBED IN THE TEXT (FIGURE ADAPTED FROM REF. 14) B) DEFINITION OF THE EFFECTIVE CONTACT ANGLE IN THE CASE OF STRONG ADHESION, THE REAL CONTACT ANGLE IS ALWAYS $180^\circ$ AS THE MEMBRANE EXHIBITS NO KINKS C) ARTISTIC RENDERING OF THREE VESICLES ADHERING TO A POLYLYSINE COATED SURFACE AS OBTAINED BY CONFOCAL MICROSCOPY, SCALE BAR $5\mu\text{M}$ .....	15
FIGURE 1-6 – SCHEMATIC DRAWING OF THE PLASMA MEMBRANE, THE DENSITY OF COMPONENTS IS REDUCED FOR VISIBILITY. IMAGE BY MARIANA RUIZ. ....	16
FIGURE 1-7 – TEM IMAGE OF A CELL. THE GLYCOLYX CAN BE CLEARLY SEEN AS THE THICK FUZZY DARK LINE, FROM ALBERTS <sup>1</sup> P. 502 .....	18
FIGURE 1-8 – LEFT: DIFFERENT CLASSES OF CAMs, ADAPTED FROM SACKMANN AND SMITH <sup>22</sup> . RIGHT: SCHEMATIC OF TWO MEMBRANE SEGMENTS EXHIBITING DIFFERENT MEMBRANE-MEMBRANE SEPARATION DUE TO NON-SPECIFIC INTERACTIONS (GREY), MODULATING SPECIFIC BINDING (GREEN RODS) .....	19
FIGURE 2-1 – OPTICAL PATH OF A CONFOCAL MICROSCOPE. A-ILLUMINATION PINHOLE, C-CONDENSER LENS, D-IMAGE PLANE. LIGHT FROM THE CONE E CANNOT PASS THE PINHOLE B IN FRONT OF THE DETECTOR P. O OBJECTIVE LENS. ARROWS INDICATE THE SCANNING OPERATION. FIGURE ADAPTED FROM PAWLEY AND MASTERS <sup>39</sup> .....	21
FIGURE 2-2 – LEFT: SOME LIPIDS USED IN MODEL MEMBRANES AND TWO DYES (NBD-PG AND DiIc18). NBD-PG IS LABELLED IN THE FATTY ACID CHAIN AND DiI IS CONJUGATED WITH TWO CARBOHYDRATE CHAINS. RIGHT: SNAPSHOT OF A MD SIMULATION, DPPC MEMBRANE WITH THE DYE DiIc18, ADAPTED FROM GULLAPALLI, ET AL. <sup>40</sup> .....	22
FIGURE 2-3 THE SAME VESICLE OBSERVED BY EPIFLUORESCENCE MICROSCOPY AT DIFFERENT TEMPERATURES. UPPER ROW: AT $T_2$ THE VESICLE EXHIBITS OPTICALLY RESOLVABLE DOMAINS. THE TEMPERATURE IS RAMPED UP FAST ( $1^\circ\text{C}/\text{min}$ ) TO A TEMPERATURE $T_1$ WHERE THE VESICLE APPEARS HOMOGENOUS. RAPID COOLING LEADS TO SPINODAL DECOMPOSITION (LOWER ROW). THE SHOWN VESICLE IS NOT LET TO EQUILIBRATE DURING THE COOLING PROCESS. SCALE BAR $10\mu\text{M}$ .....	23
FIGURE 2-4 A) SCHEMATIC OF A LIPID BILAYER STAINED WITH A GREEN DYE. THE CIRCULAR REGION OF INTEREST (ROI) IS BLEACHED BY A STRONG LASER PULSE AT *. RECOVERY CAN BE FOLLOWED BY THE AVERAGE INTENSITY IN THE ROI. B) TWO DIFFERENT MECHANISMS FOR RECOVERY. LEFT: FREE DIFFUSION, RIGHT: DIFFUSION AND BINDING AND UNBINDING AT IMMOBILE LOCATIONS INDICATED BY AN ORANGE CIRCLE. ....	24
FIGURE 2-5 – LEFT: DIFFERENT STAGES (A-E) OF GUV ELECTROFORMATION, ADAPTED FROM LUISI AND WALDE <sup>44</sup> . RIGHT: EPIFLUORESCENT MICROGRAPH OF A HEK CELL BUDDING A GPMV (INVERTED CONTRAST). SCALE BAR $10\mu\text{M}$ .....	26
FIGURE 3-1 - PICTURE OF THE EXPERIMENTAL CHAMBER FIXED ON AN INVERTED CONFOCAL MICROSCOPE. CONNECTORS TO LEFT AND RIGHT LEAD TO THE DC-VOLTAGE SOURCE. THE TRANSPARENT ITO GLASSES CAN BE SEEN IN THE MIDDLE OF THE PICTURE. THE RED SPACER IS NOT IN CONTACT WITH THE VESICLE SUSPENSION. ....	30



FIGURE 3-2 - EXAMPLES FOR THE INTENSITY PROFILES ACROSS THE MEMBRANES OF AN UNQUENCHED VESICLE (RED DIAMONDS) AND A QUENCHED VESICLE (BLACK SQUARES) ADHERING TO THE ITO GLASS. THE PROFILES WERE FITTED WITH A GAUSSIAN (ORIGINPRO 8.6) AND THE PEAK VALUE TAKEN AS AN INDICATOR OF DYE CONCENTRATION. ....	31
FIGURE 3-3 - SKETCHES OF THE SAME VESICLE WITH TOTAL AREA $A$ AND ENCLOSED VOLUME $V$ (A) IN THE LIMIT OF VERY LARGE ADHESION ENERGY AND (B) WHEN SUBJECT TO A FINITE ADHESION ENERGY. IN (A), THE SHAPE IS THAT OF A SPHERICAL CAP AND THE VALUES OF THE EFFECTIVE CONTACT ANGLE $\theta_0$ AND THE RADIUS OF THE ADHERING MEMBRANE SEGMENT $R_0$ ARE FIXED BY $A$ AND $V$ THROUGH EQ. (1). IN (B), THE SHAPE DEVIATES FROM A SPHERICAL CAP AND THE RADIUS OF THE ADHERING MEMBRANE SEGMENT $R < R_0$ IS GIVEN BY EQ. (2). ....	32
FIGURE 3-4 - VERTICAL CROSS SECTION VIEW OF AN ADHERING VESICLE (AT 1V) AS OBTAINED BY CONFOCAL MICROSCOPY. THE MANUALLY EXTRACTED CONTOUR WHICH IS USED IN THE FURTHER ANALYSIS OF THE VESICLE AREA AND VOLUME IS SHOWN IN YELLOW. ....	33
FIGURE 3-5 - CIRCLE OF BEST FIT (YELLOW) IN THE CONTACT ZONE OF AN ADHERING VESICLE (CONFOCAL SIDE VIEW). THE SCALE BAR IS $25\mu\text{m}$ . ....	35
FIGURE 3-6 - PHASE CONTRAST IMAGES OF A VERY DEFLATED VESICLE CONSECUTIVELY EXPOSED (FROM LEFT TO RIGHT) TO 0V, 1.2V AND 0V EXTERNAL VOLTAGE UNDERGOING NEARLY COMPLETE REVERSIBLE SHAPE CHANGE FROM PROLATE TO ADHERED BACK TO PROLATE SHAPE. SCALE BAR CORRESPONDS TO $20\mu\text{m}$ . ....	36
FIGURE 3-7 - CONFOCAL IMAGES OF THE VERTICAL CROSS SECTIONS OF A GUV MADE OF DOPC/DOPG 80/20. THE SCALE BAR REPRESENTS $20\mu\text{m}$ . THE MEMBRANE FLUORESCENCE IS SHOWN IN GREEN AND THE REFLECTION FROM THE ITO SURFACE IS SHOWN IN RED. (A) NON-ADHERING VESICLE IN THE ABSENCE OF APPLIED VOLTAGE. (B) SAME VESICLE ADHERING TO THE SUBSTRATE UPON APPLICATION OF 1 V DC FIELD. ARROWS INDICATE THE SUPPRESSION OF MEMBRANE FLUCTUATIONS IN THE VICINITY OF THE SURFACE DUE TO ADHESION AND THE APPEARANCE OF A SHARP CONTACT ANGLE. ....	37
FIGURE 3-8 - ADHESION ENERGY AND MEMBRANE TENSION IN DOPC/DOPG 80/20 VESICLES ADHERING TO AN ITO SUBSTRATE AT VARIED APPLIED EXTERNAL POTENTIAL. (A) ADHESION ENERGIES OF OVERALL 24 VESICLES AT DIFFERENT EXTERNAL POTENTIALS. THE DATA IS OBTAINED FROM ANALYSIS BASED. ....	38
FIGURE 3-9 - COMPARISON OF DATA FOR THE ADHESION ENERGY ASSESSED VIA THE WHOLE-CONTOUR METHOD (X AXIS) AND FROM THE CONTACT-CURVATURE METHOD (LEFT Y AXIS; THE RIGHT Y AXIS SHOWS THE MEMBRANE CURVATURE IN THE CONTACT ZONE, $R_c$ ). THE DASHED LINE HAS SLOPE ONE AND REPRESENTS IDEAL AGREEMENT BETWEEN THE TWO METHODS. ....	39
FIGURE 3-10 - NORMALIZED FLUORESCENCE INTENSITY FROM NBD-PG IN THE ADHERING MEMBRANE SEGMENT OF A (UNQUENCHED) VESICLE EXPOSED TO DIFFERENT EXTERNAL POTENTIALS CORRESPONDING TO DIFFERENT ADHESION STRENGTHS. THE SKETCHES ABOVE ILLUSTRATE THE DEPLETION IN THE ADHERING MEMBRANE SEGMENT OF NBD-PG (RED ASTERISKS) FROM THE OUTER LEAFLET OF THE VESICLE UPON ADHESION TO THE SUBSTRATE, SEE TEXT FOR DETAILS. ....	41
FIGURE 3-11 - RATIO OF FLUORESCENT INTENSITY MEASURED IN THE ADHERING AND FREE MEMBRANE SEGMENT FOR TWO DIFFERENT ENSEMBLES OF VESICLES: UNQUENCHED (A) AND WITH QUENCHED EXTERNAL LEAFLET (B). THE VESICLES WERE IMAGED AT DIFFERENT EXTERNAL POTENTIALS AND THEN THE CORRESPONDING ADHESION ENERGIES WERE CALCULATED BY THE WHOLE-CONTOUR METHOD. IN THE UNQUENCHED VESICLES, THE DYE IS DEPLETED FROM THE ADHERING MEMBRANE SEGMENT WITH INCREASING ADHESION. FOR THE VESICLES WITH QUENCHED EXTERNAL LEAFLET (B), NO SUCH TREND IS OBSERVED SUGGESTING THAT THE APPLIED EXTERNAL POTENTIAL AND THE ADHESION PROCESS INDUCE DYE REDISTRIBUTION ONLY IN THE EXTERNAL LEAFLET OF THE VESICLES. ....	42
FIGURE 3-12 - THE PH CHANGE IN THE BUFFER IN THE VICINITY OF THE BOTTOM ITO GLASS AS A FUNCTION OF THE EXTERNAL POTENTIAL WAS MEASURED USING THE PH-SENSITIVE DYE SNARF (SEMINAPHTHORHODAFUOR, LIFE TECHNOLOGIES) WHICH WAS ADDED AT CONCENTRATION OF 10 mM TO THE BUFFER. THE INTENSITY RATIO BETWEEN THE GREEN AND RED PEAK SIGNAL OF THE DYE WAS CONVERTED TO PH BASED ON CALIBRATION MEASUREMENTS IN SOLUTIONS OF KNOWN PH. THE MAXIMAL DECREASE IN PH WAS MEASURED DIRECTLY (SUB $\mu\text{m}$ DISTANCE) AT THE ITO GLASS SURFACE BUT IS STILL ABOVE PH 6. ....	43

FIGURE 3-13 - (A) COLOR CODE AND CONTOUR LINES SHOW THE SIMULATED NORMALIZED COMPOSITION OF THE ADHERING MEMBRANE SEGMENT AT DIFFERENT BILAYER-SURFACE DISTANCES AND EXTERNAL VOLTAGES. THE BROKEN LINE INDICATES THE ONSET OF ADHESION AS EXPERIMENTALLY MEASURED (B) INSERT SHOWS THE OBSERVED EXPERIMENTAL FLUORESCENT INTENSITIES (BLACK DOTS) .....	45
FIGURE 4-1 – EXPERIMENTAL CHAMBER. IN THE CENTER, THE TWO ITO GLASSES CAN BE SEEN. THE TEMPERATURE BATH IS CONNECTED ON THE TOP. THE TEMPERATURE PROBE ON THE RIGHT IS PLACED IN THE CHAMBER ONLY WHEN PERFORMING TEMPERATURE CALIBRATION. ....	49
FIGURE 4-2- LEFT: MEASURED MISCIBILITY TEMPERATURES FOR DIFFERENT MEMBRANE COMPOSITIONS IN FREE (NONADHERING) GUVs. FILLED POINTS INDICATE NO OBSERVED MACROSCOPIC PHASE SEPARATION DOWN TO 10°C. RIGHT: INTERPOLATION BETWEEN DATA POINTS, COLOURS INDICATE TEMPERATURE IN °C .....	50
FIGURE 4-3- DIFFERENT MORPHOLOGIES (VERTICAL CONFOCAL CROSS SECTIONS) OF ADHERING VESICLES OBTAINED DURING EXPERIMENTS. ARROWS INDICATE LIQUID ORDERED DOMAINS. IN THE GIBBS DIAGRAM, BLUE POINTS INDICATE COMPOSITIONS WHERE NO CHANGE IN DiIC18 PARTITIONING BETWEEN THE BOUND AND UNBOUND SEGMENTS WAS FOUND, AND RED WHERE PARTITIONING BETWEEN THE SEGMENTS WAS MEASURED. GREEN CIRCLES INDICATE COMPOSITIONS WHERE NO SIGNIFICANT CHANGE IN THE MISCIBILITY TEMPERATURE BETWEEN FREE AND ADHERED VESICLES WAS FOUND. THE DOTTED LINE IS THE COEXISTENCE BOUNDARY AS FOUND FROM FIGURE 4-2. SCALE BARS 5µm, ALL VOLTAGES BETWEEN 1.1 AND 1.3VDC .....	51
FIGURE 4-4 - LEFT: THE ADHERING MEMBRANE SEGMENT OF A DEFLATED GUVs (3/5/2). THE VESICLE UNDERGOES DOMAIN COARSENING AND SUBSEQUENT DISAPPEARANCE OF DOMAINS UPON ADHESION. THE VOLTAGE WAS RAMPED UP FAST (<5MINUTES). DOMAINS IN THE FREE SEGMENT ALSO DISAPPEAR (NOT SHOWN). SCALE BAR 5µm. RIGHT: ADHERING VESICLE (AT 1.5VDC) AFTER A TEMPERATURE CYCLE JUST ABOVE THE MISCIBILITY TEMPERATURE OF THE FREE VESICLE. UPPER: (x,y) VIEW OF THE ADHERING MEMBRANE SEGMENT. LOWER: MAXIMAL PROJECTION OF THE FREE SEGMENT. UPON COOLING DOMAINS NUCLEATE IN BOTH SEGMENTS. SCALE BAR 10µm. ....	52
FIGURE 4-5 - LEFT: DIFFUSION COEFFICIENT OF DiIC18 AS MEASURED BY FRAP IN eSM:CHOL 8:2 MEMBRANES AT RT, DATA IS SHOWN FROM A SINGLE REPRESENTATIVE VESICLE. RIGHT: PARTITIONING OF THE MEMBRANE FLUIDITY MARKER DiC18 IN DOPC:DOPC (SQUARES) AND eSM:CHOL (LINE) MEMBRANES AT RT. GREY INDICATES INSIGNIFICANT CHANGES. ....	53
FIGURE 4-6 – A) NO SIGNIFICANT CHANGES OF DiIC18 PARTITIONING BETWEEN THE TWO SEGMENTS, ADHERED AND UNBOUND, IN TWO COMPOSITIONS THAT APPEAR HOMOGENOUS AT RT B) ONLY VESICLES CLOSE TO THE CRITICAL COMPOSITION SHOW PARTITION OF THE MEMBRANE MARKER DiIC18. EACH DATA POINT IS AN INDIVIDUAL VESICLE. C) DiIC18 IS ENRICHED IN THE ADHERING MEMBRANE SEGMENT WITH INCREASING ADHESION ENERGY. DATA OBTAINED FROM AN INDIVIDUAL VESICLE AT DIFFERENT VOLTAGES.....	54
FIGURE 4-7 – CONFOCAL IMAGES(x,y) OF THE ADHERING SEGMENT OF A VESICLE EXHIBITING SMALL DOMAINS. THE VOLTAGE IS RAMPED UP FROM 0V TO 1.2VDC AT 0s. THE WHITE CIRCLE INDICATES REGIONS WITH EQUAL DiIC18 INTENSITY. SCALE BARS 5µm. THE LAST TWO IMAGES SHOW THE ADHERING SEGMENT AND THE MAXIMAL PROJECTION OF THE FREE SEGMENT.....	55
FIGURE 4-8 – LEFT, MIDDLE: 5.5/2.5/2 @ 1.3Vdc, RT, ADHERING MEMBRANE SEGMENT. ADHESION INDUCES THE FORMATION OF BUDS WITH HETEROGENEOUS DiIC18 DENSITIES. BUDS ARE TYPICALLY BETWEEN 1µm AND 3µm RIGHT: 2/6/2 18 °C EPI FLUORESCENT MICROGRAPH INDICATES DOMAINS IN MOTHER VESICLE BUT HOMOGENOUS APPEARANCE OF THE BUD AS THE TEMPERATURE IS LOWERED, INSERT SHOWS THE FOCAL PLANE OF THE UPPER POLE OF THE MOTHER VESICLE, DOMAINS ARE INDICATED BY AN ARROW. SCALE BARS 10µm .....	56
FIGURE 4-9 – ADHERING MEMBRANE SEGMENT OF A VESICLE OF COMPOSITION 5/3/2 @ 1.3VDC BEFORE (LEFT) AND AFTER (RIGHT) THE TEMPERATURE IS CYCLED ABOVE THE MAIN MELTING TEMPERATURE AND BACK TO RT. SCALE BAR 10µm. ....	57
FIGURE 4-10 – (LEFT, MIDDLE): CONFOCAL SIDE VIEW (x,z), ADHERING MEMBRANE SEGMENT (x,y) OF A VESICLE (4/2/2), ARROWS INDICATE LIQUID ORDERED DOMAINS. RIGHT: ADHERING MEMBRANE SEGMENT (5/3/2) WITH A DOMAIN OF ABOUT HALF THE DiIC18 FLUORESCENCE INTENSITY OF THE LIQUID DISORDERED PHASE. SCALE BAR 10µm.....	57

FIGURE 4-11 - SKETCH OF THE OBSERVED COMPOSITIONAL AND BUDDING TRANSITION. STARS INDICATE TWO DIFFERENT LIPID SPECIES. LEFT: ARROWS INDICATE LIPID FLOWS. THE LOWER RIGHT IMAGE INDICATES THE OBSERVED LIQUID ORDERED DOMAIN IN THE CONTACT LINE. THE MISMATCH ENERGY DUE TO SORTING LIPID IN ONLY THE OUTER LEAFLET IS SKETCHED IN THE LOWER LEFT. ....	58
FIGURE 4-12 – LEFT: FIGURES ADAPTED FROM CHOUDHURI, ET AL. <sup>97</sup> . TEM MICROGRAPH OF THE IMMUNOLOGICAL SYNAPSE MODEL. RED ARROWS INDICATE EXTRACELLULAR BUDS, WHITE ARROW THE PLASMA MEMBRANE. SCALE BAR 500NM. LOWER IMAGE: BUDS ARE CONNECTED BY A NECK IN THE CONTACT LINE WHEN THE ESCRT-III MACHINERY IS KNOCKED OUT. RIGHT: MEMBRANE MORPHOLOGY EXTRACTED FROM THE TEM (UPPER) AND VESICLE MORPHOLOGY IN THIS WORK (LOWER). NOT TO SCALE. ....	60
FIGURE 5-1 - ENHANCED UPTAKE OF OPSONIZED A549 CELLS UNDER ACIDIC CONDITIONS. CONFOCAL IMAGES OF THE DIFFERENT EXPERIMENTAL OUTCOMES AFTER IMAGE PROCESSING (GAUSSIAN IMAGE FILTER AND THRESHOLDING) GREEN: MACROPHAGE, RED: A539 CELL. LEFT: NO EATING, MIDDLE: PARTIAL ENGULFMENT RIGHT: COMPLETE ENGULFMENT. TOP: HISTOGRAM OF THE DIFFERENT EXPERIMENTAL OUTCOMES IN TWO CONDITIONS (PH6, PH7.4). FOR EACH MACROPHAGE THE RELATIVE OVERLAP BETWEEN THE GREEN CHANNEL AND THE RED CHANNEL WAS COMPUTED AND NORMALIZED TO THE AREA OF THE MACROPHAGE. ....	63
FIGURE 5-2 - CONFOCAL IMAGE OF ISOLATED GPMVs. LEFT: GFP LABELLED CD47 RIGHT: MEMBRANE MARKER DiIc18. THE ARROW INDICATES A TYPICAL VESICLE SELECTED FOR EXPERIMENTS (NO INTERNAL FLUORESCENCE). SCALE BAR 10μM	66
FIGURE 5-3 - UPPER LEFT: ANTI-CD47 IMMUNOSTAINING. LOWER LEFT: GFP-CD47 CHANNEL. MIDDLE: CORRELATION BETWEEN ANTI-C47 AND GFP SIGNAL INDICATE FUNCTIONAL RECONSTITUTION OF CD47. EACH DATA POINT IS AN INDIVIDUAL VESICLE. UPPER RIGHT: INCUBATION OF RED BLOOD CELLS TOGETHER WITH A GPMV TO ESTIMATE THE CD47 CONCENTRATION IN REAL UNITS. ARROW INDICATES A RBC. SCALE BAR 10μM.....	67
FIGURE 5-4 - LEFT: ANTI-GST STAINING OF SIRPA ABSORBED ON A GLASS SLIDE. THE BLACK REGION IS A SCRATCH WITH A PIPETTE TIP TO ESTIMATE THE BACKGROUND LEVEL. SCALE BAR 60μM RIGHT: CONFOCAL VERTICAL CROSS SECTION (x,z) OF AN ADHERING VESICLE ON A SIRPA COATED SLIDE (LEFT) AND A NONADHERING VESICLE SITTING ON A BSA COATED GLASS SLIDE (RIGHT). SCALE BARS 5μM .....	68
FIGURE 5-5 - TYPICAL EQUILIBRATION OF THE ADHERING MEMBRANE SEGMENT OBSERVED BY EPIFLUORESCENCE (TIME INCREASES FROM LEFT TO RIGHT). IN THE FIRST MINUTES A BRIGHT RING APPEARS IN THE RIM OF THE ADHERING SEGMENT (MIDDLE). OVER THE TIME COURSE OF AN HOUR THE DISTRIBUTION BECOMES HOMOGENOUS (RIGHT). DIFFERENT VESICLES ARE SHOWN AT EACH TIME POINT, THE ADHERING SEGMENT IS ABOUT 15μM IN DIAMETER.....	68
FIGURE 5-6 - QUANTIFICATION OF BOUND AND UNBOUND CD47 BY FLUORESCENCE INTENSITY. LEFT: INDIVIDUAL DATA POINT FROM DIFFERENT VESICLES UNDER THE SAME CONDITIONS. THE LINE INDICATES A LINE PROFILE WHICH IS USED TO EXTRACT THE FLUORESCENCE INTENSITY. SCALE BAR 5μM .....	69
FIGURE 5-7 – FRAP RECOVERY INTENSITY TIME COURSE AND CONFOCAL IMAGES OF A TYPICAL RECOVERY. LEFT: FREE MEMBRANE SEGMENT WITH CROSS SECTION IMAGES ABOVE, THE THREE CURVES REPRESENT DIFFERENT VESICLES. RIGHT: BOUND MEMBRANE SEGMENT WITH TOP VIEW IMAGES ABOVE. FIT FOR $[R]_{K_{ON}} \approx 4.32 \cdot 10^4 \text{ s}^{-1}$ , $K_{OFF} \approx 4.9 \text{ s}^{-1}$ . BLEACHED SPOT IS 1μM IN DIAMETER .....	70
FIGURE 5-8 - LEFT: $[R] K_{2D,FRAP}$ OBTAINED BY FRAP, EACH DATAPOINT REPRESENTS A SINGLE VESICLE $[RL]$ IS OBTAINED BY SUBTRACTING THE FLUORESCENT INTENSITY IN THE FREE SEGMENT FROM THE INTENSITY IN THE ADHERED SEGMENT. RIGHT: RATIO OF $K_{2D}$ AND $K_{3D}$ MEASURED AT PH 7.4 TO THE RESPECTIVE VALUES MEASURED AT PH 6. $K_{2D}$ VALUES WERE OBTAINED EITHER BY INTENSITY MEASUREMENTS OR FRAP. $K_{3D}$ IS OBTAINED BY BINDING SOLUBLE SIRPA TO RBCs. ....	71